Istituto Universitario
di Studi Superiori di Pavia

Università degli
Studi di Pavia

EUROPEAN SCHOOL FOR ADVANCED STUDIES IN
REDUCTION OF SEISMIC RISK

ROSE SCHOOL

CYCLIC SOIL PLASTICITY

A Dissertation Submitted in Partial
Fulfilment of the Requirements for the Master Degree in

EARTHQUAKE ENGINEERING

By

DAMIAN GRANT

Supervisors: Prof. FERDINANDO AURICCHIO
Dr. JOHN BERRILL

November, 2002

The dissertation entitled “Cyclic Soil Plasticity”, by Damian Grant, has been approved in partial fulfilment of the requirements for the Master Degree in Earthquake Engineering.

Ferdinando Auricchio _____

John Berrill _____

ABSTRACT

Accurate constitutive models for cyclic soil plasticity are an important requirement in many engineering applications. Models based on the Modified Cam-Clay yield criterion, an associative flow rule, a nonlinear hyperelastic stress–strain law and an appropriate hardening equation, are effective for cases of monotonic loading, but inaccurate for cyclic loading conditions.

In this dissertation, a Modified Cam-Clay model is presented, followed by two separate approaches extending the model's effectiveness to cyclic loading histories. In the first approach, an anisotropic Bounding Surface model with a vanishing elastic region and a discrete relocation of the back stress tensor is implemented. Secondly, the Modified Cam-Clay model is reformulated in a Generalised Plasticity framework, in which a yield function defines the boundary between elastic and inelastic states, and a limit function defines admissible and inadmissible states.

For each approach, a time discrete version of the model is presented, and a solution algorithm based on a return mapping algorithm is derived. The models are tested in a finite element setting, and behaviour under different loading histories is compared. It is found that both the Bounding Surface and Generalised Plasticity models provide some advantages over the original model, but suffer from several flaws which need to be addressed in future formulations.

ACKNOWLEDGEMENTS

I would particularly like to thank Ferdinando Auricchio and John Berrill who have been excellent mentors in my graduate studies to date.

I would also like to acknowledge Guy Houlsby and Carlo Callari, who gave me valuable advice at various stages of this work.

Finally, thanks to Mum and Dad who have mentored and advised me for my whole life — a rewarding experience overall, of which this dissertation is only a small part.

CYCLIC SOIL PLASTICITY

TABLE OF CONTENTS

1. SOIL PLASTICITY

1.1 INTRODUCTION

As computational modelling techniques are being increasingly used in the solution of engineering problems, the need for accurate and efficient constitutive models is becoming greater. Material models which accurately describe the cyclic behaviour of soil are essential in many applications, and of particular importance in the field of Earthquake Engineering.

A large number of models for the plasticity of soils have been proposed in the literature. In this chapter, some of the developments in soil plasticity relevant to this work are presented. Several different historical yield criteria are summarised, with particular focus on the commonly used Cam-Clay [Roscoe and Schofield, 1963] and Modified Cam-Clay [Roscoe and Burland, 1968] yield functions. Elastic stress–strain relations and hardening equations are also presented, for use within the Modified Cam-Clay framework. Finally, some aspects of the cyclic response of soils are addressed, and the Bounding Surface Plasticity [Dafalias and Herrmann, 1982] and Generalised Plasticity [Lubliner *et al.*, 1993] frameworks are introduced.

In subsequent chapters, these concepts are developed further, and converted to a discrete time regime. Return map algorithms are presented for each model, and tangent moduli consistent with the algorithms are obtained. Finally, a series of numerical simulations is carried out, and a comparison of the models made, allowing some conclusions to be drawn about their applicability to cyclic soil plasticity.

Notation

In the following, $\mathbf{1}$ and $\mathbb{I}$ represent the second and fourth order identity tensors, respectively, and a boldface notation is used for all other second and fourth order tensors. Moreover, $\mathbb{I}$ may be decomposed

into volumetric, $\mathbb{I}_{\text{vol}}$, and deviatoric, $\mathbb{I}_{\text{dev}}$, parts, defined as:

$$\mathbb{I}_{\text{vol}} = \frac{1}{3}\mathbf{1} \otimes \mathbf{1} \qquad \mathbb{I}_{\text{dev}} = \mathbb{I} - \frac{1}{3}\mathbf{1} \otimes \mathbf{1} \tag{1.1}$$

such that $\mathbb{I} = \mathbb{I}_{\text{vol}} + \mathbb{I}_{\text{dev}}$.

The Euclidean norm of a second order tensor, $\mathbf{a}$, is indicated by $\|\mathbf{a}\|$ (i.e. $\|\mathbf{a}\|^2 = a_{ij}a_{ij}$, where summation is implied over repeated indices), while the trace is denoted by $\text{tr}(\mathbf{a})$. The symbol ':' is used for the double contraction of tensor adjacent indices (e.g. $\mathbf{a} : \mathbf{b} = a_{ij}b_{ij}$ and $\mathbf{C} : \mathbf{d} = C_{ijkl}d_{kl}$).

It is assumed that the strain tensor, $\boldsymbol{\varepsilon}$, can be additively decomposed into elastic and plastic parts, denoted by e and p superscripts, respectively:

$$\boldsymbol{\varepsilon} = \boldsymbol{\varepsilon}^e + \boldsymbol{\varepsilon}^p \tag{1.2}$$

It will also be useful to decompose the strain and stress ($\boldsymbol{\sigma}$) tensors into volumetric and deviatoric parts:

$$\begin{aligned} \boldsymbol{\varepsilon} &= \mathbf{e} + \frac{\theta}{3}\mathbf{1} \\ \boldsymbol{\sigma} &= \mathbf{s} + p\mathbf{1} \end{aligned} \tag{1.3}$$

where:

$$\begin{aligned} \theta &= \text{tr}(\boldsymbol{\varepsilon}) & \mathbf{e} &= \boldsymbol{\varepsilon} - \frac{1}{3}\text{tr}(\boldsymbol{\varepsilon}) \\ p &= \frac{1}{3}\text{tr}(\boldsymbol{\sigma}) & \mathbf{s} &= \boldsymbol{\sigma} - \frac{1}{3}\text{tr}(\boldsymbol{\sigma}) \end{aligned} \tag{1.4}$$

The geotechnical sign convention will be used in this work, in which compressive stresses and strains are considered positive. Furthermore, the stress tensor, $\boldsymbol{\sigma}$, will actually represent the effective stress of the soil, subtracting the effects of pore water pressure.

All other notations will be explained in the text.

1.2 YIELD CRITERIA

Several different yield criteria have been proposed for geomaterials in the past. The main feature of soil behaviour that must be captured by a yield criterion is the dependence of the yield strength on the mean pressure. In 'drained' loading conditions, in which water pressure is allowed to dissipate, and at low levels of confining stress, increasing the compressive pressure will generally increase the shear strength of a soil.

The first attempt to describe such a behaviour can be found in Coulomb's early work on the strength of soil and other engineering materials [Coulomb, 1776], where the strength of geomaterials is attributed to a combination of cohesion (c) and friction (ϕ):

$$\tau = c + \sigma \tan\phi \tag{1.5}$$

where τ and σ are the shear and effective normal stress on the failure (yield) surface, respectively.

The implication of (1.5) is that increasing the mean pressure on the soil will increase the yield strength. This was made more explicit by the work of Drucker and Prager [1952], who added mean stress-dependence to von Mises' yield criterion [von Mises, 1913]:

$$q - \beta p = k \tag{1.6}$$

in which q is the deviatoric stress, with $q = \sqrt{3/2}\,\|\mathbf{s}\|$, p is the volumetric stress, with $p = \mathrm{tr}(\boldsymbol{\sigma})$, and β and k are material constants of the soil. Plotting volumetric vs. deviatoric stress ('the p–q plane'), (1.6) describes a straight line of slope β, crossing the p–axis at $-k/\beta$. This implies that if the mean stress is increased, keeping the deviatoric stress constant, yielding cannot occur — an unrealistic description of soil response .

Due to the fact that (1.6) does not give a very accurate representation of soil behaviour, several modifications have been proposed to the Drucker-Prager criterion since its formulation. Many of these lead to a more accurate yield surface for low levels of mean pressure, but still suffer from the limitation of an infinite pressure capacity, under constant deviatoric stress. Although yield criteria based on the Drucker-Prager criterion are still used in some applications, they have largely been superseded by the Cam-Clay and Modified Cam-Clay models introduced in the next section.

1.3 CAM-CLAY PLASTICITY

The Cam-Clay model (CC) of Roscoe and Schofield [1963] was an early attempt to make use of a 'capped' yield surface, in which a limit is placed on the yield strength of the soil under increasing pressure. The CC yield criterion takes the following form:

$$f(\boldsymbol{\sigma}, p_c) = q + Mp \ln \frac{p}{p_c} = 0 \tag{1.7}$$

where p_c is a stress-like hardening parameter, and M is a material constant. In the p–q plane, p_c gives the intercept of the yield surface with the p–axis, while M defines the aspect ratio.

In the context of geomechanics, p_c represents the preconsolidation pressure of the soil. Indicating with p_0 the initial value of p, we may distinguish between normally consolidated soils ($p_0 = p_c$), and overconsolidated soils ($p_0 < p_c$). The parameter, M, gives the slope of the Critical State Line (CSL) in the p–q plane, which defines a locus of stress states for which the soil will continue to yield at constant volume under constant effective stress [Roscoe *et al.*, 1958].

To improve the model effectiveness, Roscoe and Burland [1968] modified the original yield criterion to an ellipse in the p–q plane:

$$f(\boldsymbol{\sigma}, p_c) = \frac{q^2}{M^2} + p(p - p_c) = 0 \tag{1.8}$$

The CC and MCC yield surfaces, Equations (1.7) and (1.8) respectively, are compared in Fig. 1.1.

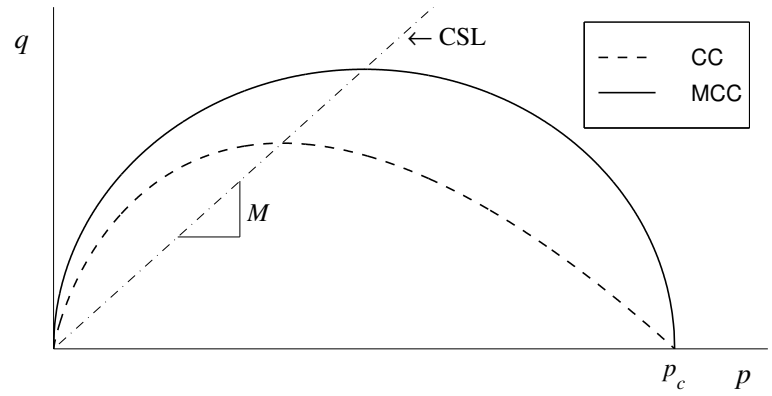

Figure 1.1: Cam-Clay (CC) and Modified Cam-Clay (MCC) yield surfaces in p–q plane.

A major strength of both Cam-Clay yield surfaces is in the modelling of plastic strain. Making use of an associative flow rule, the plastic strain rate vector is normal to the yield surface at the current stress point. From Fig. 1.1, if $p < p_c/2$, the volumetric plastic strain rate is negative, and the soil volume increases ('dilation'), while if $p > p_c/2$, the soil decreases in volume ('compaction'). Finally, if $p = p_c/2$, the volumetric plastic strain rate is zero, a condition described as 'critical state'. Conceptually, this provides an accurate model of soil behaviour at the onset of yielding.

As evident from Fig. 1.1, associative flow at high pressure will result in a higher deviatoric strain rate for the original CC surface compared with the MCC surface, as the slope of the normal to the curve has a larger component in the q–direction. The latter has been shown to give a more accurate model of soil behaviour [Roscoe and Burland, 1968]. Furthermore, the CC surface may present computational difficulties, as the derivative of (1.7) is not defined for $q = 0$. For these reasons, the MCC surface of (1.8) is used in the remainder of this work.

In addition to a yield criterion, a complete MCC model will require an elastic stress–strain law, and an evolutionary equation for the preconsolidation pressure, p_c. These components of the model are introduced in the next three sections, starting from considerations based on the isotropic compression response of soil.

1.4 ISOTROPIC COMPRESSION RESPONSE

Insight into both the elastic and inelastic components of an appropriate plasticity model for soils can be obtained from the response to isotropic compression loading. In the original Cam-Clay formulations, a bilinear relation between the specific volume, v and the natural logarithm of the pressure, p was consid-

ered. Specific volume is defined as:

$$v = \frac{V}{V_s} \tag{1.9}$$

where V is the total soil volume, and V_s is the volume of solid particles. In geotechnical engineering, v is commonly related to θ through the following expression:

$$\theta = \ln \frac{v}{v_0} \tag{1.10}$$

where v_0 is a reference value of v, for $\theta = 0$.

The bilinear relation between v and $\ln p$ is shown in Fig 1.2(a). The slopes of the two linear portions of the graph are indicated as λ' and k'.

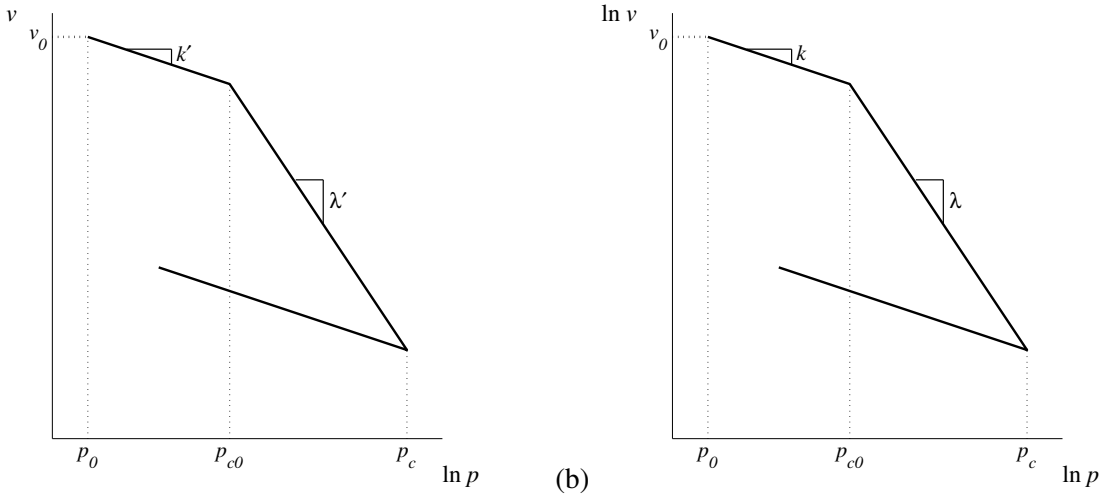

Figure 1.2: (a) Bilinear relation between v and $\ln p$, and (b) bilinear relation between $\ln v$ and $\ln p$.

Fig. 1.2(a) is consistent with common geotechnical engineering practice, and it gives a good fit of laboratory data. However, it can also be shown to lead to unrealistic behaviour [Hashiguchi, 1995], particularly at high pressure levels for which negative v is predicted.

Because of these limitations, it has become common practice in Cam-Clay plasticity to adopt a bilinear relation between $\ln v$ and $\ln p$ [e.g. Hashiguchi and Ueno, 1977; Wroth and Houlsby, 1980; Hashiguchi, 1995]. Fig. 1.2(b) shows this relationship graphically, with the slopes of the two linear portions λ and k, as indicated.

The $\ln v$–$\ln p$ relationship can now used to develop an elastic–stress strain law, and a hardening equation for p_c, to describe the complete three-dimensional response of the soil under more general loading conditions.

1.5 ELASTIC STRESS-STRAIN LAW

Several different assumptions have been used in the formulation of elastic stress–strain laws for use with the MCC yield surface. Figures 1.2(a) and (b) only describe response under isotropic compression, and additional information is required to define the complete three dimensional behaviour. Typically, a hypoelastic stress–strain relationship is given in rate form:

$$\dot{\boldsymbol{\sigma}} = [K\mathbf{1} \otimes \mathbf{1} + 2\mu\mathbb{I}_{\text{dev}}]\,\dot{\boldsymbol{\varepsilon}}^e \tag{1.11}$$

where K and μ are the bulk modulus and the shear modulus, respectively. The assumed relationship between v and p, from either Figures 1.2(a) or (b), defines a nonlinear expression for the elastic bulk modulus, while a further assumption is required to evaluate the shear modulus.

In the original presentations of the CC [Roscoe and Schofield, 1963] and MCC [Roscoe and Burland, 1968] models, it was assumed that elastic shear strains were zero. This is equivalent to the assumption of an infinite shear modulus in (1.11), which leads to difficulties in both the conceptual understanding and the computational modelling. Later developments have assumed a fixed value for either the elastic shear modulus [e.g. Wroth and Houlsby, 1985] or Poisson's ratio [e.g. Borja and Lee, 1990]. The former assumption is not realistic for soils, for which the shear stiffness tends to increase with increasing pressure, while the latter assumption has been shown to lead to a non-energy conserving stress–strain relation [Zytinsky *et al.*, 1978]. This implies that for closed strain cycles, energy may be accumulated or dissipated by the model.

Conservation of energy can be guaranteed by postulating a free energy, and obtaining the stress–strain law by differentiating with respect to the strain. Houlsby [1985] proposed the following free energy:

$$W(\boldsymbol{\varepsilon}^e) = p_0 k \exp\left(\frac{\theta^e}{k}\right)\left(1 + \frac{\alpha}{k}\|\mathbf{e}^e\|^2\right) \tag{1.12}$$

where p_0, α and k are model constants, representing the initial pressure (p_0) and some measure of the elastic shear and volumetric stiffnesses (α and k).

Differentiation of (1.12) with respect to the elastic strain leads to a hyperelastic relation between stress and elastic strain:

$$\boldsymbol{\sigma} = \frac{\partial W}{\partial \boldsymbol{\varepsilon}^e} = p_0 \exp\left(\frac{\theta^e}{k}\right)\left[\left(1 + \frac{\alpha}{k}\|\mathbf{e}^e\|^2\right)\mathbf{1} + 2\alpha\mathbf{e}^e\right] \tag{1.13}$$

Under isotropic compression($\|\mathbf{e}^e\| = \|\mathbf{s}\| = 0$) Eq. (1.13) gives the $\ln v$–$\ln p$ bilinear relationship discussed above. Furthermore, the accuracy of Eq. (1.13) under more general loading paths has been evaluated experimentally by Borja *et al.* [1997], and shown to give a good response.

1.6 HARDENING

The evolution of the hardening parameter, p_c, consistent with Fig. 1.2(b), may be described by the following expression:

$$p_c = p_{c0} \exp\left(\frac{\theta^p}{\lambda - k}\right) \tag{1.14}$$

where p_{c0} is the initial value of p_c. This is a non-associative hardening equation, since:

$$\dot{p_c} = \frac{p_c}{\lambda - k}\dot{\theta^p} \quad \neq \quad \frac{\partial f}{\partial p_c} \tag{1.15}$$

where f is the MCC yield function defined by Eq. (1.8).

With an associative plastic flow rule, for which the plastic strain increment is in the direction of the gradient to the yield surface, Eq. (1.14) leads to hardening (expansion of the yield surface) for $p > p_c/2$, and softening (contraction of the yield surface) for $p < p_c/2$. If we consider a stress trajectory for which $p > p_c/2$ is kept constant and $\|\mathbf{e}\|$ increased, the yield surface will continue to increase in size until the CSL is reached. At this point, the normal to the yield surface will be vertical in the p–q plane, and the volumetric component of the plastic strain rate will be zero. Similarly, for constant $p < p_c/2$, the yield surface will shrink until the stress point lies on the CSL, and volume change is zero. Conceptually, this provides a good model of the 'critical state concept' of geomechanics [Roscoe *et al.*, 1958].

1.7 CYCLIC LOADING RESPONSE

Combined with the elastic stress–strain relationship, isotropic hardening laws, and associative flow discussed above, the MCC yield function, Eq. (1.8) has been employed very successfully in the modelling of saturated clays, under *monotonic* loading.

Cyclic loading, however, presents further difficulties. The hysteretic behaviour of soil is not properly described by the MCC model, and several possible modifications have been suggested. One of the most successful is the Bounding Surface model (BS) proposed by Dafalias and Herrmann [1982]. The BS framework considers a 'bounding surface' enclosing all admissible stress states, with a radial projection rule defining a mapping of the current stress state onto this surface. The plastic modulus at any point within the surface is a function of the distance of the point from the bounding surface; generally, as the stress state approaches the bounding surface, the soil goes through a transition from completely elastic to completely plastic response. A recent BS formulation, with several additional features to those described here, will be discussed further in Chapter 3.

The BS Model is very similar conceptually to the 'Generalised Plasticity Model' (GP) presented by Auricchio *et al.* [1992] and Lubliner *et al.* [1993]. In this framework, a yield function defines the boundary between elastic and inelastic states, while a separate 'limit function' defines admissible and inadmissible states.

With the choice of an appropriate limit function, a smooth transition from elastic to inelastic behaviour, as described for the BS model, may be obtained. However, the GP framework may also offer more flexibility, and different forms of the limit function could be used to give a more suitable response for soils. A first attempt to apply the GP model to soils is presented in Chapter 4. Comparisons are made between the monotonic and cyclic response of the three models, and the applicability to soil plasticity problems discussed.

2. MODIFIED CAM-CLAY PLASTICITY

2.1 INTRODUCTION

The Modified Cam-Clay (MCC) model presented in this section is a small-strain adaptation of the finite-strain model presented by Callari *et al.* [1998]. The time continuous version of the model is developed directly from the considerations presented in Chapter 1, and includes an elliptical MCC yield surface with associative flow, a hardening equation based on linear $\ln v$–$\ln p$ relations, and a nonlinear hyperelastic stress–strain law.

A time discrete version of the MCC model is also developed, for use in a finite element setting. A return map algorithm is employed, and a consistent tangent obtained for both elastic and inelastic time steps. The solution algorithm is tested with several numerical examples, including monotonic and cyclic loading conditions.

In [Callari *et al.*, 1998], objections to the use of small-strain MCC models with linear $\ln v$–$\ln p$ relations are raised, based on theoretical considerations and observations of the real behaviour of clays. However, it is suggested in the following that these objections may be insignificant for a range of strain levels generally considered within a small-strain hypothesis. Although small strains have been assumed here, the extension to finite strains can be obtained in a multiplicative elasto-plastic framework, following Callari *et al.* [1998].

2.2 MODEL DESCRIPTION

2.2.1 Elastic stress-strain law

The stress–strain relation of Houlsby [1985], Eq. (1.12), is used here. This may be decomposed into volumetric and deviatoric parts, giving:

$$p = p_0 \exp\left(\frac{\theta^e}{k}\right)\left(1 + \frac{\alpha}{k}\left\|\mathbf{e}^e\right\|^2\right) \tag{2.1}$$

and

$$\mathbf{s} = 2\alpha p_0 \exp\left(\frac{\theta^e}{k}\right)\mathbf{e}^e \tag{2.2}$$

respectively.

2.2.2 Yield surface and flow rule

The MCC yield surface (1.8) is used, i.e.:

$$f(\boldsymbol{\sigma}, p_c) = \frac{3\|\mathbf{s}\|^2}{2M^2} + p(p - p_c) = 0 \tag{2.3}$$

Eq. (2.3) is used in conjunction with an associative plastic flow rule; accordingly, we obtain:

$$\dot{\boldsymbol{\varepsilon}}^p = \dot{\gamma}\frac{\partial f(\boldsymbol{\sigma}, p_c)}{\partial \boldsymbol{\sigma}} = \dot{\gamma}\left[\frac{1}{3}(2p - p_c)\mathbf{1} + \frac{3}{M^2}\mathbf{s}\right] \tag{2.4}$$

where $\dot{\gamma}$ is the continuous consistency parameter, which must satisfy the Kuhn-Tucker conditions:

$$\dot{\gamma} \geq 0 \qquad f(\boldsymbol{\sigma}, p_c) \leq 0 \qquad \dot{\gamma} f(\boldsymbol{\sigma}, p_c) = 0 \tag{2.5}$$

The decomposition of (2.4) into deviatoric and volumetric components gives:

$$\begin{aligned} \dot{\mathbf{e}}^p &= \dot{\gamma}\left(\frac{3}{M^2}\mathbf{s}\right) \\ \dot{\theta}^p &= \dot{\gamma}\,(2p - p_c) \end{aligned} \tag{2.6}$$

2.2.3 Hardening law and plastic modulus

As discussed in Chapter 1, an evolutionary equation for the hardening parameter, p_c, equivalent to the bilogarithmic isotropic compression behaviour, is:

$$p_c = p_{c0} \exp\left(\frac{1}{\lambda - k}\theta^p\right) \tag{2.7}$$

Although it will not be used directly in the following, it will be insightful to evaluate the plastic hardening modulus, $\mathcal{H}$, for the current model. The following expression is used [Lubliner, 1990]:

$$\mathcal{H} = -\frac{1}{\dot{\gamma}} \frac{\partial f}{\partial p_c} \dot{p_c} \tag{2.8}$$

The partial derivative in (2.8) can be determined by differentiating (2.3), giving:

$$\frac{\partial f}{\partial p_c} = -p \tag{2.9}$$

Substituting (1.15) and (2.9) into (2.8) gives an expression for the plastic modulus:

$$\mathcal{H} = \frac{p p_c (2p - p_c)}{\lambda - k} \tag{2.10}$$

Eq. (2.10) shows that hardening ($\mathcal{H} > 0$) will occur when $p > p_c/2$, while softening ($\mathcal{H} < 0$) is predicted for $p < p_c/2$. As discussed in Section 1.6, this is compatible with the critical state concept of geomechanics, in which the volumetric strain rate tends to zero under the application of deviatoric strain.

2.3 DISCRETE FORM OF MODEL

For use in the finite element method, the model must be cast into a time discrete setting. A backward Euler implicit scheme is adopted to integrate the strain evolutionary equations (2.6) to give:

$$\begin{aligned} \mathbf{e}^p &= \mathbf{e}^p_n + \Delta\gamma \frac{3}{M^2}\mathbf{s} \\ \theta^p &= \theta^p_n + \Delta\gamma(2p - p_c) \end{aligned} \tag{2.11}$$

with

$$\Delta\gamma = \int_{t_n}^{t_{n+1}} \dot{\gamma} \mathrm{d}t$$

where the subscript n refers to a value at time t_n, while no subscript refers to time t_{n+1}.

The discrete consistency parameter, $\Delta\gamma$, must satisfy the discrete form of the Kuhn-Tucker conditions:

$$\Delta\gamma \geq 0 \qquad f(\boldsymbol{\sigma}, p_c) \leq 0 \qquad \Delta\gamma f(\boldsymbol{\sigma}, p_c) = 0 \tag{2.12}$$

which are used as the basis of the return mapping algorithm discussed in Section 2.4.

Substituting (2.11) into (2.1) and (2.2) gives:

$$p = p_0 \exp\left(\frac{\theta - \theta^p_n - \Delta\gamma(2p - p_c)}{k}\right)\left[1 + \frac{\alpha}{k}\|\mathbf{e} - \mathbf{e}^p_n - \Delta\gamma\frac{3}{M^2}\mathbf{s}\|^2\right] \tag{2.13}$$

and

$$\mathbf{s} = 2\alpha p_0 \exp\left(\frac{\theta - \theta^p_n - \Delta\gamma(2p - p_c)}{k}\right)\left[\mathbf{e} - \mathbf{e}^p_n - \Delta\gamma\frac{3}{M^2}\mathbf{s}\right] \tag{2.14}$$

Collecting $\mathbf{s}$ terms in (2.14) leads to:

$$\mathbf{s} = \frac{2\alpha p_0 \exp\left(\frac{\theta-\theta_n^p}{k}\right)\exp\left(\frac{-\Delta\gamma(2p-p_c)}{k}\right)}{1+\frac{6\alpha p_0}{M^2}\Delta\gamma\exp\left(\frac{\theta-\theta_n^p}{k}\right)\exp\left(\frac{-\Delta\gamma(2p-p_c)}{k}\right)}[\mathbf{e}-\mathbf{e}_n^p] \tag{2.15}$$

2.4 RETURN MAP ALGORITHM

The time discrete formulation of the previous section can be conveniently solved using a return map algorithm. The methodology is summarised below, while details are presented in the following sections.

1. A trial elastic state is determined, with the discrete consistency parameter set to zero.
2. The yield function, (2.3) is evaluated for the trial values.
3. If the discrete Kuhn-Tucker conditions are satisfied, then the trial values are correct, and the time step is elastic as assumed; otherwise a plastic correction is made to the trial state.

2.4.1 Trial state

An elastic trial state is obtained by setting the discrete consistency parameter to zero, equivalent to freezing plastic flow over the time step. From Equations (2.7), (2.11), (2.13) and (2.14), the following trial state values are obtained:

$$\begin{cases} \Delta\gamma^{tr} = 0 \\ \mathbf{e}^{e,tr} = \mathbf{e} - \mathbf{e}_n^p \\ \theta^{e,tr} = \theta - \theta_n^p \\ \mathbf{s}^{tr} = 2\alpha p_0 \exp\left(\dfrac{\theta^{e,tr}}{k}\right)\mathbf{e}^{e,tr} \\ p^{tr} = p_0 \exp\left(\dfrac{\theta^{e,tr}}{k}\right)\left(1+\dfrac{\alpha}{k}\|\mathbf{e}^{e,tr}\|^2\right) \\ p_c^{tr} = p_{c0}\exp\left(\dfrac{\theta_n^p}{\lambda-k}\right) \end{cases} \tag{2.16}$$

where the superscript 'tr' indicates a trial state value.

The trial values are substituted into (2.3) to give the trial yield function:

$$f^{tr}(\boldsymbol{\sigma}^{tr}, p_c^{tr}) = \frac{3\|\mathbf{s}^{tr}\|^2}{2M^2} + p^{tr}(p^{tr} - p_c^{tr}) \tag{2.17}$$

This is compared to the second Kuhn-Tucker condition, $(2.12)_2$. If $f^{tr} \leq 0$ then the trial state is the correct solution, and the time step is elastic, as assumed. Otherwise, if $f^{tr} > 0$, the Kuhn-Tucker condition is violated, and a plastic correction must be made to obtain the correct stress state.

2.4.2 Plastic Correction

The trial state values (2.16) are substituted into the general time discrete equations (2.11), (2.13) and (2.14) from which we obtain the following plastic corrections:

$$\begin{cases} \mathbf{e}^p = \mathbf{e}^{p,tr} + \dfrac{3\Delta\gamma}{M^2}\mathbf{s} \\ \theta^p = \theta^{p,tr} + \Delta\gamma(2p - p_c) \\ \mathbf{s} = \mathbf{s}^{tr} \exp\left(\dfrac{-\Delta\gamma}{k}(2p - p_c)\right) \\ \quad \left[1 + \dfrac{6\alpha p_0}{M^2}\Delta\gamma \exp\left(\dfrac{\theta - \theta_n^p}{k}\right) \exp\left(\dfrac{-\Delta\gamma}{k}(2p - p_c)\right)\right]^{-1} \\ p = p_0 \exp\left(\dfrac{\theta^{e,tr}}{k}\right) \exp\left(\dfrac{-\Delta\gamma}{k}(2p - p_c)\right) \\ \quad \left[1 + \dfrac{\alpha}{k}\left(\|\mathbf{e}^{e,tr}\|^2 - \dfrac{6}{M^2}\Delta\gamma\mathbf{s} : \mathbf{e}^{e,tr} + \dfrac{9}{M^4}\Delta\gamma^2\|\mathbf{s}\|^2\right)\right] \end{cases} \tag{2.18}$$

The yield condition (2.3) and the hardening equation (2.7) must also be satisfied. From the latter we obtain:

$$p_c = p_c^{tr} \exp\left(\frac{2p - p_c}{\lambda - k}\Delta\gamma\right) \tag{2.19}$$

The above equations can be simplified by introducing some constants:

$$\begin{cases} A_1 = \exp\left(\dfrac{-\Delta\gamma}{k}(2p - p_c)\right) \\ A_2 = \exp\left(\dfrac{\theta^{e,tr}}{k}\right) \\ A_3 = \dfrac{6\alpha p_0}{M^2}A_2 \\ A_4 = 1 + \Delta\gamma A_1 A_3 \\ A_5 = \dfrac{A_1}{A_4} \\ A_6 = \left\{1 + \dfrac{\alpha}{k}\left(\|\mathbf{e}^{e,tr}\|^2 - \dfrac{6}{M^2}\Delta\gamma\mathbf{s} : \mathbf{e}^{e,tr} + \dfrac{9}{M^4}\Delta\gamma^2\|\mathbf{s}\|^2\right)\right\} \end{cases} \tag{2.20}$$

Equations $(2.18)_3$ and $(2.18)_4$ then simplify to:

$$p = p_0 A_1 A_2 A_6 \tag{2.21}$$

$$\mathbf{s} = A_5 \mathbf{s}^{tr} \tag{2.22}$$

Equations (2.3), (2.19), (2.21) and (2.22) must be solved simultaneously, to determine the plastically-correct stress state. We can minimise the problem dimension by substituting $\mathbf{s}$ from (2.22) into the other three equations, reducing the unknowns to three independent variables. In particular, we may define the

vector of unknowns, $\boldsymbol{x}$, and vector of residuals, $\mathbf{g}(\boldsymbol{x})$:

$$\boldsymbol{x} = \begin{Bmatrix} p \\ p_c \\ \Delta\gamma \end{Bmatrix} \; ; \quad \mathbf{g}(\boldsymbol{x}) = \begin{Bmatrix} g_1 \\ g_2 \\ g_3 \end{Bmatrix} = \begin{Bmatrix} \frac{3\|\mathbf{s}\|^2}{2M^2} + p(p - p_c) \\ p_c^{tr} \exp\left(\frac{2p - p_c}{\lambda - k}\Delta\gamma\right) - p_c \\ p_0 A_1 A_2 A_6 - p \end{Bmatrix} \tag{2.23}$$

Taking trial state (2.16) as the initial value of $\boldsymbol{x}$, we iterate using a Newton algorithm, such that the value from the $(k+1)^{\text{th}}$ iteration is found from:

$$\boldsymbol{x}^{(k+1)} = \boldsymbol{x}^{(k)} - \left[\frac{\partial \mathbf{g}}{\partial \boldsymbol{x}}\right]^{-1} \mathbf{g}\left(x^{(k)}\right) \tag{2.24}$$

and convergence is achieved when the normalised residual vector is less than machine tolerance:

$$\|\mathbf{g}\|^* = \sqrt{\left(\frac{g_1}{p_0^2}\right)^2 + \left(\frac{g_2}{p_0}\right)^2 + \left(\frac{g_3}{p_{c0}}\right)^2} < TOL \tag{2.25}$$

To make use of the Newton algorithm (2.24), the residual gradient $\partial\mathbf{g}/\partial\boldsymbol{x}$ must be calculated. This calculation is presented in Appendix A. Note also that the residual gradient must be inverted numerically for use in (2.24), although the reduction of the problem dimension from the elimination of $\mathbf{s}$ significantly reduces the computational effort in the inversion.

2.4.3 Consistent tangent

If the model is to be used in a finite element setting, a consistent tangent tensor must be calculated, by linearising the time discrete forms of the equations presented previously. Use of a tangent tensor consistent with the discretisation preserves the quadratic convergence of the model.

Elastic Step

If the trial values are correct, and the step is elastic, calculation of the consistent tangent is relatively straightforward. Linearising the expressions for p and $\mathbf{s}$ ((2.21) and (2.22), respectively) gives:

$$\mathrm{d}p = p_0 \left[\frac{1}{k}\exp\left(\frac{\theta^e}{k}\right)\left(1 + \frac{\alpha}{k}\|\mathbf{e}^e\|^2\right)\mathbf{1} + \frac{2\alpha}{k}\exp\left(\frac{\theta^e}{k}\right)\mathbf{e}^e\right]\mathrm{d}\boldsymbol{\varepsilon} \tag{2.26}$$

$$\mathrm{d}\mathbf{s} = 2\alpha p_0 \left[\frac{1}{k}\exp\left(\frac{\theta^e}{k}\right)\mathbf{e}^e \otimes \mathbf{1} + \exp\left(\frac{\theta^e}{k}\right)\mathbb{I}_{\text{dev}}\right]\mathrm{d}\boldsymbol{\varepsilon} \tag{2.27}$$

From the combination of (2.27) and (2.26), we obtain :

$$\begin{aligned}\mathbb{C}^{\text{e}} &= \frac{\partial\boldsymbol{\sigma}}{\partial\boldsymbol{\varepsilon}} = \mathbf{1} \otimes \frac{\partial p}{\partial\boldsymbol{\varepsilon}} + \frac{\partial \mathbf{s}}{\partial\boldsymbol{\varepsilon}} \\ &= \frac{p_0}{k}\exp\left(\frac{\theta^e}{k}\right)\left[2\alpha k\mathbb{I}_{\text{dev}} + 3\left(1 + \frac{\alpha}{k}\|\mathbf{e}^e\|^2\right)\mathbb{I}_{\text{vol}} + 2\alpha\left(\mathbf{1} \otimes \mathbf{e}^e + \mathbf{e}^e \otimes \mathbf{1}\right)\right]\end{aligned} \tag{2.28}$$

Plastic Step

The plastic consistent tangent must be obtained by linearising the plastically-corrected model variables. We obtain the tangent from:

$$\mathbb{C}^{\mathrm{p}} = \frac{\partial \boldsymbol{\sigma}}{\partial \boldsymbol{\varepsilon}} = \mathbf{1} \otimes \frac{\partial p}{\partial \boldsymbol{\varepsilon}} + \frac{\partial \mathbf{s}}{\partial \boldsymbol{\varepsilon}} \tag{2.29}$$

Noting that $\partial \boldsymbol{\varepsilon}^{e,tr} / \partial \boldsymbol{\varepsilon} = \mathbb{I}$, (2.29) becomes:

$$\mathbb{C}^{\mathrm{p}} = \mathbf{1} \otimes \frac{\partial p}{\partial \boldsymbol{\varepsilon}^{e,tr}} + \frac{\partial \mathbf{s}}{\partial \boldsymbol{\varepsilon}^{e,tr}} \tag{2.30}$$

Equations (2.19), (2.21) and (2.22) are differentiated with respect to the trial elastic strain tensor, $\boldsymbol{\varepsilon}^{e,tr}$, giving three equations in four unknown differentials. The remaining unknown differential, $\partial \Delta\gamma / \partial \boldsymbol{\varepsilon}^{e,tr}$, is obtained by enforcing the consistency condition on the yield surface. The complete calculation of the consistent tangent is given in Appendix B, in which the following expression is obtained:

$$\mathbb{C}^{\mathrm{p}} = E_1 \mathbf{1} \otimes \mathbf{s} + E_2 \mathbf{1} \otimes \mathbf{1} + E_3 \mathbf{s} \otimes \mathbf{1} + E_4 \mathbf{s} \otimes \mathbf{s} + E_5 \mathbb{I}_{\mathrm{dev}} \tag{2.31}$$

where the values of E_1–E_5 are given in Appendix B.

Remark 2.1. Note that (2.31) is derived in terms of the deviatoric stress tensor, $\mathbf{s}$. It may be preferable to express the tangent tensor directly as a function of the elastic trial strain, $\boldsymbol{\varepsilon}^{e,tr}$; in this case $(2.16)_4$ and (2.22) may be used in the conversion.

2.4.4 Converting to 'mechanical' sign convention

Solid mechanics generally operates under the convention that tensile stresses and strains are positive. For soils, compression is of more interest, and this is usually taken as positive. Accordingly, it may be convenient, or necessary in some cases, to convert an expression from a geotechnical sign convention to a solid mechanics convention.

It is trivial to change the sign of the appropriate components of the stress and strain tensors. However, the tangent matrix must also be altered to remain consistent with the discretisation. The appropriate expression can be obtained from the chain rule; within either the geotechnical or mechanical sign conventions, we have:

$$\begin{aligned} \boldsymbol{\varepsilon}^{m/g} &= \mathbf{e}^{m/g} + \frac{\theta^{m/g}}{3}\mathbf{1} \\ \boldsymbol{\sigma}^{m/g} &= \mathbf{s}^{m/g} + p^{m/g}\mathbf{1} \end{aligned} \tag{2.32}$$

where m and g superscripts refer to 'mechanical' and 'geotechnical' sign convention respectively. From the definitions of the sign conventions, we also have:

$$\begin{aligned} \theta^m &= -\theta^g & \qquad \mathbf{e}^m &= \mathbf{e}^g \\ p^m &= -p^g & \qquad \mathbf{s}^m &= \mathbf{s}^g \end{aligned} \tag{2.33}$$

Therefore, (2.32) and (2.33) give:

$$\begin{aligned} \boldsymbol{\varepsilon}^m &= \mathbf{e}^g - \frac{\theta^g}{3}\mathbf{1} \\ \boldsymbol{\sigma}^m &= \mathbf{s}^g - p^g\mathbf{1} \end{aligned} \tag{2.34}$$

Finally, we can evaluate the elastic and plastic consistent tangents from the chain rule:

$$\begin{aligned} \mathbb{C}^{\mathrm{p},m} &= \frac{\partial \boldsymbol{\sigma}^m}{\partial \boldsymbol{\varepsilon}^m} = \frac{\partial \boldsymbol{\sigma}^m}{\partial \boldsymbol{\varepsilon}^g} : \frac{\partial \boldsymbol{\varepsilon}^g}{\partial \boldsymbol{\varepsilon}^m} \\ &= \left[\frac{\partial \mathbf{s}^g}{\partial \boldsymbol{\varepsilon}^g} - \mathbf{1} \otimes \frac{\partial p^g}{\partial \boldsymbol{\varepsilon}^g}\right] : [\mathbb{I}_{\mathrm{dev}} - \mathbb{I}_{\mathrm{vol}}] \end{aligned} \tag{2.35}$$

Reevaluating (2.28) and (2.31) using the above expression gives the tangent tensors to be used with the mechanical (tension positive) sign convention:

$$\mathbb{C}^{\mathrm{e},m} = \frac{p_0}{k} \exp\left(\frac{\theta^e}{k}\right) \left[2\alpha k \mathbb{I}_{\mathrm{dev}} + 3\left(1 + \frac{\alpha}{k}\|\mathbf{e}^e\|^2\right)\mathbb{I}_{\mathrm{vol}} - 2\alpha\left(\mathbf{1} \otimes \mathbf{e}^e + \mathbf{e}^e \otimes \mathbf{1}\right)\right] \tag{2.36}$$

and

$$\mathbb{C}^{\mathrm{p},m} = -E_1\mathbf{1} \otimes \mathbf{s} + E_2\mathbf{1} \otimes \mathbf{1} - E_3\mathbf{s} \otimes \mathbf{1} + E_4\mathbf{s} \otimes \mathbf{s} + E_5\mathbb{I}_{\mathrm{dev}} \tag{2.37}$$

where the constant terms are defined as before, (B.39).

2.5 NUMERICAL TESTS

The MCC model was implemented in the Finite Element Analysis Program (FEAP) [Taylor, 2000], and several numerical simulations were carried out. The work of Callari *et al.* [1998] was used as a reference for some laboratory test simulations, and stress and strain controlled cyclic shear tests were also considered.

A three-dimensional isoparametric eight node element was used in each of the simulations. The material properties that were used in each test are as indicated in Table 2.1, except where stated in the description of the test.

The remaining material parameter, p_0, varies for each simulation, and is set equal to the initial mean pressure imposed on the element. Note that p_0 cannot equal zero, as this would lead to zero stress from (1.13). That is, the reference strain $\boldsymbol{\varepsilon} = \mathbf{0}$, must correspond to a non-zero reference pressure, p_0.

Table 2.1: Modified Cam-Clay model parameters

Parameter	α	M	λ	k	p_{c0}
Value	100	0.9	0.09	0.02	100 kPa

All tests are considered to take place under drained loading conditions, such that excess pore water pressure does not develop.

2.5.1 Isotropic compression test

An isotropic compression test was modelled under full stress control. From an initial state of normal consolidation ($p_0 = p_{c0} = 100$ kPa), the sample was loaded monotonically, by increasing axial stress components $\sigma_{11} = \sigma_{22} = \sigma_{33}$. This was followed by an unloading stage, and finally reloading into the plastic range.

Fig. 2.1(a) shows the loading, unloading and reloading behaviour of the model under isotropic compression. Results are shown for six, 100 and 1000 stress increments, and the accuracy of the solution algorithm can be observed, even for relatively large steps.

Fig. 2.1(b) confirms the bilinear $\ln v$–$\ln p$ relationship used in the development of the model. Comparing with Fig. 1.4(b) and Table 2.1, it is clear that the correct gradients, λ and k, have been obtained. A reference value of $v_0 = 2.5$ was assumed here, although this affects only the position on the axes, and not the shape of the curve.

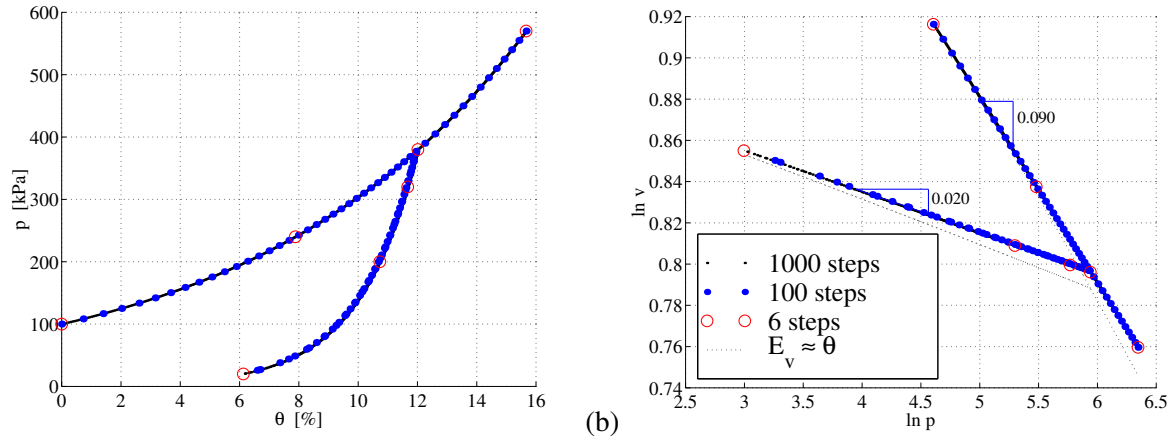

Figure 2.1: Isotropic compression test. (a) Volumetric stress, p, vs. volumetric strain, θ, and (b) bilinear $\ln v$ vs. $\ln p$ relationship.

Convergence profiles were also plotted for the 100-step and 6-step analyses. In Fig. 2.2(a), the logarithm of the normalised residual ($\log R_i$) is plotted versus the iteration number for the first, last and 'worst' time steps. The 'worst' step is defined as that with the maximum number of iterations required to converge, and with the slowest final rate of convergence. With 100 time steps, all steps converged within six iterations, while with 6 time steps, one time step required ten iterations to converge to the required tolerance, $TOL = 1 \times 10^{-16}$.

Fig. 2.2(b) shows the ratio of successive $\log R_i$ values, for the worst time step only. This ratio tends to a value of two in both cases, confirming the quadratic convergence of the model.

Remark 2.2. Callari *et al.* [1998] show that making use of the infinitesimal-strain hypothesis with a bilinear $\ln v$–$\ln p$ relation is an inconsistent approach. An implicit assumption in such a model is that the

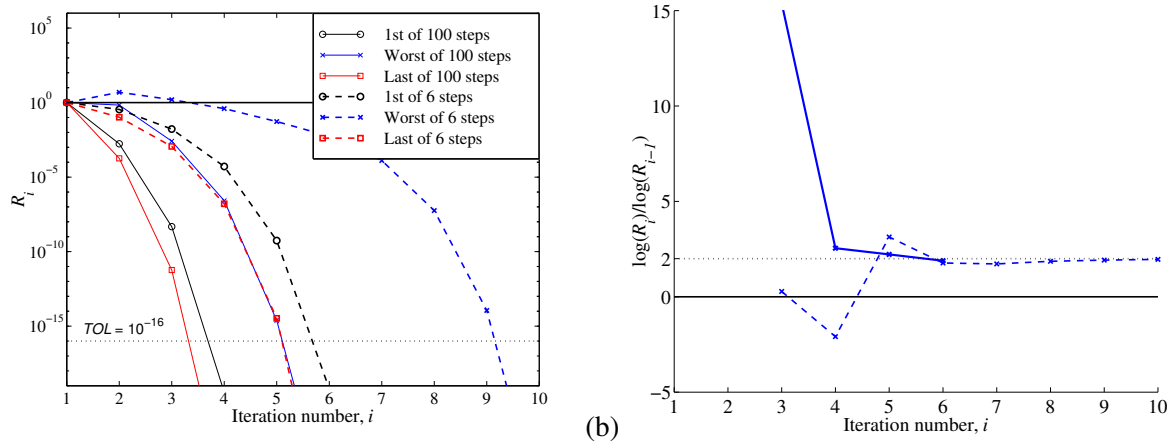

(a) (b)

Figure 2.2: Isotropic compression test. Convergence profiles of (a) normalised residual, R_i, and (b) ratio of successive logarithms, $\log R_i$.

volumetric strain defined according to:

$$E_v = -\frac{v - v_0}{v_0} \tag{2.38}$$

is approximately equal to the logarithmic volumetric strain, $\theta = \ln(v/v_0)$, as defined in (1.10).

In the present model v has not been used as a variable, and the values in Fig. 2.1(b) have been calculated from (1.10). However, it is interesting to compare the values we obtain if (2.38), and the assumption that $E_v \approx \theta$, is used to calculate v. This is shown as a dotted line on Fig. 2.1(b), which shows slight deviation from the bilinear $\ln v$–$\ln p$ relationship. However, the maximum deviation of $\ln v$ is less than two per cent, which corresponds to approximately one per cent error in v.

Clearly, this error will increase with increasing θ, although use of the small-strain hypothesis beyond $\theta = 15\%$ is not common practice. This suggests that the small-strain approach is adequate for the applications presented here, despite an apparent inconsistency in its definition.

2.5.2 Triaxial compression of lightly overconsolidated sample

A triaxial compression test was simulated. Initially, the element was loaded isotropically from $p_0 = 10$ kPa to $p = 80$ kPa, with $p_{c0} = 100$ kPa, as reported in Table 2.1. At this stage, the soil sample could be considered lightly overconsolidated, with an overconsolidation ratio (OCR $= p_{c0}/p$) of 1.25. Following isotropic loading, stress components $\sigma_{22} = \sigma_{33}$ were held constant at 80 kPa, while axial strain ε_{11} was increased until the CSL was reached.

Fig. 2.3(a) shows the overall loading history in p–q space, together with the initial ($f_0 = 0$) and final ($f_1 = 0$) yield surfaces. The yield surface continues to grow with increasing p and q, until the CSL is reached. At this point, no further stress increment can be sustained (Figures 2.3(b) and 2.3(c)), and the

volumetric strain increment is zero (Fig. 2.3(d)). In Figures 2.3(c) and 2.3(d), ε_q is a measure of the deviatoric strain, defined as:

$$\varepsilon_q = \sqrt{\frac{2}{3}}\|\mathbf{e}\| \tag{2.39}$$

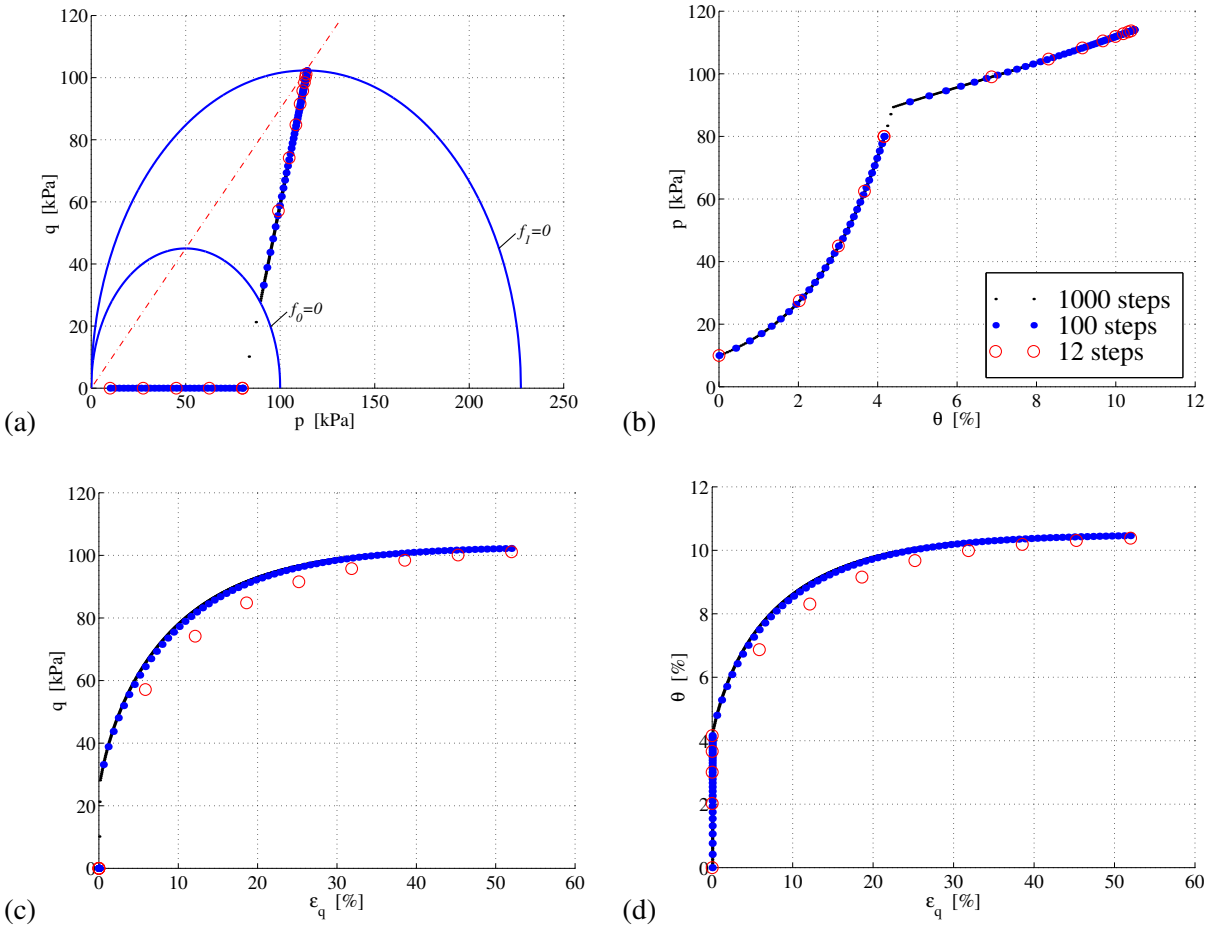

Figure 2.3: Triaxial compression of lightly overconsolidated sample. (a) Stress path on p–q diagram, (b) volumetric stress, p, vs. volumetric strain, θ, (c) deviatoric stress, q, vs. deviatoric strain, ε_q, and (d) θ vs. ε_q.

Three different stress increments were used in the analyses, corresponding to 1000, 100 and 12 integration steps. Assuming 1000 steps gives an accurate solution, Figures 2.3(c) and 2.3(d) show nearly exact correlation for 100 steps and a slight deviation from exact for 12 steps.

Convergence profiles are compared for 100 and 12 integration steps in Figures 2.4(a) and (b). As before, the solution algorithm leads to asymptotic quadratic convergence, as shown for the 'worst' time step for each case, in Fig. 2.4(b).

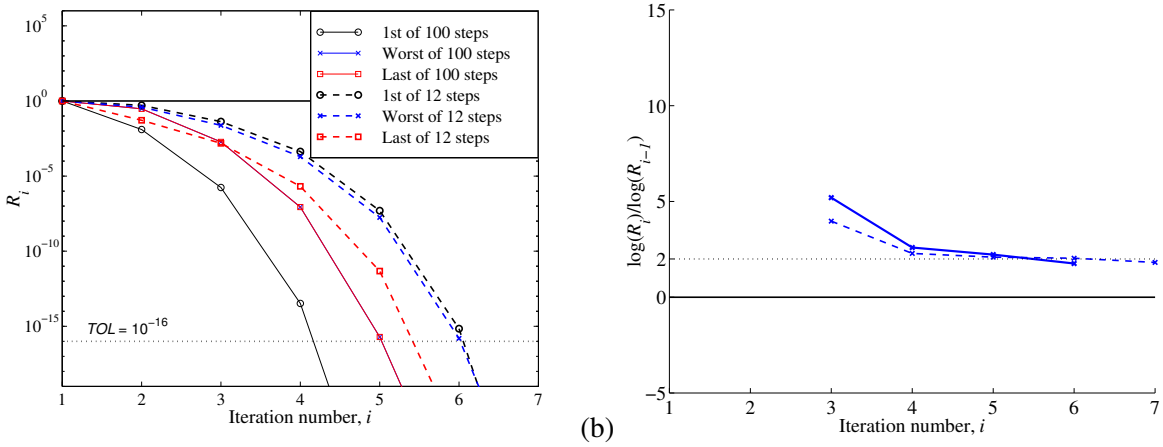

(a) (b)

Figure 2.4: Triaxial compression of lightly overconsolidated sample. Convergence profiles of (a) normalised residual, R_i, and (b) ratio of successive logarithms, $\log R_i$.

2.5.3 Triaxial compression of heavily overconsolidated sample

The same procedure as above was repeated, with the initial stage of isotropic compression from $p_0 = 10$ kPa to $p = 20$ kPa. This could be considered a heavily consolidated sample, with OCR $= 5$.

As noted by Callari *et al.* [1998], the MCC model presented here is intended for normally consolidated and lightly overconsolidated clays only. Therefore, the numerical test in this section is intended only to check the solution algorithm in the case of softening.

Test results are presented in Fig. 2.5. In Fig. 2.5(a), p and q continue to increase until the initial yield surface is reached, at which point softening takes place. In terms of volumetric strain (Fig. 2.5(b)), the sample dilates ($\dot{\theta} > 0$) in the elastic range, and contracts ($\dot{\theta} < 0$) after yield. As before, when the CSL is reached, stress and volumetric strain remains unchanged with increasing deviatoric strain (Figures 2.5(c) and 2.5(d)).

Again, three different stress increments were used in the analyses, corresponding to 1000, 100 and 18 integration steps. Assuming 1000 steps gives an accurate solution, Figures 2.5(c) and 2.5(d) show nearly exact correlation for 100 steps and a slight deviation from exact for 18 steps.

Convergence profiles are again compared for 100 and 18 integration steps in Figures 2.6(a) and (b). Again, Fig. 2.6(b) shows quadratic convergence for both 100 and 18 steps.

2.5.4 Strain controlled cyclic shear loading

In the strain and stress-controlled cyclic tests considered here, volume is held constant, which corresponds to 'undrained' loading conditions, in which excess pore water pressure is not allowed to dissipate.

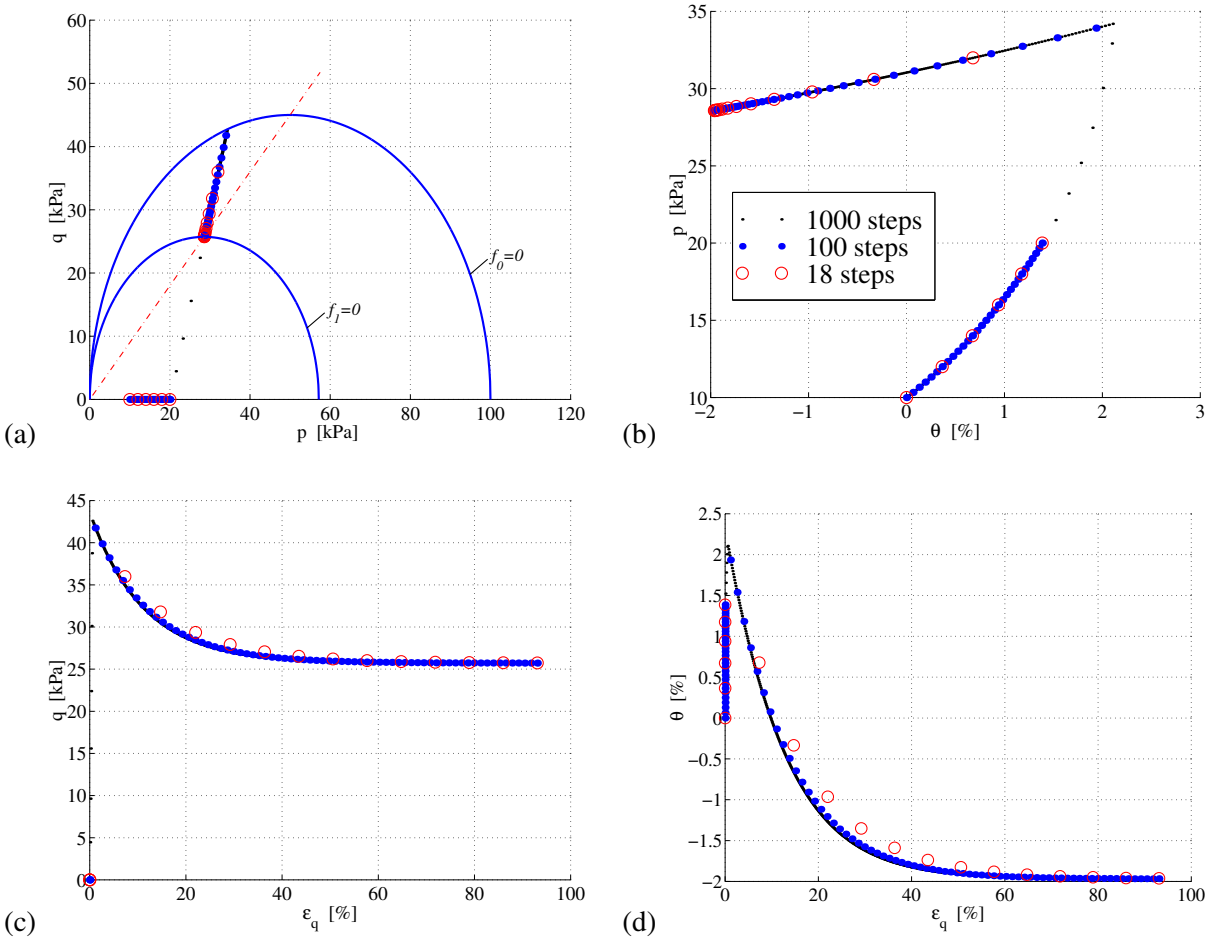

Figure 2.5: Triaxial compression of heavily overconsolidated sample. (a) Stress path on p–q diagram, (b) volumetric stress, p vs. volumetric strain, θ, (c) deviatoric stress, q vs. deviatoric strain, ε_q, and (d) θ vs. ε_q.

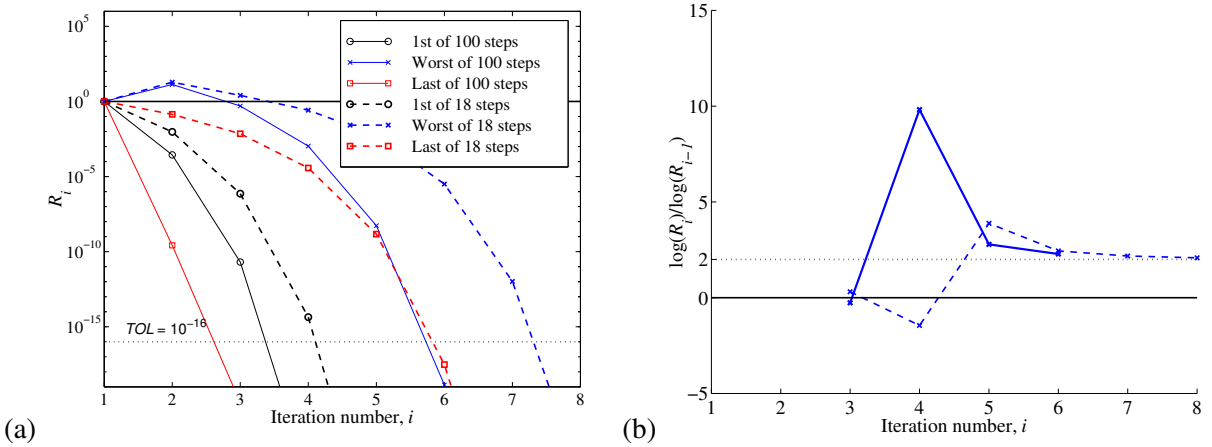

Figure 2.6: Triaxial compression of heavily overconsolidated sample. Convergence profiles of (a) normalised residual, R_i, and (b) ratio of successive logarithms, $\log R_i$.

Furthermore, deviatoric stress (q) and strain (ε_q) will be assumed to carry the sign of the controlled stress or strain component, so that the cyclic behaviour of the model can be more easily visualised.

The first cyclic shear test was carried out under full strain control. Axial strain components (ε_1, ε_2 and ε_3) were fixed at zero, and an initial pressure of $p_0 = 100$ kPa (OCR $= 1$) was assigned. Finally, two adjacent faces of the cubic element were subjected to cyclic shear loading, corresponding to $\varepsilon_{12} = \pm 0.8\%$.

Fig. 2.7(a) shows the stress path in p–q space. The stress history was characterised by inelastic loading and expansion of the yield surface initially, with the stress state tending towards the CSL. Unloading is elastic, with the coupling between volumetric and deviatoric stress components evident in Fig. 2.7(a). Subsequent cycles of reloading exhibit less hardening, as p tends to $p_c/2$, and the plastic modulus tends to zero (Eq. (2.10)).

Fig. 2.7(b) shows the hysteretic response of the sample, with deviatoric stress plotted against deviatoric strain. The figure shows more clearly the gradual reduction in plastic modulus as the sample moves towards the critical state. Also evident in Fig. 2.7(b) is the increase in stress carried by the sample under constant amplitude strain cycles. This result is contrary to observed soil response, for which shear strength degradation is expected under cycling loading.

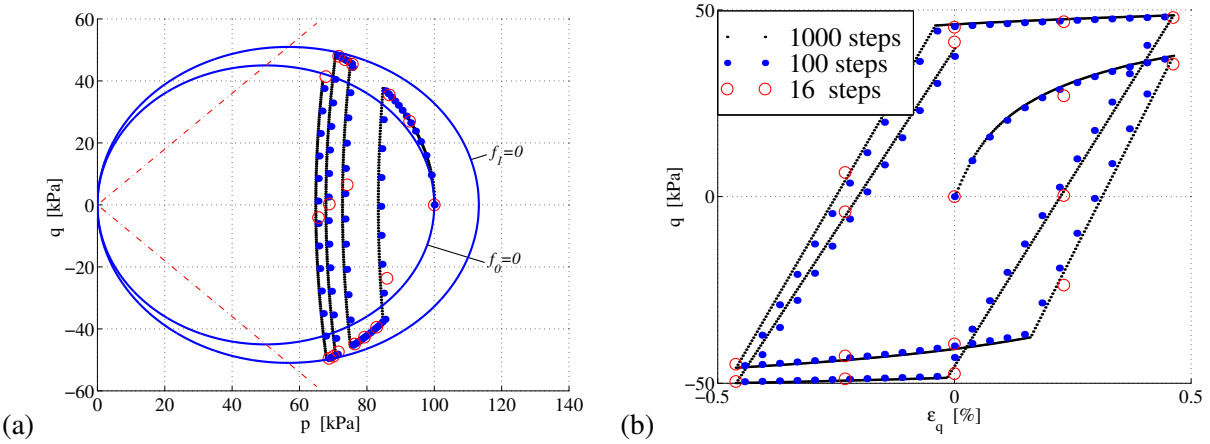

Figure 2.7: Strain controlled cyclic shear test. (a) Stress path on p–q diagram, and (b) deviatoric stress, q vs. deviatoric strain, ε_q

As with the previous cases, the adopted algorithm gives very stable solutions, even for relatively few (16) time steps.

2.5.5 Stress controlled cyclic shear loading

A second cyclic loading test was carried out under shear stress control, with axial strain components again fixed at zero. Initial stress, p_0, was again taken as 100 kPa. One shear component of the stress tensor was cycled with amplitude $\sigma_{12} = \pm 25$ kPa.

Figures 2.8(a) and 2.8(b) show a similar loading response to the strain controlled test. However, as the maximum stress amplitude is kept constant, no further plastic strains develop beyond the first cycle, and

the unloading–reloading stress paths are coincident. No hysteresis loops are exhibited by the model, as no yielding takes place within the yield surface. This is contrary to the observed behaviour or real clays, for which energy is dissipated over successive cycles in hysteretic action.

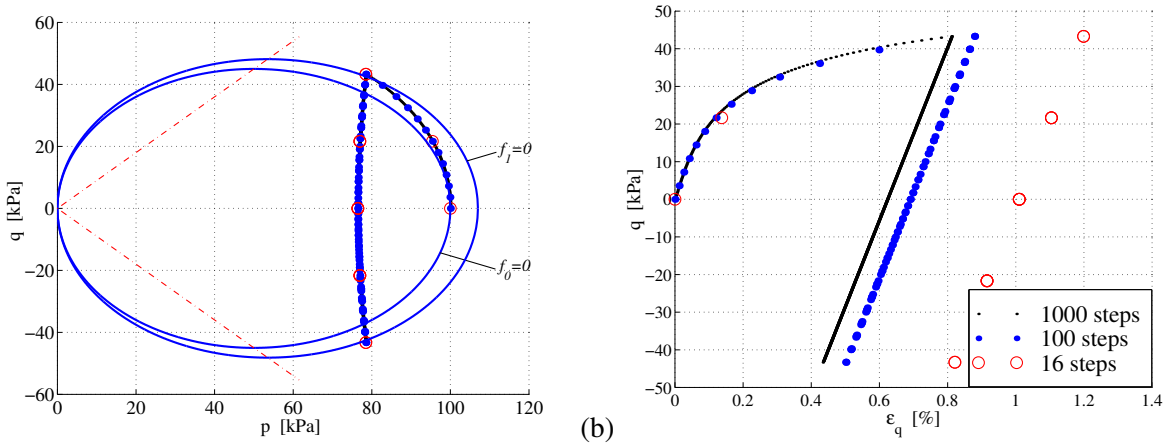

Figure 2.8: Stress controlled cyclic shear test. (a) Stress path on p–q diagram, and (b) deviatoric stress, q vs. deviatoric strain, ε_q

Fig. 2.8(b) shows that under stress control with fixed volume, relatively inaccurate results are obtained, even for a relatively large number of steps (100). The final slope in Fig. 2.8(b) is relatively low, and under stress control, a small change in the gradient can lead to a large overshoot in the converged strain values. Furthermore, in incompressible plasticity, problems are often experienced, and the penalty method [e.g. Hughes, 2000] is commonly used to ensure accuracy of the results. However, this is beyond the scope of the present work, and an additional test with 10000 steps verified the accuracy of the 1000-step solution above.

3. BOUNDING SURFACE PLASTICITY

3.1 INTRODUCTION

The Modified Cam-Clay model summarised in the previous chapter is effective in the modelling of clays under monotonic loading conditions, giving accurate predictions of the plastic volumetric and deviatoric strains developed. However, under cyclic loading the hysteretic behaviour is poorly predicted. As demonstrated in Section 2.5, no strength degradation is exhibited under cyclic shear loading of constant amplitude, and unloading and reloading within the yield surface is always elastic.

A widely adopted formulation for cyclic soil plasticity is the Bounding Surface (BS) model proposed by Dafalias and Herrmann [1982]. In this framework, a 'bounding surface' is defined, which delimits the boundary of admissible stress points in p–q space. Stress states on the bounding surface represent fully plastic response, while a specific point in stress space, the 'homology centre', represents the instantaneous elastic response. Within the bounding surface, hardening equations are defined as a function of the distance from the stress point to the bounding surface, projected radially from the homology centre. In this manner, a smooth transition from elastic behaviour to fully plastic behaviour is observed, as the stress point passes from the homology centre to the bounding surface.

The work of Borja *et al.* [2001] is a recent application of the Bounding Surface framework to soil plasticity. In this work, an elliptical bounding surface in the p–q plane is used, identical to the MCC yield surface of Chapter 2. The hyperelastic stress–strain law of Eq. (1.13) is used, and the hardening equation, (1.14), describes the evolution of the bounding surface. In addition to the isotropic hardening parameter, a kinematic back stress is also defined, based on the location of the homology centre.

The model of Borja *et al.* [2001] is used as a basis for the following developments, converted into the terminology and framework of Chapter 2 where appropriate. A few changes to the solution approach result in a slightly more efficient algorithm. By decomposing the stress tensor into volumetric and deviatoric parts, the number of scalar dimensions in the plastic correction step can be reduced from eight to four.

Furthermore, adopting the same procedure as in Appendix B, the consistent inelastic tangent matrix is calculated without the requirement of matrix inversion.

3.2 MODEL DEVELOPMENT

3.2.1 Elastic stress-strain law

The hyperelastic stress–strain law used in this section is identical to that used in Chapter 2. Decomposed into volumetric and deviatoric components, we have:

$$p = p_0 \exp\left(\frac{\theta^e}{k}\right)\left(1 + \frac{\alpha}{k}\left\|\mathbf{e}^e\right\|^2\right) \tag{3.1}$$

and

$$\mathbf{s} = 2\alpha p_0 \exp\left(\frac{\theta^e}{k}\right)\mathbf{e}^e \tag{3.2}$$

respectively.

3.2.2 Bounding surface and loading surface

Instead of a yield surface, the BS model uses a bounding surface, $F(\hat{\boldsymbol{\sigma}}, p_c) = 0$, to define admissible stress states. The bounding surface is defined by:

$$F(\hat{\boldsymbol{\sigma}}, p_c) = \frac{3\|\hat{\mathbf{s}}\|^2}{2M^2} + \hat{p}(\hat{p} - p_c) = 0 \tag{3.3}$$

where p_c is a hardening parameter, representing the intercept of the elliptical surface with the p–axis in p–q space.

The tensor $\hat{\boldsymbol{\sigma}}$ is a mapping of the current stress value, $\boldsymbol{\sigma}$, onto the bounding surface, and $\hat{\mathbf{s}}$ and $\hat{p}$ are its deviatoric and volumetric parts. This mapping is one of the main constituents of the BS formulation, and the first point of departure from the MCC model. Commonly, a radial mapping is considered from a projection point called the 'homology centre', $\boldsymbol{\sigma}_h$:

$$\hat{\boldsymbol{\sigma}} = \boldsymbol{\sigma} + \kappa(\boldsymbol{\sigma} - \boldsymbol{\sigma}_h) \tag{3.4}$$

The variable κ is a measure of the distance of the current stress point from the bounding surface. It may take values between 0, for a stress value located on the bounding surface, and an infinite value, for a stress value at the homology centre. Substituting this expression for $\hat{\boldsymbol{\sigma}}$ into (3.3) gives:

$$\frac{3}{2M^2}\left\|\mathbf{s}(1+\kappa) - \kappa\mathbf{s}_h\right\|^2 + \left[p\,(1+\kappa) - \kappa p_h\right]\left[p\,(1+\kappa) - \kappa p_h - p_c\right] = 0 \tag{3.5}$$

where $\mathbf{s}_h$ and p_h are the deviatoric and volumetric parts of the homology centre, $\boldsymbol{\sigma}_h$, respectively. The initial value of $\boldsymbol{\sigma}_h$ must be defined by the user as another model parameter, and may be taken as $\boldsymbol{\sigma}_{0,i} = \mathbf{0}$ for an initially isotropic soil. Evolution of $\boldsymbol{\sigma}_h$ from the initial position is discussed in Section 3.2.6.

Dividing this expression by $(1+\kappa)^2$ defines a new surface, $f(\tilde{\boldsymbol{\sigma}}, p_l) = 0$, called the 'loading surface':

$$f = \frac{F}{(1+\kappa)^2} = \frac{3}{2M^2}\|\tilde{\mathbf{s}}\|^2 + \tilde{p}\,(\tilde{p} - p_l) = 0 \tag{3.6}$$

In (3.6), $\tilde{\mathbf{s}}$ and $\tilde{p}$ are the deviatoric and volumetric parts of $\tilde{\boldsymbol{\sigma}}$, defined as:

$$\tilde{\boldsymbol{\sigma}} = \boldsymbol{\sigma} - \boldsymbol{\alpha} \tag{3.7}$$

where

$$\boldsymbol{\alpha} = \boldsymbol{\sigma}_h \frac{\kappa}{1+\kappa} \tag{3.8}$$

and p_l is a hardening parameter, analogous to p_c, representing the size of the loading surface. It is defined as:

$$p_l = \frac{p_c}{1+\kappa} \tag{3.9}$$

Equation (3.6) defines another elliptical surface in the p–q plane, with $\boldsymbol{\alpha}$ representing the back stress. Because f has been defined by dividing F by $(1+\kappa)^2 > 1$, it is clear that the loading surface is completely inscribed by the bounding surface. Note also that M is unchanged in (3.6), so the axis ratios of the ellipses are the same. This is to be expected from the geotechnical interpretation of M as the slope of the critical state line, which is a property of the soil, and independent of loading history.

The loading surface, bounding surface and radial mapping rule used here are shown schematically in Figures 3.1(a) and (b). Fig. 3.1(a) shows the definition of hardening parameters p_c and p_l, while Fig. 3.1(b) demonstrates the relationship between $\boldsymbol{\sigma}_h$, $\boldsymbol{\sigma}$ and $\hat{\boldsymbol{\sigma}}$, through the radial mapping rule.

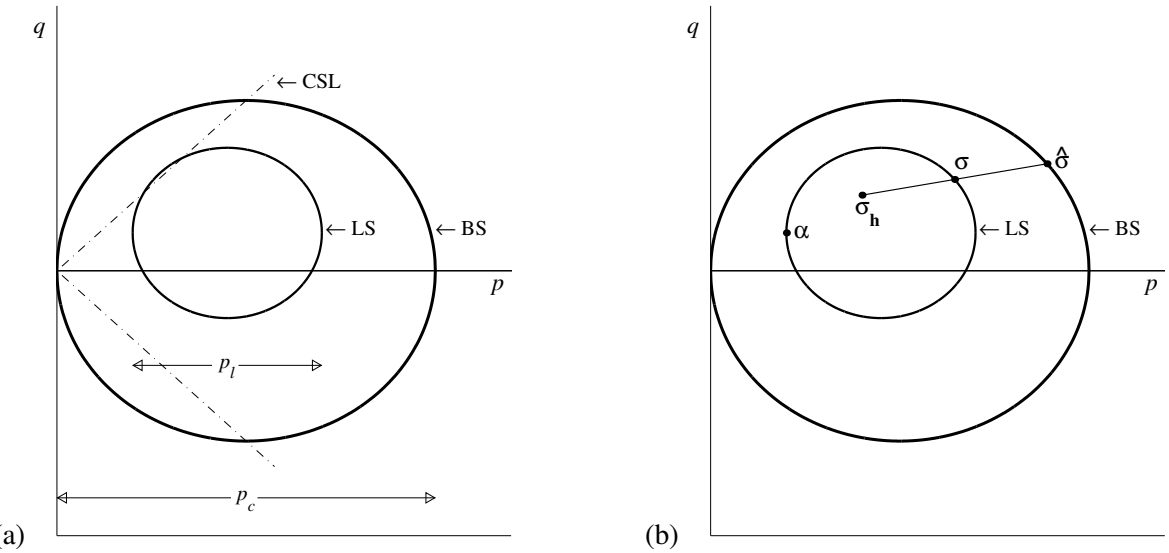

Figure 3.1: Loading surface (LS) and bounding surface (BS) in p–q plane, showing (a) definition of p_c and p_l, and (b) radial mapping of current stress point, $\boldsymbol{\sigma}$, onto a value on the bounding surface, $\hat{\boldsymbol{\sigma}}$

The loading surface gives a locus of all points with the same value of κ. The nature of its definition allows several results to be obtained, which simplify the application of a return map to the BS model [Borja *et al.*, 2001].

Result 1. *If* $F = \dot{F} = 0$*, then* $f = \dot{f} = 0$

Proof. From (3.6), $F = 0 \Rightarrow f = 0$. Differentiating gives:

$$\dot{F} = (1+\kappa)^2 \dot{f} + 2(1+\kappa)\dot{\kappa} f$$

And with $f = 0$, $\dot{F} = 0 \Rightarrow \dot{f} = 0$. This allows us to enforce the Kuhn-Tucker conditions, (2.12) on the loading surface instead of the bounding surface. □

Result 2. *The following relation holds:*

$$\frac{\partial f}{\partial \boldsymbol{\sigma}} = \frac{1}{1+\kappa}\frac{\partial F}{\partial \hat{\boldsymbol{\sigma}}} \tag{3.11}$$

Proof. Taking the right-hand side of (3.11), we differentiate (3.3) to obtain:

$$\begin{aligned}\frac{1}{1+\kappa}\frac{\partial F}{\partial \hat{\boldsymbol{\sigma}}} &= \frac{1}{1+\kappa}\left[\frac{1}{3}(2\hat{p} - p_c)\mathbf{1} + \frac{3}{M^2}\hat{\mathbf{s}}\right] \\ &= \frac{1}{3}\big(2p - \boldsymbol{\alpha}^p - p_l\big)\mathbf{1} + \frac{3}{M^2}\big(\boldsymbol{\sigma} - \boldsymbol{\alpha}^s\big) \\ &= \frac{1}{3}(2\tilde{p} - p_l)\mathbf{1} + \frac{3}{M^2}\tilde{\mathbf{s}} \quad = \quad \frac{\partial f}{\partial \boldsymbol{\sigma}}\end{aligned}$$

This shows the equivalence of an 'associative' flow rule, defined on the bounding surface with respect to the mapped stress, and one defined on the loading surface with respect to the current stress tensor. The two gradients are in the same direction, differing only by a constant factor. □

3.2.3 Flow rule

The bounding surface represents the asymptotic inelastic behaviour for the model, and it is sensible to define the associative flow rule with respect to the bounding surface and mapped stress. Result 2, however, allows us to formulate an equivalent flow rule on the loading surface with respect to the current stress; the development is identical to that of the MCC model:

$$\dot{\boldsymbol{\varepsilon}}^p = \dot{\gamma}\frac{\partial f(\tilde{\boldsymbol{\sigma}}, p_l)}{\partial \boldsymbol{\sigma}} = \dot{\gamma}\left[\frac{1}{3}(2\tilde{p} - p_l)\mathbf{1} + \frac{3}{M^2}\tilde{\mathbf{s}}\right] \tag{3.12}$$

As before, we decompose (3.12) into deviatoric and volumetric components:

$$\begin{aligned}\dot{\mathbf{e}}^p &= \dot{\gamma}\left(\frac{3}{M^2}\tilde{\mathbf{s}}\right) \\ \dot{\theta}^p &= \dot{\gamma}\,(2\tilde{p} - p_l)\end{aligned} \tag{3.13}$$

3.2.4 Hardening laws

The BS model has two stress-like hardening parameters, p_c and p_l, related through (3.9). For the hardening parameter defining the size of the bounding surface, p_c, the same evolutionary equation as in the MCC model will be considered. Expressed in rate form (1.15), for consistency with a subsequent expression for $\dot{p_l}$, we have:

$$\dot{p_c} = \frac{\dot{\theta^p}}{\lambda - k}\, p_c \tag{3.14}$$

The choice of a hardening law for p_l is the primary difference between different Cam-Clay bounding surface models proposed in the literature. Typically, an equation relating the plastic hardening modulus on the bounding surface to that on the loading surface is given. As a simple example, Zienkiewicz *et al.* [1985] proposed to express the plastic modulus at the current stress point, $\mathcal{H}$, as a function of the plastic modulus, $\hat{\mathcal{H}}$, at the projected stress point, as follows:

$$\mathcal{H} = \hat{\mathcal{H}}(1 + \kappa)^{\gamma} \tag{3.15}$$

where the exponent, γ, is a material parameter.

Eq. (3.15) predicts an infinite plastic modulus when the stress point is located at the homology centre, decreasing exponentially as the stress point approaches the bounding surface.

In contrast, Borja *et al.* [2001] use a direct evolutionary equation for the hardening parameter, p_l. Arguably, this is a more transparent formulation, and easier to convert to computer code. However, it is more difficult to determine the physical meaning of the extra model parameters. Nevertheless, an adaptation of the rate equation of Borja *et al.* [2001] has been used here:

$$\dot{p_l} = \frac{\dot{\theta^p}}{\lambda - k}\, (p_l + h\kappa^m) \tag{3.16}$$

where two new model parameters have been introduced, h and m.

3.2.5 Plastic moduli

For comparison with (3.15), and other similar models, an expression for the plastic modulus consistent with the hardening equations used here, (3.14) and (3.16), can be calculated.

The plastic modulus for the bounding surface is obtained as discussed in Chapter 2:

$$\hat{\mathcal{H}} = -\frac{1}{\dot{\gamma}} \frac{\partial F}{\partial p_c} \dot{p_c} = \frac{\hat{p} p_c (2\tilde{p} - p_l)}{\lambda - k} \tag{3.17}$$

Eq. (3.17) is given as a function of both the actual stress, $\boldsymbol{\sigma}$, and the mapped stress, $\hat{\boldsymbol{\sigma}}$. Making use of (3.4) and (3.9), Eq. (3.17) can be expressed only in terms of the current stress state, and parameter κ:

$$\hat{\mathcal{H}} = (1 + \kappa)^2 \frac{\tilde{p} p_l (2\tilde{p} - p_l)}{\lambda - k} \tag{3.18}$$

Similarly, the plastic modulus of the current stress point, based on the evolutionary equation for p_l, (3.16), can be determined:

$$\mathcal{H} = -\frac{1}{\dot{\gamma}}\frac{\partial f}{\partial p_l}\dot{p}_l = \frac{\tilde{p}(p_l + h\kappa^m)(2\tilde{p} - p_l)}{\lambda - k} \tag{3.19}$$

Substituting from (3.18), Eq. (3.19) can be expressed as:

$$\mathcal{H} = \hat{\mathcal{H}}\frac{(p_l + h\kappa^m)}{p_l(1+\kappa)^2} \tag{3.20}$$

Remark 3.1. It is important that the plastic modulus approaches the correct limits as $\kappa \to 0$ and $\kappa \to \infty$. In the former limit, corresponding to a stress point on the bounding surface, (3.20) gives $\mathcal{H} = \hat{\mathcal{H}}$, as required. The latter limit can be evaluated by rearranging (3.20):

$$\begin{aligned} \lim_{\kappa\to\infty} \mathcal{H} &= \lim_{\kappa\to\infty}\left[\frac{1}{(1+\kappa)^2} + \frac{h\kappa^m}{p_c(1+\kappa)}\right] \\ &= \infty \quad \text{for } h \neq 0\ ,\ m > 1 \end{aligned} \tag{3.21}$$

Therefore, we obtain the required instantaneously elastic response when $\kappa \to \infty$, and the stress point is located at the homology centre, provided the two conditions in (3.21) are satisfied.

3.2.6 Evolution of homology centre and back stress

In addition to the two isotropic hardening parameters, p_c and p_l discussed above, the model also makes use of a kinematic back stress-like hardening parameter, $\boldsymbol{\alpha}$. This parameter is defined explicitly by (3.8), and is a function of the homology centre, $\boldsymbol{\sigma}_h$.

In the model presented by Borja *et al.* [2001], the homology centre does not remain in a constant position during loading. As the bounding surface increases in size (p_c increases) the homology centre keeps the same relative position within the ellipse. Immediately upon unloading, the instantaneous response is elastic, and $\boldsymbol{\sigma}_h$ is relocated to the current value of $\boldsymbol{\sigma}$.

Following Borja *et al.* [2001], it will be useful to redefine $\boldsymbol{\sigma}_h$ based on the last position of unloading:

$$\boldsymbol{\sigma}_h = \boldsymbol{\Sigma} p_c \tag{3.22}$$

where $\boldsymbol{\Sigma}$ is defined as:

$$\boldsymbol{\Sigma} = \frac{\boldsymbol{\sigma}_h^*}{p_c^*} \tag{3.23}$$

and $\boldsymbol{\sigma}_h^*$ and p_c^* are the values of $\boldsymbol{\sigma}_h$ and p_c at which unloading was last detected. The condition:

$$\frac{\partial f}{\partial \boldsymbol{\sigma}} : \dot{\boldsymbol{\sigma}} < 0 \tag{3.24}$$

represents unloading in a time continuous setting, at which point, the current values of $\boldsymbol{\sigma}_h$ and p_c replace the old values of $\boldsymbol{\sigma}_h^*$ and p_c^*, respectively.

Eq. (3.22) can also be substituted into (3.8) to give the following expression:

$$\boldsymbol{\alpha} = \frac{\kappa}{1+\kappa}\boldsymbol{\Sigma} p_c = \kappa p_l \boldsymbol{\Sigma} \tag{3.25}$$

This gives a rate form for the back stress:

$$\dot{\boldsymbol{\alpha}} = \boldsymbol{\Sigma}(\kappa \dot{p}_l + \dot{\kappa} p_l) \tag{3.26}$$

which is not evaluated explicitly here.

Remark 3.2. A discrete relocation of the homology centre is used to model inelastic unloading in the model, such that an unloading state is replaced by loading with respect to a new origin. Model behaviour may also be considered 'anisotropic' in the sense that subsequent cycles 'load' with respect to a non-zero origin, and behaviour is therefore load direction-dependent.

Note, however, that a regular kinematic hardening model may also be considered anisotropic in this sense. In such a model, yielding of the material results in a continuous translation of the back stress tensor, and direction-dependence in subsequent loading cycles. However, in its usual formulation, a kinematic hardening model does not allow plasticity on unloading and reloading within the current yield surface, which is a useful feature of the current model.

The discontinuity in the evolution of the homology centre is a valuable concept in the modelling of regular cycles of loading. However, it can also lead to conceptual problems for certain load histories. The model as presented by Borja *et al.* [2001], and revisited here, is sensitive to small perturbations in the loading history, through round-off error in computations, or testing machine inaccuracies in experimental simulation. For example, a small reduction in load in an otherwise monotonic loading history will lead to relocation of the homology centre, and stiffening of subsequent response.

This drawback of the model will be further explored with some numerical simulations in Section 3.5.

Remark 3.3. Further problems may arise with the current model for cases of unloading. In particular, for cases where $(2\tilde{p} - p_l) < 0$, $(3.13)_2$ and (3.16) show that $\dot{\theta}^p$ and therefore $\dot{p}_l$ are negative. However, upon detection of the unloading condition, the homology centre is relocated, and p_l is instantaneously set to zero, which is incompatible with $\dot{p}_l = 0$. The computational aspects of this problem in a time discrete setting are further investigated in Section 3.5, where several loading histories which include stress reversals are modelled.

3.3 DISCRETE FORM OF MODEL

As with the MCC model, implicit backward Euler integration is used to determine time discrete versions of the model equations. These expressions are similar to those obtained in Section 2.3, with extra terms introduced for the back stress parameter, $\boldsymbol{\alpha}$.

Implicit integration of (3.13) yields:

$$\begin{aligned} \mathbf{e}^p &= \mathbf{e}^p_n + \Delta\gamma \frac{3}{M^2}\tilde{\mathbf{s}} \\ \theta^p &= \theta^p_n + \Delta\gamma(2\tilde{p} - p_l) \end{aligned} \tag{3.27}$$

with

$$\Delta\gamma = \int_{t_n}^{t_{n+1}} \dot{\gamma}\mathrm{d}t$$

Substituting (3.27) into (3.1) gives:

$$p = p_0 \exp\left(\frac{\theta - \theta^p_n - \Delta\gamma(2\tilde{p} - p_l)}{k}\right)\left[1 + \frac{\alpha}{k}\|\mathbf{e} - \mathbf{e}^p_n - \Delta\gamma\frac{3}{M^2}\tilde{\mathbf{s}}\|^2\right] \tag{3.28}$$

Similarly, substituting (3.27) into (3.2), and collecting $\mathbf{s}$ terms results in:

$$\mathbf{s} = \frac{2\alpha p_0 \exp\left(\frac{\theta-\theta^p_n}{k}\right)\exp\left(\frac{-\Delta\gamma(2\tilde{p}-p_l)}{k}\right)}{1 + \frac{6\alpha p_0}{M^2}\Delta\gamma\exp\left(\frac{\theta-\theta^p_n}{k}\right)\exp\left(\frac{-\Delta\gamma(2\tilde{p}-p_l)}{k}\right)}\left[\mathbf{e} - \mathbf{e}^p_n + \Delta\gamma\frac{3}{M^2}\boldsymbol{\alpha}^s\right] \tag{3.29}$$

Unlike the MCC model, we now have the hardening equations, (3.14) and (3.16), in rate form. The former can be integrated explicitly (as in Chapter 2) while the latter can only be integrated implicitly. Here, implicit integration will be used for both hardening equations, for numerical consistency. Therefore, using backward Euler integration on (3.14) and (3.16), then substituting for $\Delta\theta^p$ from $(3.27)_1$ leads to the discrete forms:

$$p_c = \frac{p_{cn}}{1 - \frac{1}{\lambda-k}\Delta\gamma(2\tilde{p} - p_l)} \tag{3.30}$$

$$p_l = \frac{p_{ln} + \frac{1}{\lambda-k}h\kappa^m\Delta\gamma(2\tilde{p} - p_l)}{1 - \frac{1}{\lambda-k}\Delta\gamma(2\tilde{p} - p_l)} \tag{3.31}$$

3.4 RETURN MAP ALGORITHM

There have been difficulties in the past in applying a return mapping algorithm to the BS model. The consistency condition is defined on the bounding surface, but it is difficult to apply the return map to the mapped stress tensor. In this formulation, however, Result 1 from Section 3.2.2 allows the consistency condition to be applied directly to the loading function, f, in terms of the current stress tensor.

In fact, the loading function has many properties of a yield function. The principal difference between the two is that the former is always equal to zero, while a yield function can be less than or equal to zero. The loading surface moves with the stress point, even upon unloading, while a yield surface represents the maximum extent of previous yielding.

In the BS formulation, instantaneous elastic response only occurs instantaneously upon detection of the unloading condition, and inelastic behaviour occurs at all other times. In a time discrete setting, the usual

condition for an elastic time step, $f^{tr} < 0$, now results in a discrete relocation of the homology centre, with plastic response now occurring with respect to the new loading function.

As discussed above, this can lead to some convergence difficulties immediately upon unloading. We will allow an elastic time step when $p_l < p_l^{en}$, the elastic nucleus condition given in Section 3.2.6. However, this will require calculation of an appropriate value of p_l consistent with $\boldsymbol{\varepsilon}$, $\boldsymbol{\sigma}^{tr}$ and p_c. Details of this calculation are given in Section 3.4.2, below.

Otherwise, the return mapping follows exactly the same procedure as in Chapter 2. A trial state is calculated by freezing plastic flow. A condition for an elastic time step is checked, in this case representing the elastic nucleus. If satisfied, an elastic tangent tensor is evaluated; otherwise a plastic correction is made, and an inelastic tangent consistent with the discretisation is determined.

3.4.1 Trial state

As before, we set the trial discrete consistency parameter equal to zero; from (3.13), (3.28), (3.29), (3.30) and (3.31), we obtain the following trial values:

$$\begin{cases} \Delta\gamma^{tr} = 0 \\ \mathbf{e}^{e,tr} = \mathbf{e} - \mathbf{e}_n^p \\ \theta^{e,tr} = \theta - \theta_n^p \\ p^{tr} = p_0 \exp\left(\dfrac{\theta^{e,tr}}{k}\right)\left(1 + \dfrac{\alpha}{k}\|\mathbf{e}^{e,tr}\|^2\right) \\ \mathbf{s}^{tr} = 2\alpha p_0 \exp\left(\dfrac{\theta^{e,tr}}{k}\right)\mathbf{e}^{e,tr} \\ p_c^{tr} = p_{cn} \\ p_l^{tr} = p_{ln} \end{cases} \tag{3.32}$$

Furthermore, κ^{tr} can be obtained from (3.9):

$$\kappa^{tr} = \frac{p_c^{tr}}{p_l^{tr}} - 1 = \kappa_n \tag{3.33}$$

3.4.2 Check unloading condition

In a time discrete setting, the unloading condition is replaced by a trial loading function, as in classical plasticity. Making use of (3.6), we define:

$$f^{tr} = \frac{3}{2M^2}\|\tilde{\mathbf{s}}^{tr}\|^2 + \tilde{p}^{tr}(\tilde{p}^{tr} - p_l) < 0 \tag{3.34}$$

This condition may not be sufficient for convergence of plastic time steps soon after unloading is detected. In this case, κ is large, while $(2\tilde{p} - p_l)$ is small, and (3.31) may be ill-conditioned for solution. Borja *et al.* [2001] suggest the use of a small elastic nucleus for low values of p_l. We allow elastic behaviour for $p_l < p_l^{en}$, where p_l^{en} is a size parameter for the nucleus.

The choice of p_l^{en} is a tradeoff between stability and accuracy. For high values of p_l^{en}, the problem of ill-conditioning does not occur, but significant plastic strain development is ignored. A small elastic nucleus is desirable for accuracy of solution, but convergence problems may be experienced. Parametric studies by Borja *et al.* [2001] suggest a value of $0.10\, p_c$ is appropriate.

If the unloading condition (3.34) is satisfied, then the homology centre is relocated to the stress state at time t_n, and the time step may be considered 'loading' relative to a new centre of projection. This requires six further internal variables to store the stress state at time t_n. Alternatively, the normalised projection state, $\boldsymbol{\Sigma}_n = \boldsymbol{\sigma}/p_c$ may be stored, and on detection of unloading:

$$\boldsymbol{\Sigma} = \frac{\boldsymbol{\sigma}}{p_c} = \boldsymbol{\Sigma}_n \tag{3.35}$$

To be consistent with (3.35), the value of p_l at the start of the time step must also be set to zero if the unloading condition is satisfied. That is:

$$p_{ln} = 0 \tag{3.36}$$

In a time continuous setting, p_l will instantaneously assume a value of zero, and κ will tend to an infinite value. However, in a time discrete setting, this will only present a problem if the stress state remains at the homology centre for the duration of the time step, $\Delta t = t_{n+1} - t_n$. However, this would lead to $f^{tr} = 0$, which does not satisfy the unloading condition, so no singularities should occur.

Given the new trial values for p_{ln} and $\boldsymbol{\Sigma}$, the relative stress tensor, $\tilde{\boldsymbol{\sigma}}^{tr}$, is reevaluated from (3.7) and (3.32).

3.4.3 Check elastic nucleus

For time steps immediately following unloading, values of $\tilde{\boldsymbol{\sigma}}$ and p_l are expected to be small, while κ is large. From (3.27), plastic strain increments are small, and do not contribute a large amount to the total strain.

As discussed previously, an elastic nucleus can be assumed for small values of p_l. However, p_{ln} can no longer be used for the trial value of p_l. If the trial values of p_l and κ were used as given by (3.32) and (3.33), then a stress point would never leave the elastic nucleus, as p_l^{tr} would remain equal to p_{ln}, and thus never exceed p_l^{en}.

We obtain the appropriate trial value of p_l by requiring the trial stress state and current homology centre to satisfy the bounding surface equation, (3.3). The radial mapping equation for $\hat{\boldsymbol{\sigma}}$, (3.4), is substituted into the expression for the bounding surface, (3.3), giving the following expression:

$$F = \frac{3}{M^2}\left\|(1+\kappa)\mathbf{s}^{tr} - \kappa\boldsymbol{\sigma}_h^{s,tr}\right\|^2 + \left[(1+\kappa)p^{tr} - \kappa\sigma_0^{p,tr}\right]\left[(1+\kappa)p^{tr} - \kappa\sigma_0^{p,tr} - p_c^{tr}\right] = 0 \quad (3.37)$$

which is a function of the trial stress state, hardening parameter p_c, and the trial homology centre. The latter is defined in terms of the normalised homology centre:

$$\boldsymbol{\sigma}_h^{tr} = \boldsymbol{\Sigma} p_c^{tr} \quad (3.38)$$

Eq. (3.37) can therefore be solved for κ:

$$\kappa = \frac{-b + \sqrt{b^2 - 4ac}}{2a} \quad (3.39)$$

where

$$a = \frac{3}{2M^2}\|\mathbf{s}^{tr} - \boldsymbol{\sigma}_h^{s,tr}\|^2 + (p^{tr} - \sigma_0^{p,tr})^2$$
$$b = \frac{3}{M^2}\,\mathbf{s}^{tr}{:}\left(\mathbf{s}^{tr} - \boldsymbol{\sigma}_h^{s,tr}\right) + \left(p^{tr} - \sigma_0^{p,tr}\right)\left(2p^{tr} - p_c^{tr}\right)$$
$$c = \frac{3}{2M^2}\|\mathbf{s}^{tr}\|^2 + p^{tr}\left(p^{tr} - p_c^{tr}\right)$$

Finally, the value of κ calculated in (3.39) is used to calculate a new trial value for p_l, using p_c^{tr} and (3.9). This value of p_l^{tr} is compared with the elastic nucleus condition:

$$p_l^{tr} < p_l^{en} \quad (3.40)$$

If this condition is satisfied, the time step is elastic, and the plastic correction stage is omitted. If p_l lies outside the elastic nucleus, then a Newton algorithm must again be used to determine the plastically-corrected state.

Remark 3.4. Using the above calculation to determine a trial elastic value of p_l is inconsistent with the hardening equation, (3.31). The other trial values defined in (3.32) correspond to the case where $\Delta\gamma = 0$, whereas substituting $\Delta\gamma = 0$ into (3.31) gives $p_l^{tr} = p_n$, as in $(3.32)_7$.

However, as stressed by Borja *et al.* [2001], the elastic nucleus is merely intended as a computational tool, and the size of the nucleus, governed by the constant ratio p_l^{en}/p_c, should be determined such that the error resulting from the above inconsistency is minimised.

3.4.4 Plastic Correction

The same procedure as in Chapter 2 is used here. The back stress has been expressed above in terms of a normalised homology centre, $\boldsymbol{\Sigma}$, which remains constant during a loading cycle. Therefore, the inclusion of this kinematic hardening term does not add extra independent variables to the Newton algorithm.

The addition of an extra isotropic hardening parameter p_l adds one extra degree of freedom, for a total of four unknowns in the plastic correction step. This represents a significant computational improvement over the solution algorithm of Borja *et al.* [2001], which uses the same procedure with eight unknowns. However, the complexity of the residual gradient calculation is increased accordingly, and is presented in Appendix C.

As before, the appropriate plastic correction for each variable is found by substituting the trial state values, (3.32), into (3.27), (3.28) and (3.29):

$$\begin{cases} \mathbf{e}^p = \mathbf{e}^{p,tr} + \dfrac{3\Delta\gamma}{M^2}\tilde{\mathbf{s}} \\ \theta^p = \theta^{p,tr} + \Delta\gamma(2\tilde{p} - p_l) \\ \mathbf{s} = \exp\left(\dfrac{-\Delta\gamma}{k}(2\tilde{p} - p_l)\right)\left(\mathbf{s}^{tr} + 2\alpha p_0 \exp\left(\dfrac{\theta - \theta^p}{k}\right)\dfrac{3\Delta\gamma}{M^2}\boldsymbol{\alpha}^s\right) \\ \quad \left[1 + \dfrac{6\alpha p_0}{M^2}\Delta\gamma \exp\left(\dfrac{\theta - \theta_n^p}{k}\right)\exp\left(\dfrac{-\Delta\gamma}{k}(2\tilde{p} - p_l)\right)\right]^{-1} \\ p = p_0 \exp\left(\dfrac{\theta^{e,tr}}{k}\right)\exp\left(\dfrac{-\Delta\gamma}{k}(2\tilde{p} - p_l)\right) \\ \quad \left[1 + \dfrac{\alpha}{k}\left(\|\mathbf{e}^{e,tr}\|^2 - \dfrac{6}{M^2}\Delta\gamma\tilde{\mathbf{s}} : \mathbf{e}^{e,tr} + \dfrac{9}{M^4}\Delta\gamma^2\|\tilde{\mathbf{s}}\|^2\right)\right] \end{cases}$$

The hardening parameters may be obtained directly from (3.30) and (3.31).

These equations are simplified by introducing constants analogous to those used in Chapter 2, with the addition of one further constant for the new hardening equations:

$$\begin{cases} A_1 = \exp\left(\dfrac{-\Delta\gamma}{k}(2\tilde{p} - p_l)\right) \\ A_2 = \exp\left(\dfrac{\theta^{e,tr}}{k}\right) \\ A_3 = \dfrac{6\alpha p_0}{M^2}A_2 \\ A_4 = 1 + \Delta\gamma A_1 A_3 \\ A_5 = \dfrac{A_1}{A_4} \\ A_6 = \left\{1 + \dfrac{\alpha}{k}\left(\|\mathbf{e}^{e,tr}\|^2 - \dfrac{6}{M^2}\Delta\gamma\tilde{\mathbf{s}} : \mathbf{e}^{e,tr} + \dfrac{9}{M^4}\Delta\gamma^2\|\tilde{\mathbf{s}}\|^2\right)\right\} \\ A_7 = \dfrac{1}{\lambda - k}\Delta\gamma(2\tilde{p} - p_l) \end{cases} \tag{3.42}$$

Equations $(3.41)_3$, $(3.41)_4$, (3.30) and (3.31) then simplify to:

$$\mathbf{s} = A_5 \left(\mathbf{s}^{tr} + A_3 \Delta\gamma \boldsymbol{\alpha}^s \right) \tag{3.43}$$

$$p = p_0 A_1 A_2 A_6 \tag{3.44}$$

$$p_c = \frac{p_{cn}}{1 - A_7} \tag{3.45}$$

$$p_l = \frac{p_{ln} + A_7 h \kappa^m}{1 - A_7} \tag{3.46}$$

Combining (3.7) and (3.43) leads to a useful expression for $\tilde{\mathbf{s}}$:

$$\tilde{\mathbf{s}} = \mathbf{s} - \boldsymbol{\alpha}^s = A_5 \mathbf{s}^{tr} - \frac{1}{A_4} \boldsymbol{\alpha}^s \tag{3.47}$$

We solve these equations using the same procedure as in Chapter 2, with one additional unknown — the extra hardening parameter, p_l. Equations (3.6), (3.9), (3.44) and (3.46) are solved, substituting for $\mathbf{s}$, $\tilde{\mathbf{s}}$ and p_c from (3.43), (3.47) and (3.45), respectively.

We introduce the vector of unknowns, $\boldsymbol{x} = \{\tilde{p},\ p_l,\ \Delta\gamma,\ \kappa\}$, and vector of residuals:

$$\mathbf{g}(\boldsymbol{x}) = \begin{Bmatrix} g_1 \\ g_2 \\ g_3 \\ g_4 \end{Bmatrix} = \begin{Bmatrix} \frac{3\|\tilde{\mathbf{s}}\|^2}{2M^2} + \tilde{p}(\tilde{p} - p_l) \\ p_0 A_1 A_2 A_6 - \tilde{p} - \alpha^p \\ (p_{ln} + A_7 h \kappa^m) \left[1 - A_7\right]^{-1} - p_l \\ (1 + \kappa) p_l - p_{cn} \left[1 - A_7\right]^{-1} \end{Bmatrix} \tag{3.48}$$

As before, we use a Newton algorithm, such that the value from the $(k+1)^{\text{th}}$ iteration is found from:

$$\boldsymbol{x}^{(k+1)} = \boldsymbol{x}^{(k)} - \left[\frac{\partial \mathbf{g}}{\partial \boldsymbol{x}} \right]^{-1} \mathbf{g}\left(\boldsymbol{x}^{(k)} \right) \tag{3.49}$$

Convergence can be considered achieved when the normalised vector of residuals is less than machine tolerance:

$$\|\mathbf{g}\|^* = \sqrt{\left(\frac{g_1}{p_0^2}\right)^2 + \left(\frac{g_2}{p_0}\right)^2 + \left(\frac{g_3}{p_{l0}}\right)^2 + \left(\frac{g_4}{p_{l0}}\right)^2} < TOL \tag{3.50}$$

Calculation of the residual gradient for use in (3.49) is presented in Appendix C.

Remark 3.5. The problem dimension could be further reduced by solving g_4 for κ, and substituting this expression into α^p, g_2 and g_3. This would reduce the number of unknowns to three, equivalent to the MCC model of Chapter 2, and to the GP model presented in the next chapter. However, this has not been attempted here.

3.4.5 Consistent tangent

Elastic step

Comparing the trial states for the MCC and BS models, (2.16) and (3.32), it is evident that the elastic tangent tensor will be the same as in Chapter 2:

$$\mathbb{C}^e = \frac{p_0}{k}\exp\left(\frac{\theta^e}{k}\right)\left[2\alpha k\mathbb{I}_{\text{dev}} + 3\left(1+\frac{\alpha}{k}\|\mathbf{e}^e\|^2\right)\mathbb{I}_{\text{vol}} + 2\alpha\left(\mathbf{1}\otimes\mathbf{e}^e + \mathbf{e}^e\otimes\mathbf{1}\right)\right] \tag{3.51}$$

Plastic step

As in Chapter 2, we obtain the inelastic tangent tensor by differentiating stress and hardening variables with respect to the trial elastic strain, $\boldsymbol{\varepsilon}^{e,tr}$, then enforcing the consistency condition to find $\partial\Delta\gamma/\partial\boldsymbol{\varepsilon}^{e,tr}$. The complete calculation is given in Appendix D, where the following expression is obtained:

$$\begin{aligned}\mathbb{C}^{\text{p}} = &\left(H_1\mathbf{1} + G_3\mathbf{s} + H_4\boldsymbol{\Sigma}_{\text{dev}}\right)\otimes\mathbf{1} + \left(H_2\mathbf{1} + G_5\mathbf{s} + H_5\boldsymbol{\Sigma}_{\text{dev}}\right)\otimes\mathbf{s}\\ &+ \left(H_3\mathbf{1} + G_7\mathbf{s} + H_6\boldsymbol{\Sigma}_{\text{dev}}\right)\otimes\boldsymbol{\Sigma}_{\text{dev}} + C_{13}\mathbb{I}_{\text{dev}}\end{aligned} \tag{3.52}$$

where the values of G_3, G_5, G_7 and H_1–H_7 are obtained in Appendix D.

Remark 3.6. The procedure used in Appendix D results in an expression for $\mathbb{C}^{\text{p}}$ in closed-form. The calculation requires no matrix inversion, which results in an efficient procedure, computationally. Contrast the solution algorithm of Borja *et al.* [2001], which requires the inversion of a 4×4 and a 6×6 matrix.

3.4.6 Converting to 'mechanical' sign convention

For tension-positive sign convention, the tangent tensor must be converted in the same manner as Chapter 2. Eq. (2.35) remains valid here, from which we obtain:

$$\begin{aligned}\mathbb{C}^{\text{p}} = &\left(H_1\mathbf{1} - G_3\mathbf{s} - H_4\boldsymbol{\Sigma}_{\text{dev}}\right)\otimes\mathbf{1} + \left(-H_2\mathbf{1} + G_5\mathbf{s} + H_5\boldsymbol{\Sigma}_{\text{dev}}\right)\otimes\mathbf{s}\\ &+ \left(-H_3\mathbf{1} + G_7\mathbf{s} + H_6\boldsymbol{\Sigma}_{\text{dev}}\right)\otimes\boldsymbol{\Sigma}_{\text{dev}} + C_{13}\mathbb{I}_{\text{dev}}\end{aligned} \tag{3.53}$$

for the inelastic time step, where the constant terms are the same as for the compression-positive case. The elastic tangent is as given in (2.36).

3.5 NUMERICAL TESTS

The numerical tests of Section 3.5 are repeated here for the BS models, with material parameters indicated in Table 3.1. As before, p_0 is defined separately for each test, based on the non-zero initial value of

pressure defined by the loading history. In addition, p_{l0} is defined equal to p_0 for each test, which follows from the definition of the loading surface (3.6), and an initial deviatoric stress, $\mathbf{s}_0 = \mathbf{0}$. Finally, we take $p_l^{en} = 0.10\, p_c$, as suggested in Section 3.3.

Table 3.1: Bounding Surface model parameters

Parameter	α	M	λ	k	p_{c0}	h	m	$\boldsymbol{\sigma}_h$
Value	100	0.9	0.09	0.02	100 kPa	5000 kPa	2	$\mathbf{0}$

In the following figures, the initial and final position of the loading surface are indicated by f_0 and f_1, and the initial and final positions of the bounding surface are indicated by F_0 and F_1.

3.5.1 Isotropic compression test

Initially, the isotropic compression test from Section 2.5.1 was attempted with the current model. However, as predicted in Remark 3.3, the unloading portion of the loading history resulted in some difficulties, both conceptual and computational. On initial unloading, the homology centre and loading surface are relocated, and elastic behaviour continues until the boundary of the elastic nucleus is reached. When p_l^{tr} exceeds p_l, inelastic behaviour is expected, and the plastic correction described in Section 3.4.4 is carried out. However, given that $p_l > 0$, $\Delta\gamma > 0$, and that for the isotropic loading history described here, $\tilde{p} = 0$, Eq. (3.31) gives $p_l < p_{ln}$. This implies that the loading surface decreases in size, a result that is inconsistent with the loading history described, in which p decreases and the loading surface must grow accordingly.

The results of the simulation are shown in Fig. 3.2, for 1000 time steps. Convergence problems did not develop immediately upon unloading as could have been expected from the above discussion, and a significant amount of unloading continued until a level of mean stress, $p \approx 100$ kPa, was reached. However, for the entire inelastic loading branch of Fig. 3.2(b), the discrete consistency parameter, $\Delta\gamma$, converged to a value less than zero, a result which violates the Kuhn-Tucker condition, Eq. $(2.12)_1$. Therefore, the unloading portion of Figure 3.2 should not be considered as an appropriate representation of the behaviour of the model, and under general loading conditions involving stress reversals, the adequacy of the model is questionable.

In order to investigate the reloading behaviour of the model, the original loading history was modified, by limiting the unloading portion to a value of $p = 150$ kPa. The results of this simulation are shown in Fig. 3.3, for 1000, 100 and 48 time steps — due to the unloading difficulties discussed above, fewer time steps led to convergence problems in the unloading portion of the loading history.

The initial loading branch of Fig. 3.3(b) is identical to the results obtained for the MCC model, as for $p_{c0} = p_{l0}$, and $\boldsymbol{\sigma}_h = \mathbf{0}$, the models are identical. On detection of the unloading condition, $\boldsymbol{\sigma}_h$ is

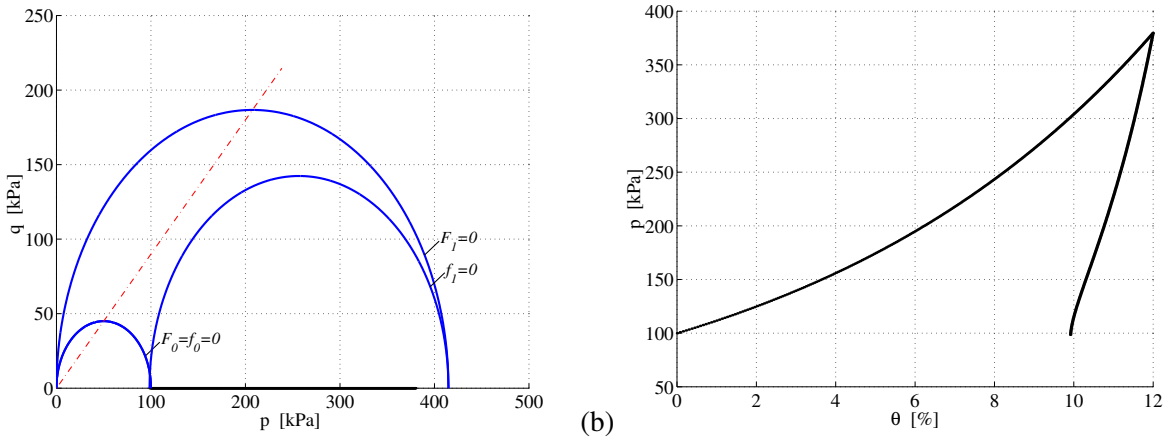

(a) (b)

Figure 3.2: Isotropic compression test with loading history from Section 2.5.1. (a) Stress path on p–q diagram and (b) volumetric stress, p, vs. volumetric strain, θ.

relocated, and subsequent unloading and reloading behaviour is different to the MCC model. If we ignore the unloading branch of Fig. 3.3(b), for the reasons discussed in Section 3.5.1, we see that inelastic behaviour commences immediately on stress reversal. The concave downward behaviour of the model for $p_c > p_l$, evident in Fig. 3.3(b), is cited by Borja *et al.* [2001] as an improvement of the BS model over the MCC model in the description of the behaviour of real overconsolidated clays.

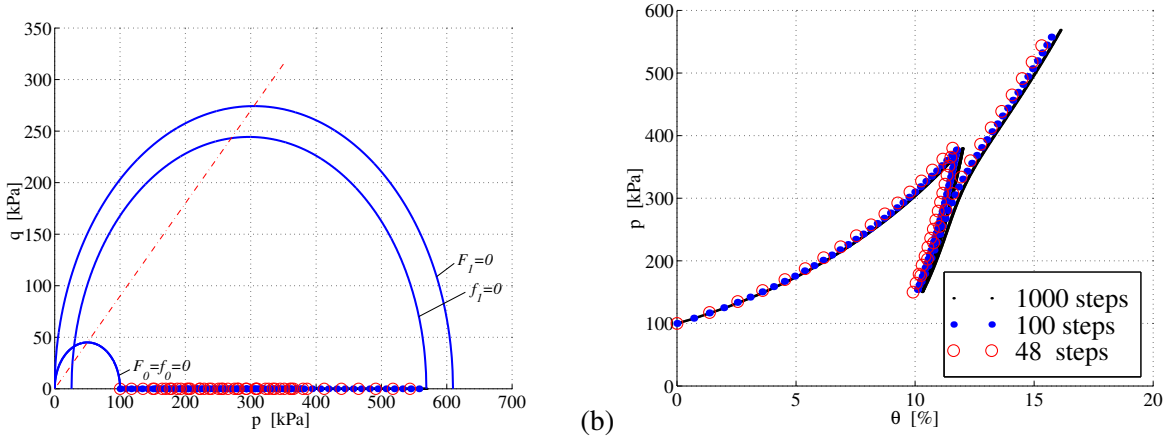

(a) (b)

Figure 3.3: Isotropic compression test with modified loading history. (a) Stress path on p–q diagram and (b) volumetric stress, p, vs. volumetric strain, θ.

The convergence of the model is analysed in Fig. 3.4, for the 100-time step and 48-time step simulations. Convergence to the required tolerance is obtained within five iterations in each case, and at an asymptotically quadratic rate (Fig. 3.4(b)).

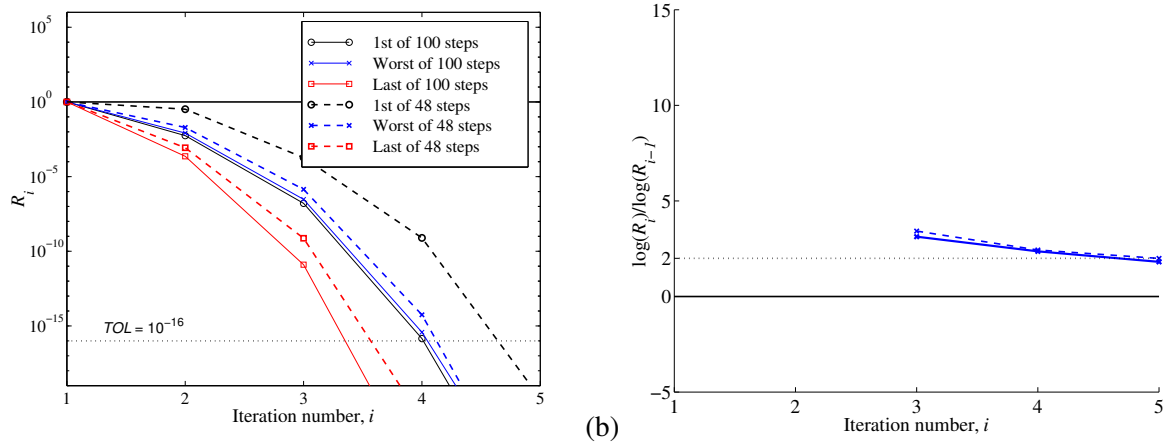

Figure 3.4: Isotropic compression test. Convergence profiles of (a) normalised residual, R_i, and (b) ratio of successive logarithms, $\log R_i$.

3.5.2 Monotonic isotropic compression with small perturbation in loading history

Although the discrete relocation of the homology centre leads to realistic reloading behaviour for the previous loading history, Remark 3.2 suggested that this may not be the case in general. In particular, a small perturbation in the loading history has as much effect on the relocation of the homology centre as the complete unloading path described in the previous simulation.

The effect of such a perturbation was analysed in a further isotropic compression simulation. The loading history is the same as described above, but with the unloading portion reduced in size to $\Delta p = -5$ kPa. This increment lies within the elastic nucleus, so the unloading problems discussed above do not arise, although the unloading condition is met, and the homology centre is relocated.

Initially, the material parameters in Table 3.1 were used. However, some convergence problems were experienced on reloading, when the stress point was too close to the bounding surface. In particular, when the trial stress value lay outside the bounding surface, the analysis failed to converge. It is not immediately clear if this is a problem which also applies to the solution algorithm proposed by Borja *et al.* [2001].

To remove this problem, a value of $p_{c0} = 200$ kPa was used, along with $p_0 = p_{l0} = 100$ kPa, as before. In addition, two different values of h were considered: 5000 kPa as in Table 3.1, and 50 kPa.

The results from this simulation are presented in Fig. 3.5. For $h = 5000$ kPa, used throughout this section, the effect of the relocation of the homology centre does not significantly alter the subsequent stress–strain behaviour. However for the lower h value, the effect is much more significant, and leads to a sharp discontinuity in the otherwise monotonic p–θ response shown in Fig. 3.5.

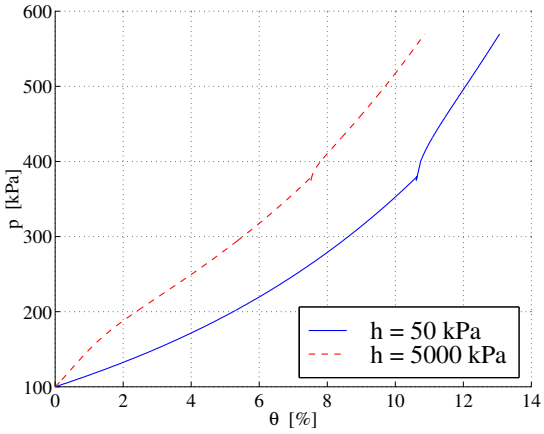

Figure 3.5: Monotonic isotropic compression with small perturbation in loading history. Volumetric stress, p, vs. volumetric strain, θ.

3.5.3 Triaxial compression of lightly overconsolidated sample

The triaxial test described in Section 2.5.2 was repeated for the current model, with results for 1000, 100 and 24 time steps summarised in Fig. 3.6. The results obtained here are nearly identical to those obtained for the MCC model (Fig. 2.3). This could be expected for monotonic loading of lightly overconsolidated soils, for which the loading surface lies close to the bounding surface.

The convergence of the model is assessed in Fig. 3.7, in the same manner as previously. Convergence is achieved within five and seven iterations for the 100-time step and 24-time step analyses, respectively, and at an asymptotically quadratic rate.

3.5.4 Triaxial compression of heavily overconsolidated sample

Results for the triaxial compression test of a heavily consolidated sample are presented in Fig. 3.8, for 1000, 100 and 18 time steps. The BS model is unable to describe the softening response obtained in Chapter 2, and converges to a critical state through purely dilative behaviour. Although $p < p_c/2$, as in the MCC simulation, here we have $\tilde{p} > p_l/2$, and the associative flow rule defined in (3.12) gives $\dot{\theta^p} > 0$. Compaction behaviour ($\dot{\theta^p} < 0$) will require $\tilde{p} < p_l/2$, a condition that has been shown to lead to problems for the isotropic compression test.

The inability to model compaction and softening response of heavily consolidated soils could be considered a shortcoming of the present model. However, as stated in Chapter 2, the MCC yield condition used as the basis of all the models presented in this work is intended for normally consolidated and lightly consolidated clays only. The results presented here, although significantly different to those obtained for the MCC model, are used to test the robustness of the solution algorithm for general load cases and initial

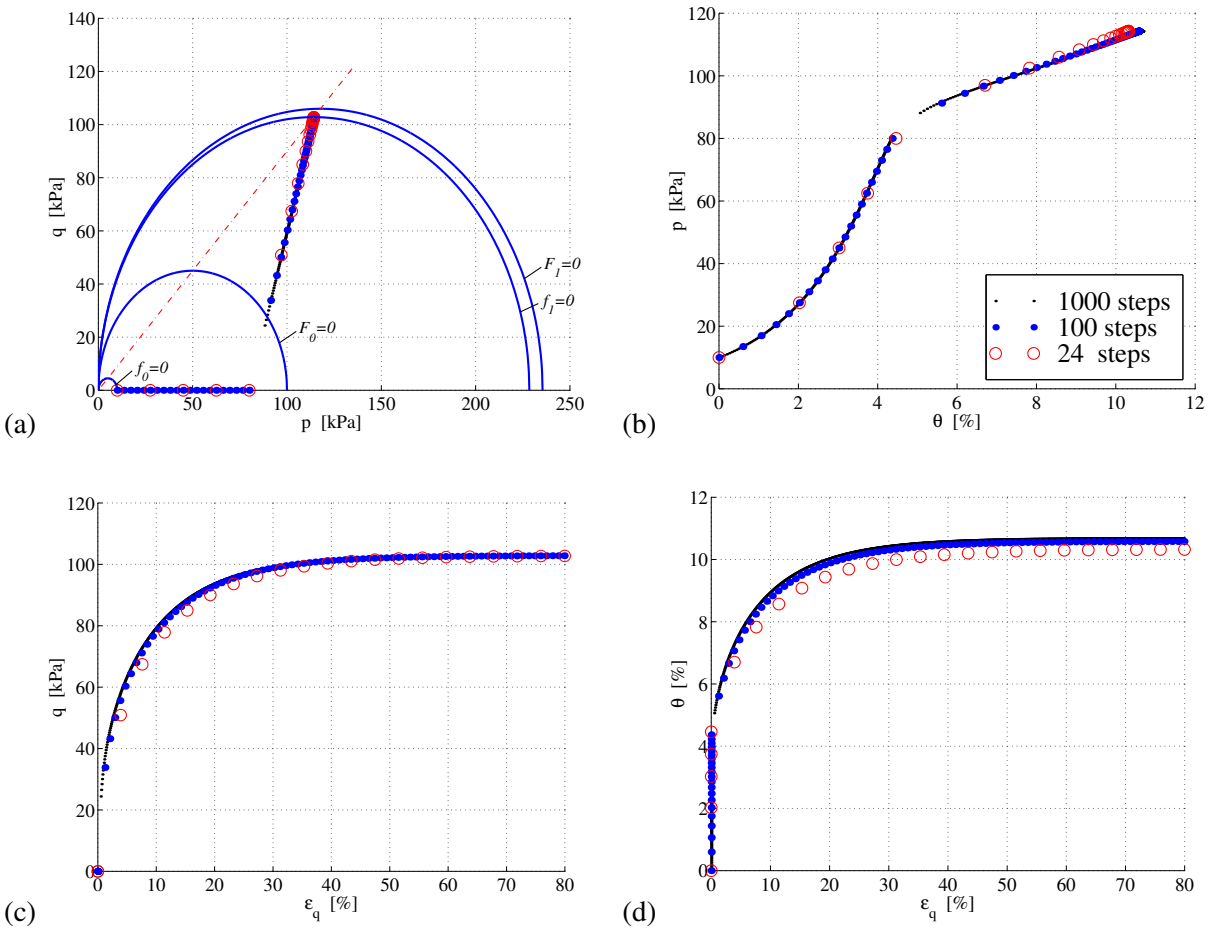

Figure 3.6: Triaxial compression of lightly overconsolidated sample. (a) Stress path on p–q diagram, (b) volumetric stress, p, vs. volumetric strain, θ, (c) deviatoric stress, q, vs. deviatoric strain, ε_q, and (d) θ vs. ε_q.

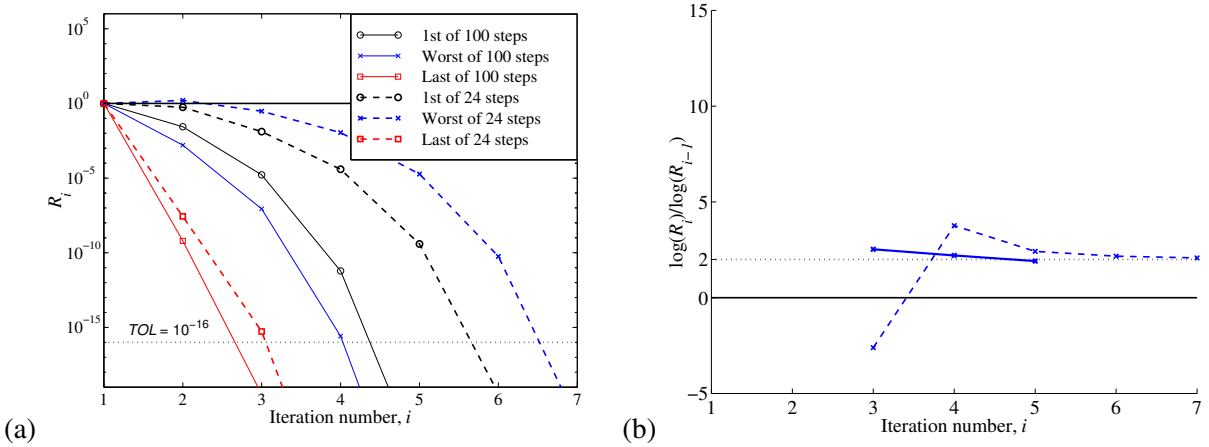

Figure 3.7: Triaxial compression of lightly overconsolidated sample. Convergence profiles of (a) normalised residual, R_i, and (b) ratio of successive logarithms, $\log R_i$.

conditions. As shown in Fig. 3.9, convergence is again obtained quadratically in these analyses.

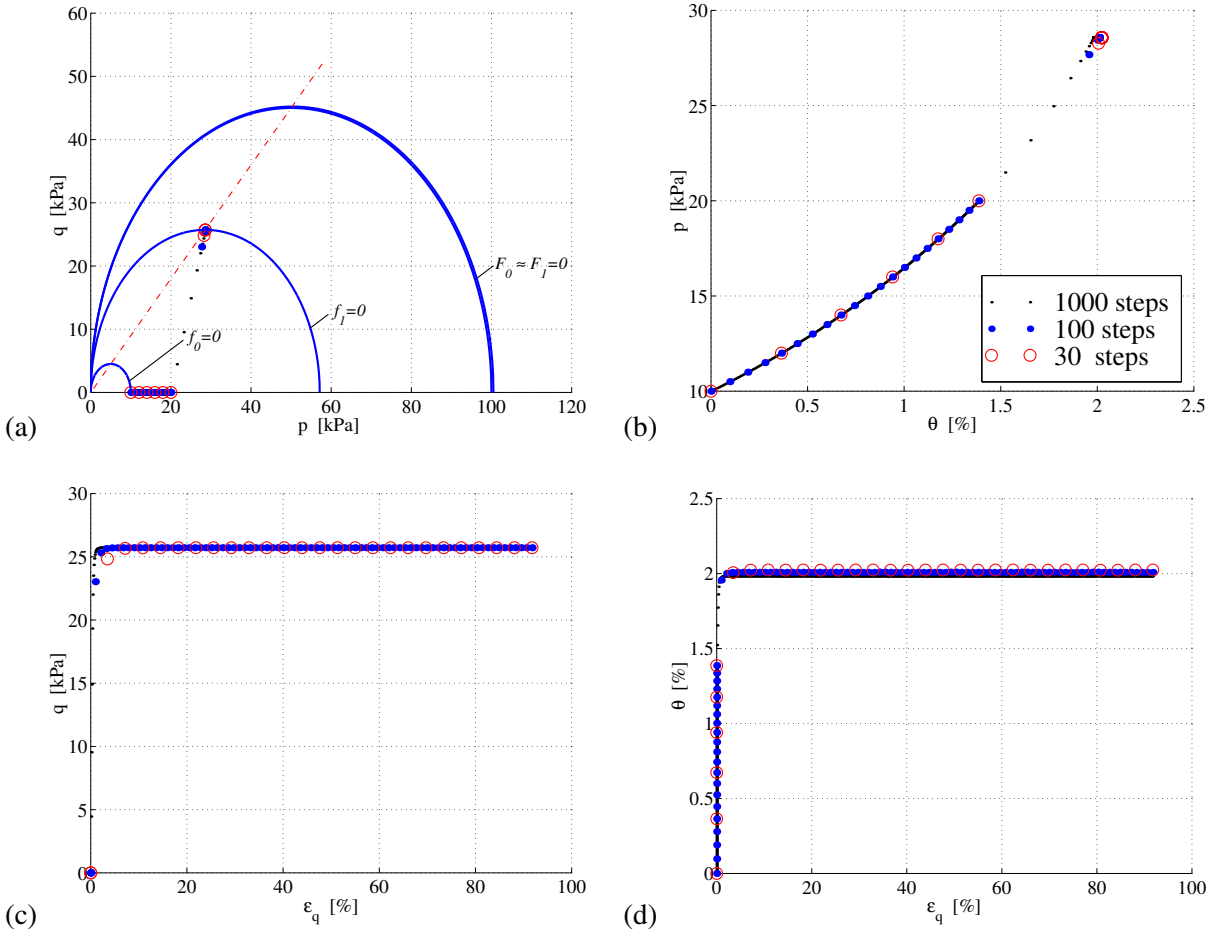

Figure 3.8: Triaxial compression of heavily overconsolidated sample. (a) Stress path on p–q diagram, (b) volumetric stress, p vs. volumetric strain, θ, (c) deviatoric stress, q vs. deviatoric strain, ε_q, and (d) θ vs. ε_q.

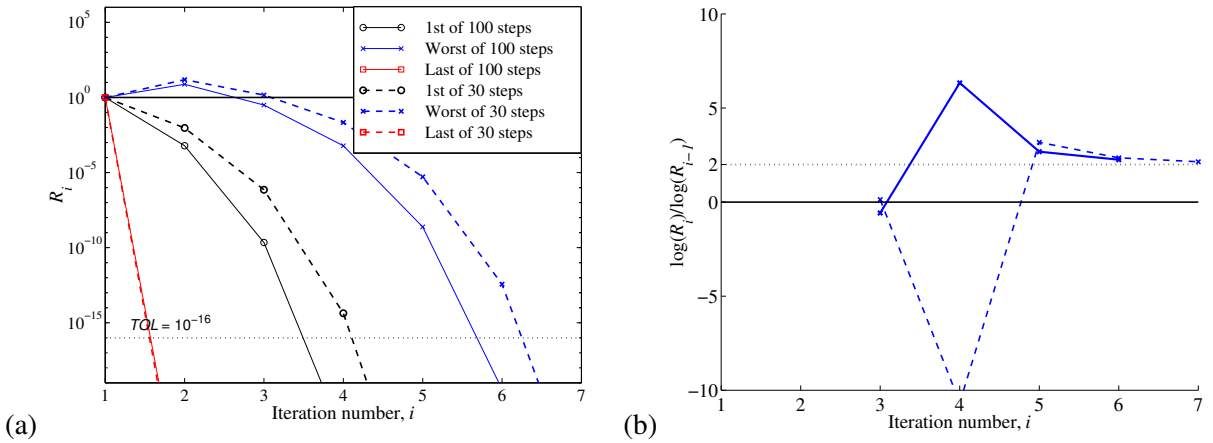

Figure 3.9: Triaxial compression of heavily overconsolidated sample. Convergence profiles of (a) normalised residual, R_i, and (b) ratio of successive logarithms, $\log R_i$.

3.5.5 Strain controlled cyclic shear loading

The numerical examples described above present an interesting comparison with the equivalent tests in Chapter 2, and also highlight some potential problems in the model. However, the main objective of the bounding surface formulation is to improve the behaviour of the MCC model for cyclic loading histories.

The response of the model to the strain-controlled cyclic shear test is shown in Fig. 3.10. As is evident from the figures, the BS model exhibits smoother hysteretic behaviour, with inelastic loading, unloading and reloading. Furthermore, stress carried on successive loading cycles is decreased in both the volumetric and deviatoric components, more representative of real soil behaviour. In contrast, successive reloading cycles in the MCC model of Section 2.5.4 led to increased levels of deviatoric stress, as the model behaviour converged to the critical state.

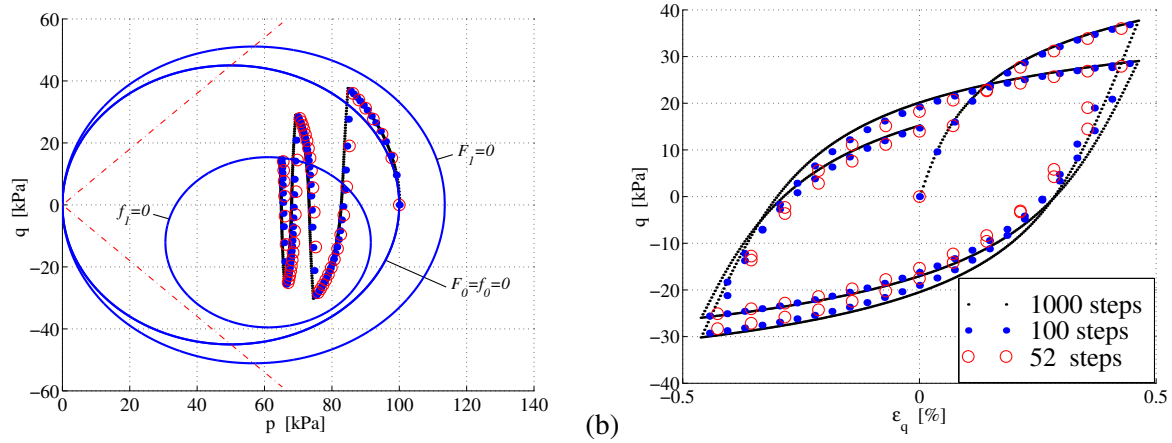

Figure 3.10: Strain controlled cyclic shear test. (a) Stress path on p–q diagram, and (b) deviatoric stress, q vs. deviatoric strain, ε_q

Provided the total number of time steps was 52 or greater, no problems were experienced on unloading in the strain-controlled test. In this loading history, unloading leads to a decrease in κ, and the back stress $\boldsymbol{\alpha}$ moves closer to the origin. For this reason, although p is decreasing with unloading, $\tilde{p}$ is always greater than $p_l/2$. This is evident from Fig. 3.10(a), where the final stress point lies in the right-hand half of the loading surface, $f_1 = 0$.

For fewer than 52 time steps, trial stress values were located in the left-hand half of the loading surface ($p^{tr} < p_l^{tr}/2$), and convergence problems were experienced. Similarly, problems arose if the magnitude of the strain cycle was increased to $\varepsilon_{12} = \pm 1.5\%$, even for 1000 time steps.

3.5.6 Stress controlled cyclic shear loading

Initially, the stress-controlled cyclic shear test described in Section 2.5.5, with $\sigma_{12} = \pm 25$ kPa was attempted for this model. This value was chosen to be similar to the simulations presented by Borja *et al.* [2001], while using material properties equivalent to those used in the MCC tests.

Under this loading history, however, the same unloading problems discussed previously were experienced here, and the stress cycle magnitude was reduced to $\sigma_{12} = \pm 15$ kPa. In this case, the entire loading history was completed for 1000 time steps, and partially completed for 100 time steps, with the results shown in Fig. 3.11. Note that in Fig. 3.11(a), the final loading surface labelled '$f_1 = 0$' applies to the 1000-time step case, for which the entire test was completed.

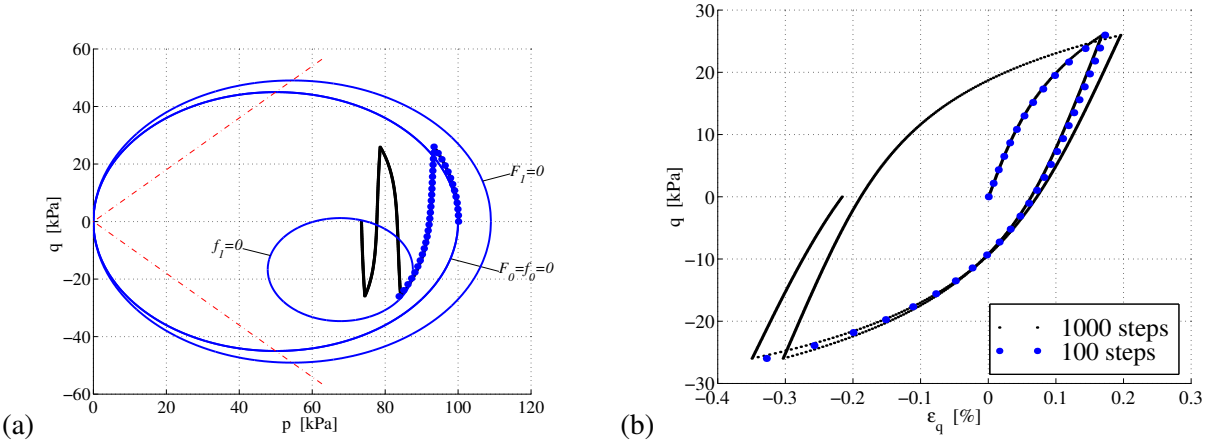

Figure 3.11: Stress controlled cyclic shear test. (a) Stress path on p–q diagram, and (b) deviatoric stress, q vs. deviatoric strain, ε_q

It is interesting to note the sensitivity of the stability of the test to relatively small changes in material parameters. For example, if the parameter M is increased to a value of 1.2, the entire load history with $\sigma_{12} = \pm 25$ kPa converges successfully for 100 time steps. Although some of the other parameters are slightly different than those used here, this roughly corresponds to the stress-controlled cyclic simple shearing test presented in Borja *et al.* [2001].

It is also worth noting that Borja *et al.* [2001] utilise the same free energy and hyperelastic stress–strain law used here, but with the addition of an extra term representing a constant shear modulus. However, in all of the tests presented in the paper, the hyperelastic parameter, α, is taken as zero, and a constant shear modulus is used. For the loading history described here, this results in a vertical stress path in the p–q plane, within the elastic nucleus, and it is less likely that the problems experienced here will arise.

In addition, the strain-controlled test simulated above is similar to the strain-controlled cyclic simple shearing test of [Borja *et al.*, 2001], and the stability of the model for this test was shown here to be sensitive to relatively small changes in the loading history.

These considerations suggest that the tests presented by Borja *et al.* [2001] are sensitive to material parameters and to the loading history, and are not sufficiently rigourous to test the solution algorithm therein.

4. GENERALISED PLASTICITY

4.1 INTRODUCTION

The Generalised Plasticity (GP) model, presented by Auricchio *et al.* [1992] and Lubliner *et al.* [1993], is an alternative representation of the cyclic behaviour of materials. In the GP framework, a yield function defines the boundary between elastic and inelastic states, while a separate limit function defines admissible and inadmissible states. The limit function and hardening laws can be selected to give a smooth, nonlinear transition from elastic to inelastic response, characteristic of most materials.

In this chapter, a model for soil plasticity is developed in the GP framework, making use of the MCC yield function used in the previous chapters. A limit function is adapted from the original papers, to be compatible with the yield function and hardening rule used here. Finally, the same numerical examples as in Chapter 2 and Chapter 3 are carried out, and results compared with the earlier models.

4.2 MODEL DESCRIPTION

4.2.1 Elastic stress–strain law

A hyperelastic stress–strain law identical to (1.13) is used with this model:

$$p = p_0 \exp\left(\frac{\theta^e}{k}\right)\left(1 + \frac{\alpha}{k}\left\|\mathbf{e}^e\right\|^2\right) \tag{4.1}$$

$$\mathbf{s} = 2\alpha p_0 \exp\left(\frac{\theta^e}{k}\right)\mathbf{e}^e \tag{4.2}$$

4.2.2 Yield and limit functions

Again, the yield function used here is the MCC surface of (1.8).

$$f(\boldsymbol{\sigma}, p_c) = \frac{3\|\mathbf{s}\|^2}{2M^2} + p(p - p_c) \tag{4.3}$$

where p_c again refers to the preconsolidation pressure of the soil.

As with the BS model of Chapter 3, the role of (4.3) is slightly different in a GP framework. The yield surface, $f = 0$, is used to define the boundary between elastic and inelastic stress points, while a separate surface, defined by the limit function, F, is used to distinguish admissible from inadmissible states. This means that, unlike in classical plasticity, the yield function is not restricted to zero or negative values. The limit function now takes this role, and the Kuhn-Tucker conditions apply:

$$\dot{\gamma} \geq 0 \qquad F(\boldsymbol{\sigma}, p_c) \leq 0 \qquad \dot{\gamma} F(\boldsymbol{\sigma}, p_c) = 0 \tag{4.4}$$

The GP model is presented conceptually in Fig. 4.1. In the inelastic range (defined by $f > 0$), the model gradually approaches an asymptote at a distance of β from the yield surface, where β is a material constant. Subsequent cycles of loading begin to yield when $f > 0$, before the previous maximum stress has been reached.

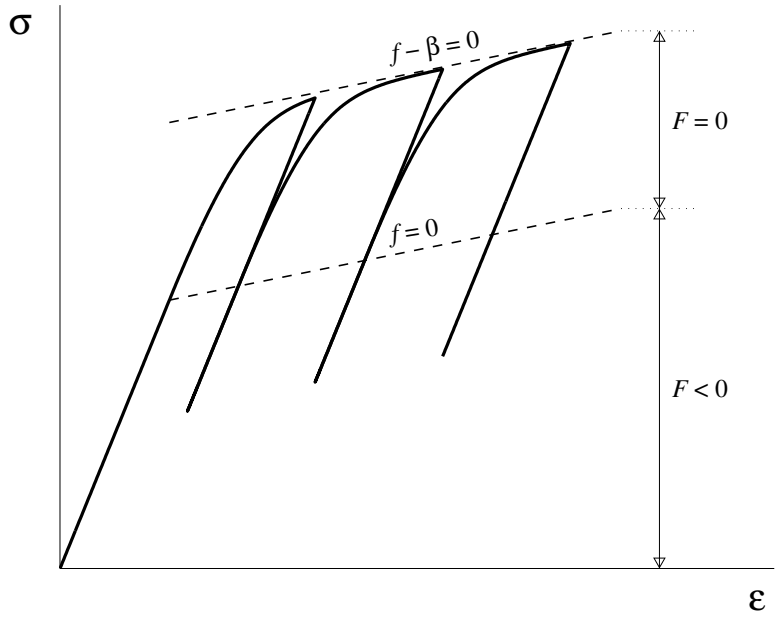

Figure 4.1: Generalised plasticity conceptual representation.

Obviously, the choice of limit function will have a significant effect on the behaviour of the model. In the original presentations of the GP model, with a J2 yield function, [Auricchio *et al.*, 1992; Lubliner *et al.*, 1993], the following limit function is assumed:

$$F = h(f)[\mathbf{n} : \dot{\boldsymbol{\sigma}}] - \dot{\gamma} \tag{4.5}$$

with

$$h(f) = \frac{f}{\delta(\beta - f) + H\beta} \quad , \qquad \mathbf{n} = \frac{\partial f}{\partial \boldsymbol{\sigma}} \tag{4.6}$$

where β and δ are material constants, having units of stress in the original model. The parameter δ gives the speed at which the model converges to an inelastic asymptote, at a distance β from the J2 yield surface. The parameter H represents the asymptotic plastic modulus of the model, obtained in the limit as $f \to \beta$.

To be consistent with (4.3), δ and H have units of stress cubed and stress squared, respectively, in the present model. Furthermore, the values of β and H cannot be taken as constant, unlike in J2 plasticity, where use of constant values followed naturally from the form of the yield surface and hardening law. Finally, in the equation for the yield surface, the hardening parameter, p_c, is not simply additive, and appears in Eq. (4.3) multiplied by p. If the limit surface is to be homologous to the yield surface, this requires an expression for β of the following form:

$$\beta = \beta_1 p \tag{4.7}$$

where β_1 is a material constant, with dimensions of stress.

Similarly, the value of H is no longer constant in the MCC version of generalised plasticity. If H is to represent the plastic modulus for $\beta = f$, then it must be obtained in the same manner as the plastic modulus for the MCC model of Chapter 2.

Recalling (2.10), we take:

$$H = \frac{p p_c (2p - p_c)}{\lambda - k} \tag{4.8}$$

Note that no new material parameters are introduced in (4.8), as the expression for the asymptotic plastic modulus follows directly from the hardening law and yield surface of the material.

4.2.3 Flow rule

The same associative flow rule as in Chapter 2 is used here. Decomposed into deviatoric and volumetric components, we have:

$$\begin{aligned} \dot{\mathbf{e}}^p &= \dot{\gamma}\left(\frac{3}{M^2}\mathbf{s}\right) \\ \dot{\theta}^p &= \dot{\gamma}\,(2p - p_c) \end{aligned} \tag{4.9}$$

4.2.4 Hardening law

The same hardening law is used as in the MCC model:

$$p_c = p_{c0} \exp\left(\frac{1}{\lambda - k}\theta^p\right) \tag{4.10}$$

As with the BS formulation, (4.10) does not contain all information about hardening in the model. With BS plasticity, the evolutionary equation for p_c described hardening of the bounding surface, while a separate equation was required for evolution of the loading surface hardening parameter, p_l. In the GP formulation, (4.10) describes hardening of the yield surface, while (4.5) and (4.8) implicitly define hardening of a surface given by $f = \beta$.

Remark 4.1. In combination with the Kuhn-Tucker conditions (4.4), Eq. (4.5) effectively provides a direct expression for the consistency parameter, $\dot{\gamma}$. In the inelastic region, with $F = 0$ and $\dot{\gamma} > 0$, we have:

$$\dot{\gamma} = h(f)[\mathbf{n} : \dot{\boldsymbol{\sigma}}] \tag{4.11}$$

This can be compared with the expression for the consistency parameter for yielding from classical plasticity:

$$\dot{\gamma} = \frac{1}{\mathcal{H}}[\mathbf{n} : \dot{\boldsymbol{\sigma}}] \tag{4.12}$$

in which $\mathcal{H}$ is the plastic modulus.

Therefore, the combination of (4.11) and (4.12) gives the following expression for the plastic modulus:

$$\mathcal{H} = \frac{1}{h(f)} = \frac{\delta(\beta - f) + H\beta}{f} \tag{4.13}$$

which tends to the asymptotic plastic modulus, H, as f tends to β.

Remark 4.2. The similarities between the GP model and the BS model described in Chapter 3 should be evident. Eq. (4.13) gives an expression for the plastic modulus of the GP formulation that depends on β/f, δ and H, roughly corresponding to $(1 + \kappa)$, hardening parameters h and m, and $\hat{\mathcal{H}}$ from Chapter 3, respectively. Similarly, (3.20) gives an expression for the plastic modulus of the BS model in terms of these parameters, although not in the same format.

Comparing the GP and BS models, the following comments can be made:

1. The GP model assumes the existence of an elastic region for which $f < 0$, and plastic strain rates are zero. The BS model includes a small 'elastic nucleus' in the time discrete version of the model for computational purposes only, and plastic strain increments are in general non-zero.

2. In the BS model, the distance between the loading and bounding surfaces is not fixed, and hardening equations governing the size of each surface are separate, although not independent. The hardening equation given for the size of the loading surface is such that it is confined by the bounding surface.

   In the GP model, admissible stress states are bounded by a surface $f - \beta_1 p = 0$ — an ellipse in the p–q plane homologous to the yield surface, which intercepts the p–axis at $p_c + \beta_1$. The model parameter β_1 is taken as constant, so that the difference between the yield surface and the limiting

surface is fixed. However, the consistency condition is not applied to the yield equation, so the stress point is allowed to approach the asymptote, as in the BS model.

3. Unloading is elastic in the GP model, while for the BS model, detection of the unloading condition results in a discrete relocation of the homology centre, and inelastic loading continues from this new point. That is, 'unloading' never occurs.

   Note, however, that kinematic hardening can be readily incorporated into the GP framework, as in the original papers [Auricchio *et al.*, 1992; Lubliner *et al.*, 1993].

Finally, it should be noted that with appropriate manipulation of the expressions for plastic moduli, (3.20) and (4.13), the BS model could be reformulated within the framework of GP plasticity, and vice versa. For example, Eq. (4.5) could be used with:

$$h(f, \kappa, p_l) = \frac{1}{\mathcal{H}} \tag{4.14}$$

where $\mathcal{H}$ is obtained directly from (3.20), with parameters κ and p_l defined as in Chapter 3.

Clearly, reformulating the anisotropic BS model in the GP framework would require additional evolutionary equations for the homology centre, as in Chapter 3. However, as stated above, generalised plasticity is fully compatible with kinematic hardening, and this should not present any difficulties.

4.3 DISCRETE FORM OF MODEL

As in the previous models, we use backward Euler integration to obtain a time discrete form of the model. As before, we have:

$$\begin{aligned} \mathbf{e}^p &= \mathbf{e}^p_n + \Delta\gamma \frac{3}{M^2}\mathbf{s} \\ \theta^p &= \theta^p_n + \Delta\gamma(2p - p_c) \end{aligned} \tag{4.15}$$

with

$$\Delta\gamma = \int_{t_n}^{t_{n+1}} \dot{\gamma} \mathrm{d}t$$

and the same expressions for p and $\mathbf{s}$:

$$p = p_0 \exp\left(\frac{\theta - \theta^p_n - \Delta\gamma(2p - p_c)}{k}\right)\left[1 + \frac{\alpha}{k}\|\mathbf{e} - \mathbf{e}^p_n - \Delta\gamma\frac{3}{M^2}\mathbf{s}\|^2\right] \tag{4.16}$$

$$\mathbf{s} = \frac{2\alpha p_0 \exp\left(\frac{\theta-\theta^p_n}{k}\right)\exp\left(\frac{-\Delta\gamma(2p-p_c)}{k}\right)}{1 + \frac{6\alpha p_0}{M^2}\Delta\gamma \exp\left(\frac{\theta-\theta^p_n}{k}\right)\exp\left(\frac{-\Delta\gamma(2p-p_c)}{k}\right)}\left[\mathbf{e} - \mathbf{e}^p_n\right] \tag{4.17}$$

Because of the form being used for the limit function, this must also be integrated to obtain an appropriate time discrete form. If (4.5) is integrated in its current form, the value of $\boldsymbol{\sigma}$ at the previous time step, $\boldsymbol{\sigma}_n$ will need to be stored for the next time step, adding six internal variables to the model. It will be more efficient to make a manipulation of (4.5) before integrating.

Note that the implied definition of $\mathbf{n}$ from $(4.6)_2$ is:

$$\mathbf{n} = \frac{\partial f}{\partial \boldsymbol{\sigma}}\Big|_{p_c=\text{constant}} = \frac{d\hat{f}}{d\boldsymbol{\sigma}} \tag{4.18}$$

where

$$\hat{f}(\boldsymbol{\sigma}) = f(\boldsymbol{\sigma}, p_c)\big|_{p_c=\text{constant}} \tag{4.19}$$

Substituting (4.18) into (4.5), we obtain:

$$F = h(f)\dot{\hat{f}} - \dot{\gamma} = 0 \tag{4.20}$$

Implicit integration gives the discrete equivalent of the limit function:

$$F_{disc} = h[\hat{f} - \hat{f}_n] - \Delta\gamma \tag{4.21}$$

The term in brackets, $[\hat{f} - \hat{f}_n]$, requires further clarification. This is the discrete change in the function $\hat{f}$ over the time step. Noting the definition of $\hat{f}$, this requires that p_c is kept constant over the time step. Therefore, the following expressions apply:

$$\hat{f}_n = f(\boldsymbol{\sigma}_n, p_{cn}) = f_n \qquad\qquad \hat{f} = f(\boldsymbol{\sigma}, p_{cn}) \tag{4.22}$$

from which we see that the only stored variables required from time t_n are f_n and p_{cn}.

4.4 RETURN MAP ALGORITHM

Because most of the equations here are identical to those used in Chapter 2, the return map algorithm is very similar to that used before. However, now the consistency condition, $(4.4)_2$ is enforced on the limit function, F.

4.4.1 Trial state

The trial values used here are identical to Chapter 2, as defined in (2.16).

In the present model, the role of the limit function is to define the boundary between admissible and inadmissible states. Therefore, it is the trial limit function which must be used to determine if the time step is accurately described by the elastic trial state. Substituting trial state values from (2.16), the trial limit function is given by:

$$F^{tr}_{disc} = h(f^{tr})[\hat{f}^{tr} - \hat{f}_n] \tag{4.23}$$

Note that from $(4.22)_2$, we can take:

$$\hat{f}^{tr} = f(\boldsymbol{\sigma}^{tr}, p_{cn}) = f(\boldsymbol{\sigma}^{tr}, p_c^{tr}) = f^{tr} \tag{4.24}$$

and, substituting from $(4.22)_1$ and (4.24) into (4.23) gives:

$$F_{disc}^{tr} = h(f^{tr})[f^{tr} - f_n] \tag{4.25}$$

Again, we must compare this value with the second Kuhn-Tucker condition, $(4.4)_2$. If $F_{disc}^{tr} \leq 0$, then the trial state given by (2.16) is the correct solution. Otherwise, if $F_{disc}^{tr} > 0$ the Kuhn-Tucker condition is violated, and a plastic correction must be made to obtain the correct stress state.

There is, however, additional complication in using the above condition for acceptance of the trial state. It is important to consider the physical meanings of the two components of (4.25), $h(f^{tr})$ and $[f^{tr} - f_n]$. Provided that the denominator of h in (4.6) remains positive (see Remark below), $h(f^{tr}) < 0$ implies that the trial stress state is in the elastic region.

Meanwhile, if $[f^{tr} - f_n] < 0$, the stress point is becoming closer to the origin, which implies an unloading stress path. This is a generalisation of the unloading condition used in classical plasticity, and in the MCC and BS models of Chapters 2 and 3. In classical plasticity, $f_n = 0$, which gives a condition $f^{tr} < 0$ for unloading. In generalised plasticity, the consistency condition is no longer enforced on f, and f_n will be greater than zero in the plastic range.

If we desire elastic unloading, the condition $F_{disc}^{tr} \leq 0$ should apply in all cases when $[\hat{f}^{tr} - \hat{f}_n] < 0$ applies. However, if we take:

$$[\hat{f}^{tr} - \hat{f}_n] < 0, \qquad \text{and} \qquad h(f^{tr}) < 0,$$

a condition of unloading in the elastic region, (4.25) gives a positive value of F_{disc}^{tr}.

The implication of the above discussion is that we must check both the trial yield function and the direction of loading in our evaluation of the trial state. An appropriate pair of expressions to use for this purpose are:

$$f^{tr} > 0 \qquad \text{and} \qquad [\hat{f}^{tr} - \hat{f}_n] > 0 \tag{4.26}$$

If both (4.26) equations are satisfied, then we must make the plastic correction. In words, if the stress state is in the inelastic region, *and* it is a loading stress path, then we have a plastic time step. Otherwise, the trial state is correct.

Remark 4.3. The generalised plasticity framework requires that the function h is greater than zero when f is greater than zero. If $\mathbf{n} : \dot{\boldsymbol{\sigma}} > 0$ in a time continuous setting, or (4.26) is satisfied in a time discrete setting, the Kuhn-Tucker conditions (4.4) require that $F = 0$ and the continuous or discrete consistency

parameter is greater than zero. From the appropriate expression for F, (4.5) or (4.21), and the definition of h, Eq. (4.6), we require that the denominator of h is greater than zero.

From (4.6), we have:

$$\delta(\beta - f) + H\beta > 0 \tag{4.27}$$

which can be rearranged to give the following inequality for H:

$$H > \delta\left(\frac{f}{\beta} - 1\right) \tag{4.28}$$

Eq. (4.28) presents no difficulties for cases of hardening in a time continuous setting. In this case $H > 0$ and $f/\beta < 1$, which satisfies the inequality. In fact, negative values of H may also be permitted, particularly for low values of f and high values of δ.

Theoretically, the same argument applies to a time discrete setting. However, if H is replaced by the trial asymptotic modulus, $H^{tr} = H\left(p^{tr}, p_c^{tr}\right)$, we have:

$$H^{tr} > \delta\left(\frac{f^{tr}}{\beta^{tr}} - 1\right) \tag{4.29}$$

where $\beta^{tr} = \beta_1 p^{tr}$, and f^{tr} is defined as before.

For stress states near the CSL, H^{tr} can take a negative value, even when the converged value of H is positive. Similarly, f^{tr} could be overpredicted, and may exceed β^{tr}. This situation could lead to the violation of (4.29), and convergence problems may be encountered.

If $h^{tr} > 0$ is used in place of $(4.26)_1$ as a condition for a plastic time step, an elastic time step will be assumed, and the trial state will be erroneously accepted. If $(4.26)_1$ is used, a plastic time step will be correctly predicted. However, convergence problems may be experienced in the plastic correction stage.

These problems will be further explored in Section 4.5.

4.4.2 Plastic Correction

The plastic correction step is developed in exactly the same manner as in previous chapters. As before, p_c, p and $\mathbf{s}$ must satisfy (4.10), (4.16) and (4.17), respectively, while the second Kuhn-Tucker condition $(4.4)_2$ is now enforced on the limit function.

Therefore, we introduce the same vector of unknowns, $\boldsymbol{x}$, and a modified vector of residuals, $\mathbf{g}(\boldsymbol{x})$:

$$\boldsymbol{x} = \begin{Bmatrix} p \\ p_c \\ \Delta\gamma \end{Bmatrix} \; ; \quad \mathbf{g}(\boldsymbol{x}) = \begin{Bmatrix} g_1 \\ g_2^{MCC} \\ g_3^{MCC} \end{Bmatrix} = \begin{Bmatrix} h(\hat{f} - \hat{f}_n) - \Delta\gamma \\ p_0 A_1 A_2 A_6 - p \\ p_c^{tr} \exp\left(\frac{2p - p_c}{\lambda - k}\Delta\gamma\right) - p_c \end{Bmatrix} \tag{4.30}$$

where the MCC superscripts emphasise that these components of $\mathbf{g}$ are unchanged from Chapter 2. As before we iterate using:

$$\boldsymbol{x}^{(k+1)} = \boldsymbol{x}^{(k)} - \left[\frac{\partial \mathbf{g}}{\partial \boldsymbol{x}}\right]^{-1} \mathbf{g}\left(x^{(k)}\right) \tag{4.31}$$

until the convergence condition:

$$\|\mathbf{g}\|^* = \sqrt{(g_1)^2 + \left(\frac{g_2}{p_0}\right)^2 + \left(\frac{g_3}{p_{c0}}\right)^2} < TOL \tag{4.32}$$

is satisfied.

Again, residual gradient calculations are confined to Appendix E. It is worth noting that only the first row of $\partial \mathbf{g}/\partial \boldsymbol{x}$ is changed from the MCC model, as g_2 and g_3 are the same as in Chapter 2.

Remark 4.4. In the original presentations of the model for J2 Plasticity, [Auricchio *et al.*, 1992; Lubliner *et al.*, 1993], a quadratic expression for $\Delta\gamma$ was developed in closed form, and it was shown that the smallest positive root of this equation corresponded to the physically correct root.

As with the models in previous chapters, a Newton algorithm will be required here to determine appropriate plastically-corrected values of $\Delta\gamma$, $\boldsymbol{\sigma}$ and p_c. No check is available to determine if the correct root of $\Delta\gamma$ has been calculated. In fact, Remark 4.3 suggests that negative values of $\Delta\gamma$ may be obtained for certain loading histories, which contradicts the Kuhn-Tucker conditions (4.4).

This presents a possible shortcoming of the proposed model, although further investigation into the extent of the problem is required. In particular, alternative initial conditions for the Newton algorithm, other than the trial state, could be explored.

4.4.3 Consistent tangent

Elastic step

The elastic behaviour of the GP model is identical to the MCC model of Chapter 2, as the yield surface is the same. Repeating the expression obtained in Section 2.4.3, we have:

$$\mathbb{C}^e = \frac{p_0}{k} \exp\left(\frac{\theta^e}{k}\right) \left[2\alpha k \mathbb{I}_{\text{dev}} + 3\left(1 + \frac{\alpha}{k}\|\mathbf{e}^e\|^2\right)\mathbb{I}_{\text{vol}} + 2\alpha\left(\mathbf{1} \otimes \mathbf{e}^e + \mathbf{e}^e \otimes \mathbf{1}\right)\right] \tag{4.33}$$

Plastic step

As before, the following expression applies:

$$\mathbb{C}^{\text{p}} = \mathbf{1} \otimes \frac{\partial p}{\partial \boldsymbol{\varepsilon}^{e,tr}} + \frac{\partial \mathbf{s}}{\partial \boldsymbol{\varepsilon}^{e,tr}} \tag{4.34}$$

The procedure is exactly the same as before, and most equations are unchanged. The only difference is in the enforcement of the consistency condition, which is now defined on the limit function, F. The final expression:

$$\mathbb{C}^{\mathrm{p}} = \hat{E}_1 \mathbf{1} \otimes \mathbf{s} + \hat{E}_2 \mathbf{1} \otimes \mathbf{1} + \hat{E}_3 \mathbf{s} \otimes \mathbf{1} + \hat{E}_4 \mathbf{s} \otimes \mathbf{s} + \hat{E}_5 \mathbb{I}_{\mathrm{dev}} \tag{4.35}$$

is derived in Appendix F. The constants $\hat{E}_1$–$\hat{E}_5$ are very similar to their MCC counterparts.

4.4.4 Converting to 'mechanical' sign convention

As before, we have:

$$\mathbb{C}^{\mathrm{e},m} = \frac{p_0}{k} \exp\left(\frac{\theta^e}{k}\right) \left[2\alpha k \mathbb{I}_{\mathrm{dev}} + 3\left(1 + \frac{\alpha}{k}\|\mathbf{e}^e\|^2\right)\mathbb{I}_{\mathrm{vol}} - 2\alpha\left(\mathbf{1} \otimes \mathbf{e}^e + \mathbf{e}^e \otimes \mathbf{1}\right)\right] \tag{4.36}$$

and

$$\mathbb{C}^{\mathrm{p},m} = -\hat{E}_1 \mathbf{1} \otimes \mathbf{s} + \hat{E}_2 \mathbf{1} \otimes \mathbf{1} - \hat{E}_3 \mathbf{s} \otimes \mathbf{1} + \hat{E}_4 \mathbf{s} \otimes \mathbf{s} + \hat{E}_5 \mathbb{I}_{\mathrm{dev}} \tag{4.37}$$

where the constant terms are the same as for the compression positive case, with negative signs as shown.

4.5 NUMERICAL TESTS

The same finite element simulations as in previous chapters were conducted using the GP model, using the material parameters summarised in Table 4.1. As before, the parameter p_0 varies for each test, and the form of the stress–strain law prohibits an initial pressure of zero.

Table 4.1: Generalised Plasticity model parameters

Parameter	α	M	λ	k	p_{c0}	δ	β_1
Value	100	0.9	0.09	0.02	200 kPa	$1 \times 10^7 (kPa)^3$	100 kPa

4.5.1 Isotropic compression test

Fig. 4.2 shows the loading, unloading and reloading behaviour of the model under isotropic compression. Results are shown for six, 100 and 1000 stress increments, and the accuracy of the solution algorithm, can be observed.

An interesting feature of Fig. 4.2(a) is the onset of yielding before the previous maximum stress level is obtained. Comparing with Fig. 2.1(a), the elastic behaviour, experienced on unloading and reloading of the sample, is identical. The plastic behaviour exhibits an initially convex stress–strain response, which evolves into the concave response characteristic of the MCC model as f increases.

In Fig. 4.2(b) the $\ln v$–$\ln p$ relationship deviates slightly from the bilinear form used as the basis of the model, with a more gradual transition from the elastic to the inelastic branches of the graph. The parameter k is correctly obtained for the elastic straight line portion of the graph, while λ is found in the limit for the inelastic portion, as shown in Fig. 4.2(b).

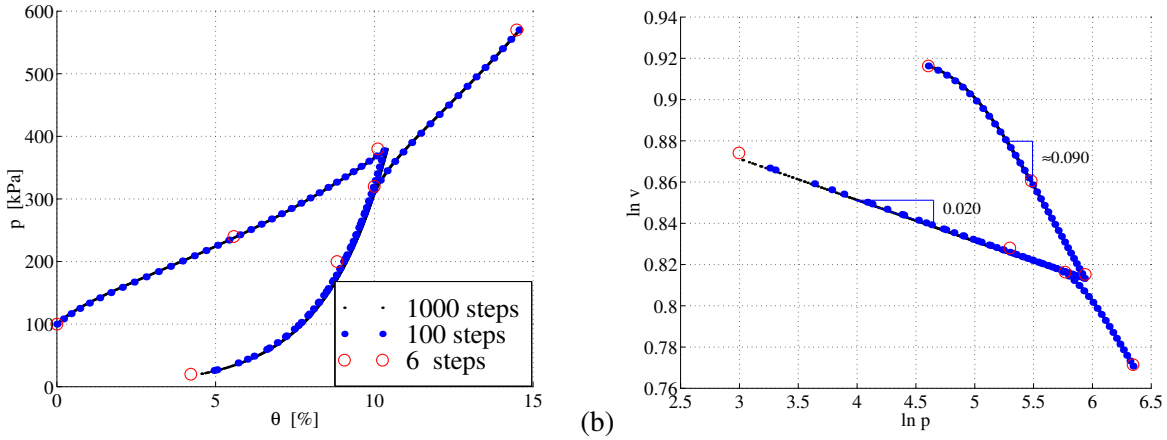

(a) (b)

Figure 4.2: Isotropic compression test. (a) Volumetric stress, p, vs. volumetric strain, θ, and (b) bilinear $\ln v$ vs. $\ln p$ relationship.

The convergence profiles are again compared for first, 'worst' and last integration steps, in Fig. 4.3. In all cases, convergence is achieved quadratically, within five iterations with 100 time steps, and six iterations with six time steps (Fig. 4.3(a)). It is interesting to note that ten iterations were required in the latter case, using the MCC model (Fig. 2.2).

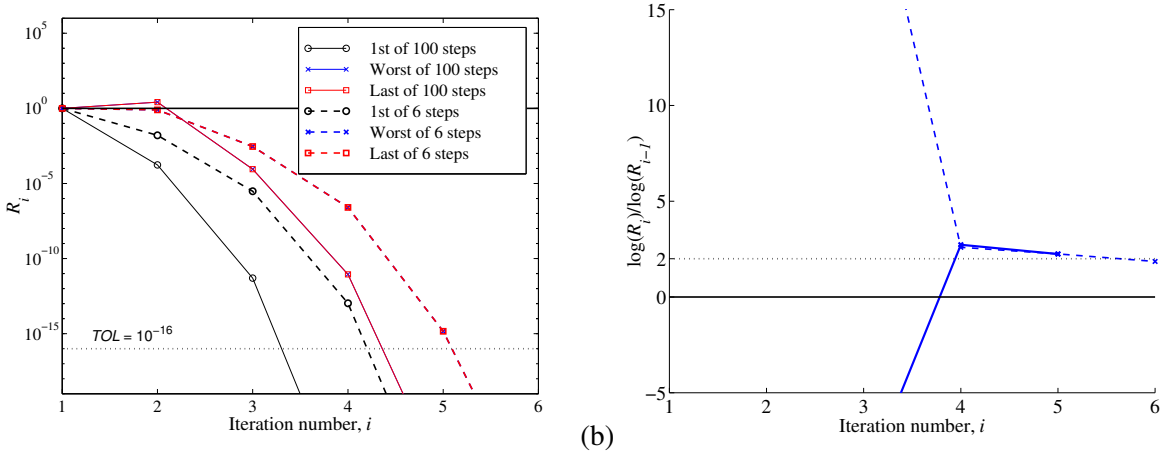

(a) (b)

Figure 4.3: Isotropic compression test. Convergence profiles of (a) normalised residual, R_i, and (b) ratio of successive logarithms, $\log R_i$.

4.5.2 Triaxial compression of lightly consolidated sample

Results from the triaxial compression test simulation are presented in Fig. 4.4. The model exhibited convergence problems, even for the case of 100 time steps, and the last data point plotted for 100 and

18 time steps runs in Fig. 4.4 represent the last convergent step. In each case, the number of time steps reported (1000, 100 and 18 steps) represents the number of steps that would have been completed if the full loading history described in Section 2.5.2 had been completed, and not the actual number of convergent time steps. This corresponds to an increment in the controlled strain component of approximately 0.07%, 0.7% and 4%, respectively.

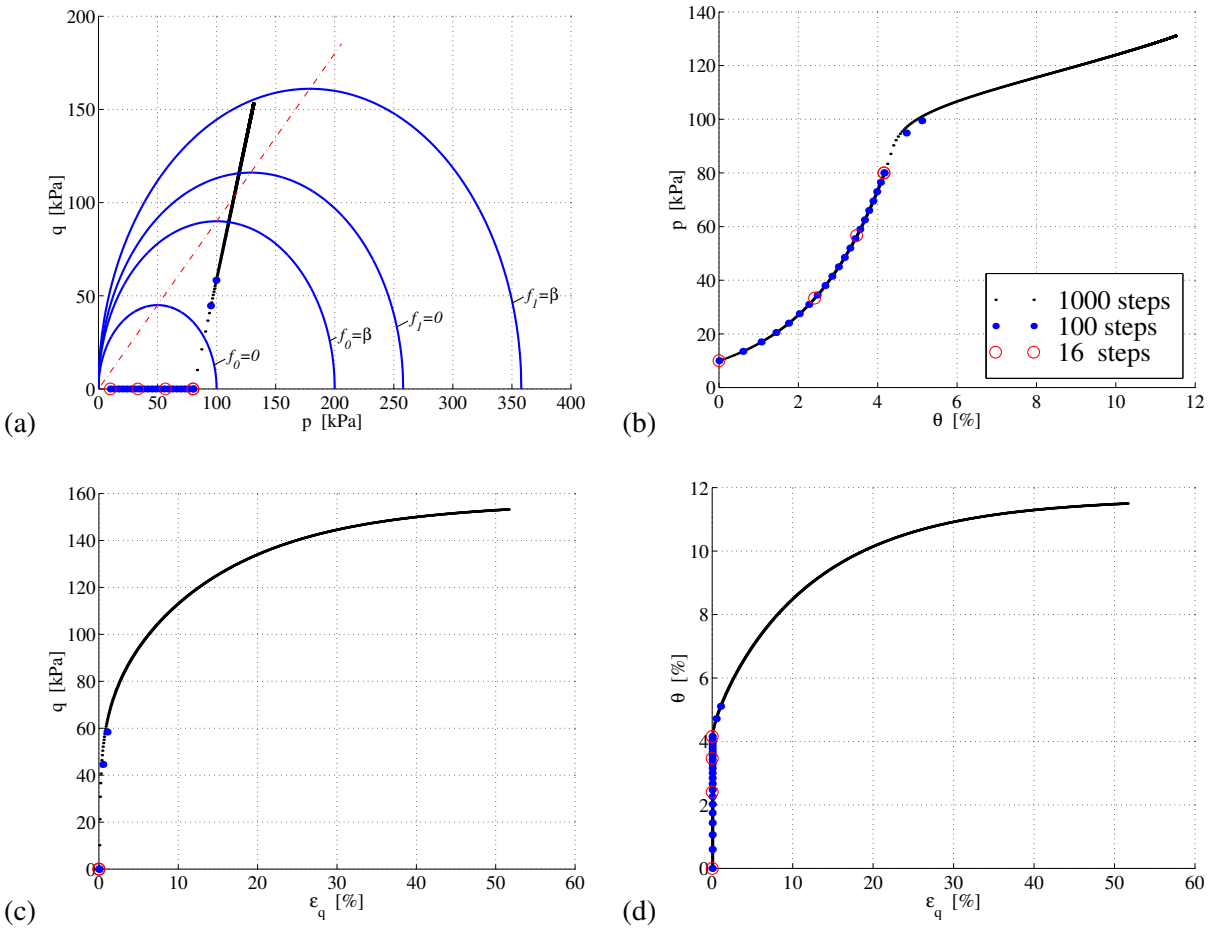

Figure 4.4: Triaxial compression of lightly overconsolidated sample. (a) Stress path on p–q diagram, (b) volumetric stress, p, vs. volumetric strain, θ, (c) deviatoric stress, q, vs. deviatoric strain, ε_q, and (d) θ vs. ε_q.

The convergence difficulties exhibited in this simulation highlight a significant problem with the current version of the GP model. The output files from each of the analyses revealed that the problem predicted in Remark 4.3 is responsible, with Eq. (4.29) violated in each of the non-convergent time steps. As suggested in the remark, a small or negative asymptotic plastic modulus, H, results in a negative value for the function h, which is not compatible with the Kuhn-Tucker requirement, $(4.4)_1$. For the analyses that experienced problems here, the final non-convergent time step corresponds to a trial stress state for which $p^{tr} < p_c^{tr}/2$, leading to $H^{tr} < 0$ from (4.8), and violation of (4.29).

Fig. 4.4(a) also highlights an unfavourable aspect of the current model related to the modelling of the 'critical state concept' introduced in Section 1.6. With 1000 time steps, Figures 4.4(b) and (c) indicate

that the critical state has been effectively reached when convergence problems occur, with no further increase in stress or volumetric stain occurring. However, Fig. 4.4(a) shows that the final stress state does not lie on the CSL in the p–q plane, and the geotechnical interpretation of the CSL (and the slope, given by the parameter M) is no longer valid.

The reinterpretation of the critical state concept is a result of the use of a flow rule associated with the yield surface, which, in the present model, is not restricted to zero or negative values. For the MCC and BS models discussed in the previous chapters, plastic flow was associated with a surface that passed through the current stress state — the yield surface or the loading surface respectively — and the direction of plastic flow could be found from the gradient to the surface at that stress state. In the GP formulation discussed here, the gradient of the yield surface for the current stress state will not necessarily correspond to an appropriate flow direction. In this case, we have a final stress state corresponding to $p \approx p_c/2$, for which $(4.9)_2$ gives a volumetric strain rate of zero — a 'critical state' not lying on the CSL.

Fig. 4.5 shows the implications of using flow associated with the yield surface, $f = 0$. A surface defined by $F = 0$ is plotted as a dotted line passing through the current stress state, and the surface $f = \beta$ is also shown. The gradient of $F = 0$ at the current stress point is decomposed into volumetric and deviatoric parts, and is indicated by the '1' subscript in Fig. 4.5. The direction of flow given by these two components is representative of the associative flow rules used for the MCC and BS models.

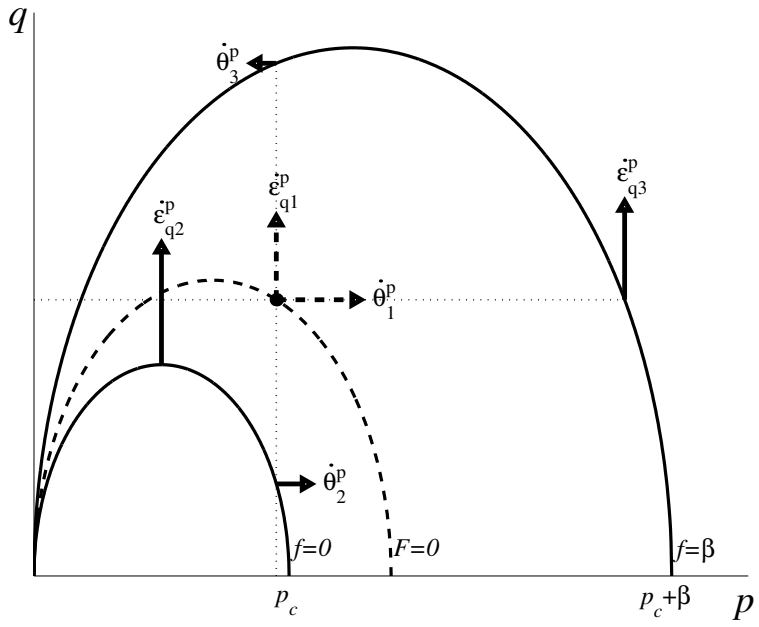

Figure 4.5: Generalised plasticity with flow rules associated with (1) $F = 0$, (2) $f = 0$ and (3) $f = \beta$.

For the GP model, (4.9) is used to evaluate the deviatoric and volumetric strain rates, and the former rate is converted to $\dot{\varepsilon}_q^p$ using (2.39). These two components of flow are indicated by the '2' subscript in Fig. 4.5. Note that for the case shown, $\dot{\theta}_2^p$ is equivalent to the volumetric component of the gradient of $f = 0$ with the current value of p. The current value of q does not correspond to a stress state on $f = 0$

— the deviatoric plastic strain rate, $\dot{\varepsilon}^p_{q2}$ is still calculated from (4.9) and (2.39), although the physical significance of being a gradient to a surface is lost.

The resultant strain rate $\dot{\boldsymbol{\varepsilon}}^p_2$ assumed in the GP model, from the vector addition of $\dot{\theta}^p_2$ and $\dot{\varepsilon}^p_{q2}$, is clearly different from that used in the previous models (equivalent to $\dot{\boldsymbol{\varepsilon}}^p_1$ in Fig. 4.5), and, as shown above, leads to an incorrect interpretation of the critical state. A second model in the GP framework was also developed, using a flow rule associated with the surface defined by $f = \beta$. However, as suggested by the strain rate components with subscript '3' in Fig. 4.5, the behaviour of this model was also contrary to experimental evidence, and the 'critical state concept' of soil mechanics.

Fig. 4.5 and the above discussion suggest two possible solutions to the problem. Firstly, a flow rule associated with the surface $F = 0$ could be used. However, the evaluation of:

$$\dot{\boldsymbol{\varepsilon}}^p = \dot{\gamma}\frac{\partial F}{\partial \boldsymbol{\sigma}}$$

could present some difficulty, given that the expression for F, Eq. (4.5), contains the consistency parameter $\dot{\gamma}$.

A second possible solution is the adoption of a mapping rule, similar to that used in Chapter 3, which defines a stress state corresponding to the current stress state mapped onto either $f = 0$ or $f = \beta$. As with the BS model, either of these alternatives would be equivalent to a flow rule associated with $F = 0$, as the surfaces are defined homologously. Although the GP model would retain some independence from the model discussed in Chapter 3 — Eq. (4.5) would still be used to provide a smooth transition between elastic and inelastic states rather than hardening rules based on the aspect ratios of the surfaces — the distinction between the two would be less significant, and the relative simplicity of the original GP formulation would be sacrificed.

The principal difficulty here lies in adopting the GP framework to a non-J2 plasticity model. In J2 plasticity, the surfaces defined by $f = 0$, $F = 0$ and $f = \beta$ form concentric circles in the Π–plane (deviatoric stress space), and the vectors defined by the following gradients:

$$\mathbf{n}_1 = \frac{\partial f}{\partial \boldsymbol{\sigma}} \quad ; \quad \mathbf{n}_2 = \frac{\partial F}{\partial \boldsymbol{\sigma}} \quad ; \quad \mathbf{n}_3 = \frac{\partial (f-\beta)}{\partial \boldsymbol{\sigma}} \tag{4.38}$$

are parallel. This allows a simple scalar equation like (4.5) to be defined, which scales the magnitude of the flow rate to provide a smooth transition from elasticity to inelasticity.

With a Cam-Clay yield surface, the three vectors defined in (4.38) will in general point in different directions, as shown in Fig. 4.5, and a scalar multiplier of $\mathbf{n}_2$ will not be sufficient to effectively model the transition region.

Notwithstanding the problems discussed above, the convergence of the solution algorithm was assessed for the 1000-time step and 100-time step test runs. In the case of 18-time steps, only the isotropic

hardening portion of the loading history converged, and the behaviour of the model under isotropic hardening has already been assessed in the previous section. In the 100-time step test run presented in Figures 4.6(a) and (b), 'last' time step refers to the last convergent step, and 'worst' is defined as before. Both test runs exhibit quadratic convergence, within 5 iterations for all time steps.

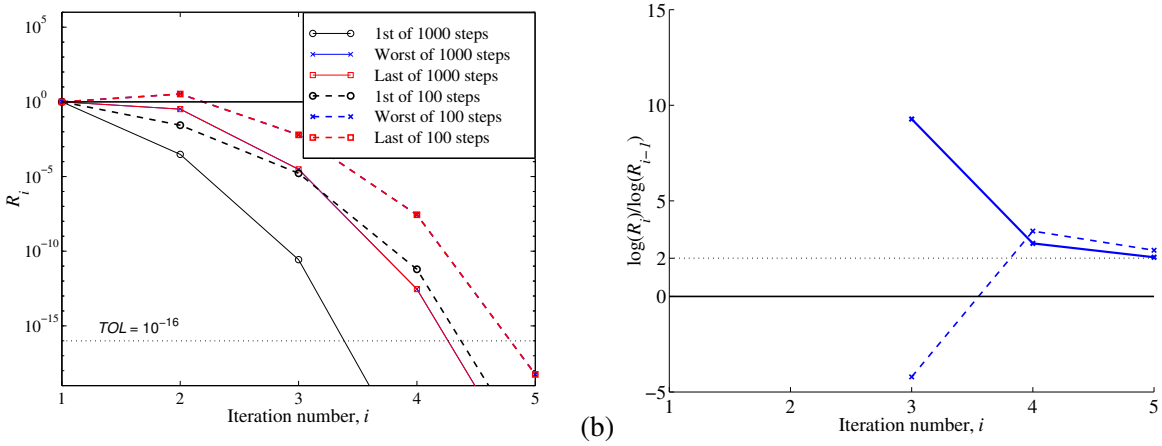

(a) (b)

Figure 4.6: Triaxial compression of lightly overconsolidated sample. Convergence profiles of (a) normalised residual, R_i, and (b) ratio of successive logarithms, $\log R_i$.

4.5.3 Triaxial compression of heavily overconsolidated sample

In Section 2.5.3, a triaxial compression test of a heavily consolidated sample was simulated with a MCC model, and quadratic convergence was reported for softening behaviour with a negative plastic modulus. As discussed in Remark 4.3, a negative asymptotic plastic modulus, H, may be admissible, provided that (4.28) is not violated. The results of the simulation presented in this section are therefore of some interest to assess the importance of the conditions presented in Remark 4.3.

The results are shown in Fig. 4.7. In all test runs, the model failed to converge for the complete load history — for 100 and 18 total time steps, only the isotropic portion of the load path was completed, while for 1000 time steps, the model continued to converge for several steps beyond yield. In all cases, convergence failed at the final step shown in Fig. 4.7 due to the violation of (4.28).

For the 1000-time step case, some yielding is admitted for $p < p_c/2$ and $H < 0$. However, although some compaction ($\Delta\theta^p < 0$) is indicated by Fig. 4.7(d), softening, or reduction of the stress carried by the soil, does not occur (Figures 4.7(b) and (c)). The form of the instantaneous plastic modulus in (4.13) indicates $\mathcal{H} < 0$ only when $h(f) < 0$, and because $h(f)$ is restricted to positive values by the considerations discussed in Remark 4.3, no softening behaviour can be described by the GP model. In the analysis described here, convergence is achieved while (4.28) is satisfied, but as f increases, the denominator of h in (4.6) decreases. Eventually, the denominator becomes negative, and the model fails to converge.

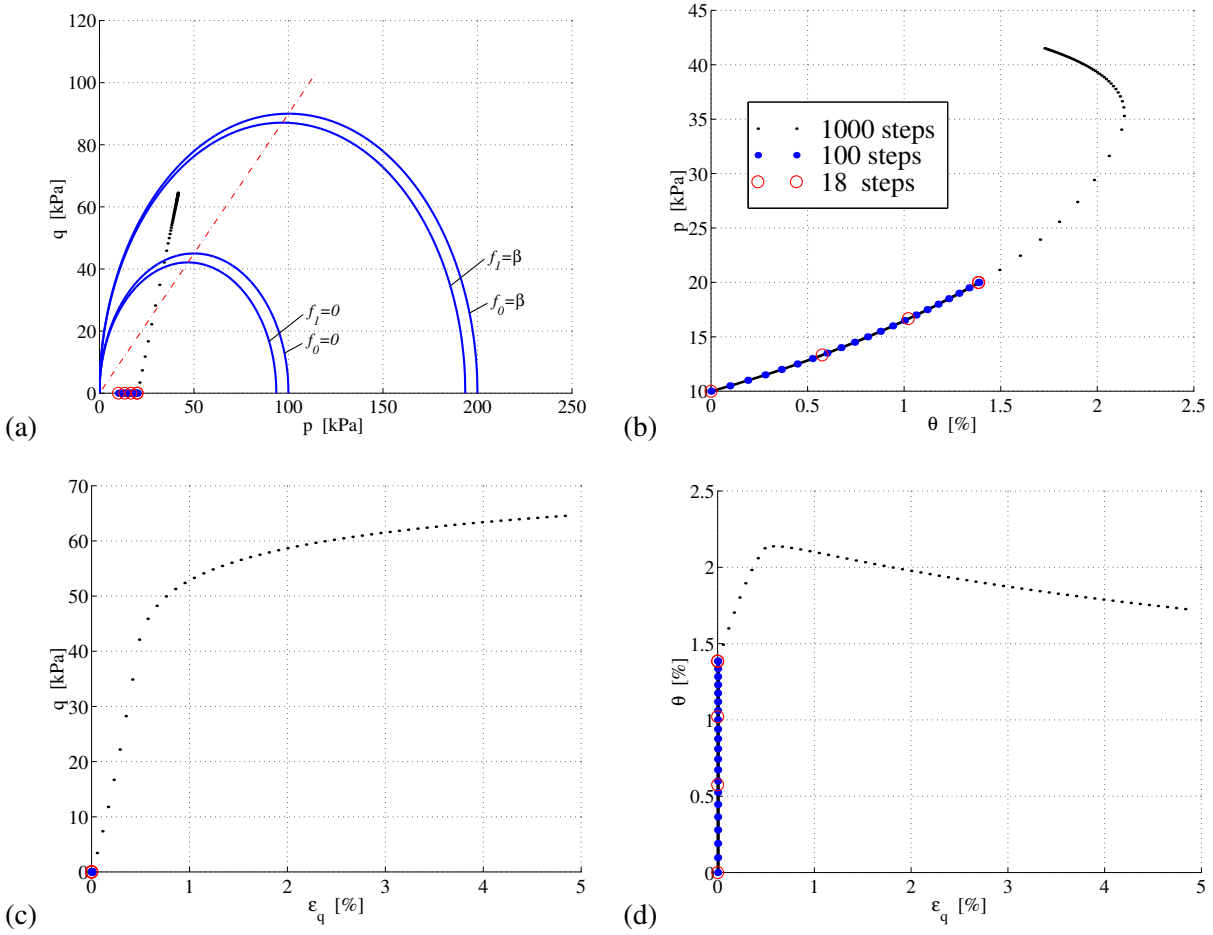

Figure 4.7: Triaxial compression of heavily overconsolidated sample. (a) Stress path on p–q diagram, (b) volumetric stress, p vs. volumetric strain, θ, (c) deviatoric stress, q vs. deviatoric strain, ε_q, and (d) θ vs. ε_q.

For the convergent steps in the 1000-time step analysis, convergence profiles are given in Fig. 4.8. Where the model converges successfully, it does so quadratically, as shown for the first, worst and last convergent time steps in the analysis.

4.5.4 Strain controlled cyclic shear loading

Fig. 4.9 show the behaviour of the GP model under the strain-controlled cyclic loading history, for 1000, 100 and 16 time steps. Comparing with Fig. 2.7, the GP formulation results in a smoother transition from elastic to inelastic behaviour, and a slightly smaller increase in maximum deviatoric stress over successive load cycles. However, overall the behaviour is very similar to the MCC model, and the hysteretic response of a real soil is not described accurately.

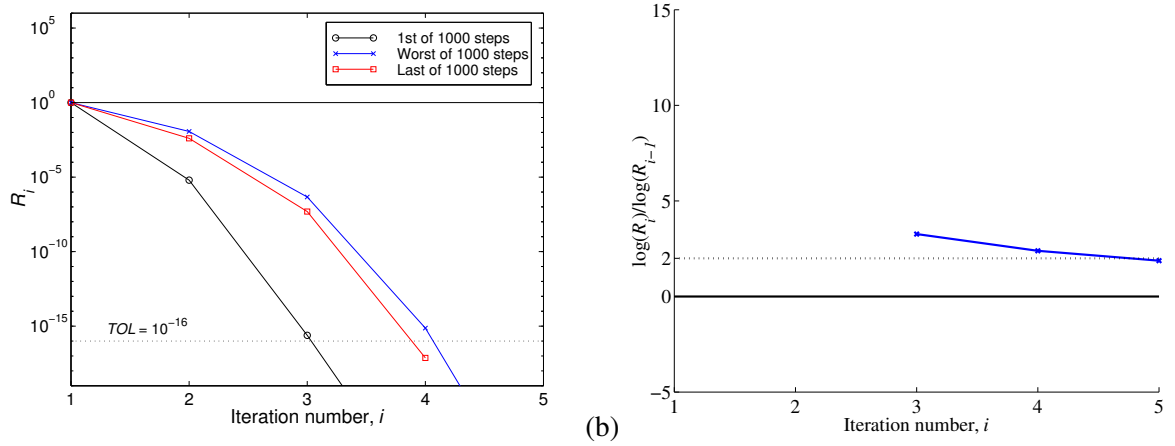

(a) (b)

Figure 4.8: Triaxial compression of heavily overconsolidated sample. Convergence profiles of (a) normalised residual, R_i, and (b) ratio of successive logarithms, $\log R_i$.

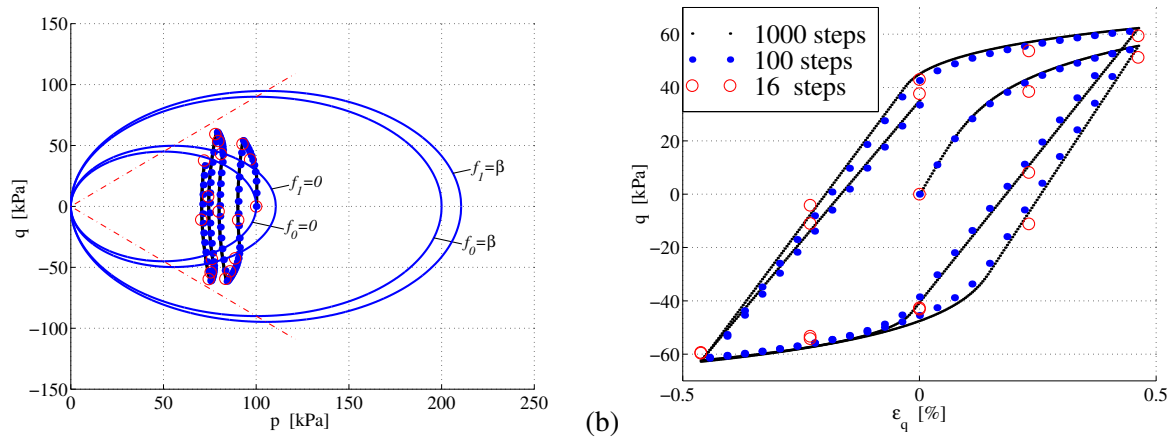

(a) (b)

Figure 4.9: Strain controlled cyclic shear test. (a) Stress path on p–q diagram, and (b) deviatoric stress, q vs. deviatoric strain, ε_q

4.5.5 Stress controlled cyclic shear loading

The stress-controlled analysis is presented for 1000, 100 and 16 time steps in Fig. 4.10. The hysteretic response shown here represents a slight improvement over the MCC model, with a decrease in pressure carried by the soil over successive cycles of shear loading. However, maximum deviatoric strain is constant over successive cycles, which is not representative of real soil response.

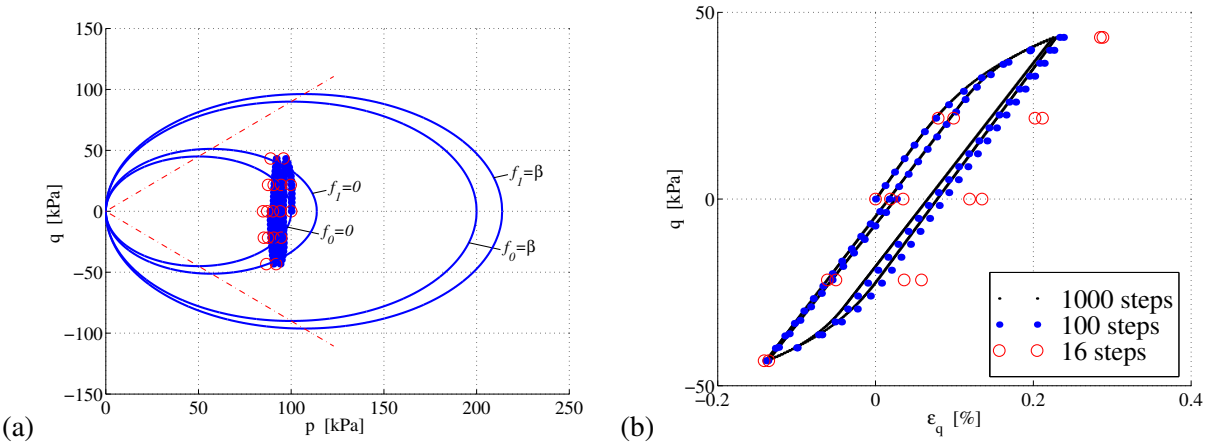

Figure 4.10: Stress controlled cyclic shear test. (a) Stress path on p–q diagram, and (b) deviatoric stress, q vs. deviatoric strain, ε_q

5. CONCLUSIONS

In this dissertation, three constitutive models have been presented for the modelling of cyclic soil plasticity. Each model was based upon the Modified Cam-Clay (MCC) yield criterion of Roscoe and Burland [1968], with different approaches taken for the modelling of inelastic behaviour.

Modified Cam-Clay Model

The first model considered was in the framework of classical plasticity, with a MCC yield condition, associative flow, a nonlinear hyperelastic stress–strain law, and nonlinear isotropic hardening. This model has been shown in the literature to model the monotonic behaviour of lightly overconsolidated and normally consolidated clays effectively. Furthermore, with the return mapping solution algorithm presented here, the model was robust and converged quadratically with relatively few time steps.

In cyclic loading histories, the MCC model was less effective at modelling real soil response. Cyclic shear loading tests under both stress and strain control were simulated here, while the volumetric strain was maintained at zero. Under cyclic strain-controlled loading with constant amplitude, the deviatoric stress component increased over successive cycles, as the size of the yield surface increased and the volumetric stress component decreased. With stress-controlled cyclic loading, only the first cycle resulted in yielding of the soil, and subsequent loading at the same amplitude was completely elastic. These results are not typical of the cyclic behaviour of real clays, which are dominated by degradation of stress capacity, and hysteretic response.

Anisotropic Bounding Surface Model

Because of the shortcomings in the MCC model for cyclic loading, several modifications to the original model have been proposed in the literature. One of these modifications is the widely used Bounding

Surface (BS) model, which was the second model considered in this dissertation. In particular, the Anisotropic BS model of Borja *et al.* [2001] was used, which involves a loading surface defined homologously to the bounding surface, and a combination of isotropic and kinematic hardening. An improved solution algorithm was presented here, with a reduction in the number of model dimensions in the plastic correction phase, and an explicit solution for the inelastic consistent tangent tensor, eliminating the requirement for matrix inversion.

The BS formulation resulted in a significant improvement in the modelling of soil response. In particular, the effective modelling of monotonic loading tests was maintained, while the two main shortcomings of the MCC model were rectified.

However, the BS model also suffered from several flaws which limit its applicability in engineering applications in its current form. Several problems related to the discrete relocation of the homology centre, and subsequent collapse of the loading surface were experienced. In summary:

- The discrete relocation of the homology centre on detection of the unloading condition results in sensitivity of model response to small perturbations in the loading history. This effect was particularly pronounced for low values of the model parameter, h.
- For cases where $(2\tilde{p} - p_l) < 0$, the model equations dictate that the loading surface must decrease in size. In some unloading histories, this is conceptually problematic. Computationally, the result of this problem was either a loss of convergence, or convergence to non-physical solutions.
- Several numerical examples presented by Borja *et al.* [2001] could be successfully recreated here. However, if relatively small modifications were made to model parameters or loading history, convergence problems developed. This suggests that the solution algorithm of Borja *et al.* [2001] may also experience the problems discussed here in more general application.

It was suggested here that a continuous evolution of the homology centre and back stress tensor may be a less problematic approach to describing the kinematic hardening of the model. However, to maintain the effectiveness of the Anisotropic BS approach, inelastic unloading should be incorporated, as this a particularly important feature of the model.

Generalised Plasticity Model

The final model considered in this dissertation was an adaption of the Generalised Plasticity (GP) framework of Auricchio *et al.* [1992] and Lubliner *et al.* [1993] to the MCC yield criterion. Several modifications to the original works were made, and several of the parameters of the model required redefinition.

The main attributes of the GP framework exploited here were a gradual transition from elastic to inelastic behaviour, and the onset of yielding at a stress level below the maximum previously reached. In these features, the GP framework is similar to the BS model discussed previously, but with the addition of a finite elastic region. However, in this first attempt to make use of the GP concepts for soil plasticity, only isotropic hardening was used, and unloading was elastic. If the results of the BS model were to be matched, inelastic unloading and kinematic hardening — discrete or continuous — would need to be added.

As presented, the GP model only slightly improved the modelling of cyclic response. In the strain-controlled cyclic loading test, the response was smoothed, but deviatoric stress levels continued to increase as the model converged to the critical state. The stress-controlled test exhibited some hysteretic behaviour, as some yielding was allowed to occur in each cycle, but not to the same extent as the BS model. Furthermore, deviatoric strain over successive cycles did not increase, a characteristic of real soil response.

Although some improvements were observed in the GP model, some conceptual and computational difficulties existed. In summary:

- In the original presentation of GP plasticity for a J2 yield function, a quadratic equation was solved analytically, and the correct root obtained by physical considerations. In this case, the plastic correction step of the return mapping was more complex, and it was not possible to determine the correct root. This led to convergence problems in the model, particularly when the stress state was near the critical state.
- Associative flow based on either the loading surface ($f = 0$) or limiting surface ($f = \beta$) did not result in an appropriate direction or magnitude of plastic flow. Because of this, the model converges to a critical state which does not lie on the critical state line.

These problems would need to be addressed in any future formulations of the GP model with MCC yield criterion. For the first problem, starting conditions other than the trial state could be investigated for the plastic correction stage of the return mapping. In particular, for stress states near critical the function h must remain positive, and the condition defined by (4.29) must be maintained.

For the second problem, associative flow should be defined based on the limit function, F. Differentiation of F could lead to some difficulties due to the inclusion of the consistency parameter in (4.5). If this is the case, a mapping of the current stress state onto either $f = 0$ or $f = \beta$ could be considered, although this approach may suggest that a bounding surface formulation is more appropriate.

A. CALCULATION OF RESIDUAL GRADIENT FOR CAM-CLAY MODEL

Calculation of $\frac{\partial g_1}{\partial \boldsymbol{x}}$

Differentiating $(2.23)_1$ with respect to the vector of unknowns gives:

$$\frac{\partial g_1}{\partial \boldsymbol{x}} = \frac{3}{M^2}\|\mathbf{s}\|\frac{\partial \|\mathbf{s}\|}{\partial \boldsymbol{x}} + \left\{ \begin{array}{c} 2p - p_c \\ -p \\ 0 \end{array} \right\} \tag{A.1}$$

where $\partial\|\mathbf{s}\|/\partial\boldsymbol{x}$ is obtained by differentiating (2.22):

$$\begin{aligned} \frac{\partial \|\mathbf{s}\|}{\partial \boldsymbol{x}} &= 2\alpha p_0 \left\|\mathbf{e}^{e,tr}\right\| A_2 . \frac{1}{A_4^2}\left[A_4\frac{\partial A_1}{\partial \boldsymbol{x}} - A_1\frac{\partial A_4}{\partial \boldsymbol{x}}\right] \\ &= \frac{\left\|\mathbf{s}^{tr}\right\|}{A_4^2}\left[\frac{A_1 A_4}{k}\left\{ \begin{array}{c} -2\Delta\gamma \\ \Delta\gamma \\ -(2p-p_c) \end{array} \right\} - \frac{A_1^2 A_3 \Delta\gamma}{k}\left\{ \begin{array}{c} -2\Delta\gamma \\ \Delta\gamma \\ -(2p-p_c) \end{array} \right\} - A_3 A_1^2 \left\{ \begin{array}{c} 0 \\ 0 \\ 1 \end{array} \right\}\right] \end{aligned} \tag{A.2}$$

Taking into account equations $(2.20)_4$ and (2.22) gives:

$$\frac{\partial \|\mathbf{s}\|}{\partial \boldsymbol{x}} = \frac{\|\mathbf{s}\|}{A_4}\left[\frac{1}{k}\left\{ \begin{array}{c} -2\Delta\gamma \\ \Delta\gamma \\ -(2p-p_c) \end{array} \right\} - A_1 A_3 \left\{ \begin{array}{c} 0 \\ 0 \\ 1 \end{array} \right\}\right] \tag{A.3}$$

It will be useful to define some vectors to simplify the above equations:

$$\boldsymbol{\Pi} = \left\{ \begin{array}{c} 2p - p_c \\ -p \\ 0 \end{array} \right\} \quad \boldsymbol{\Gamma} = \left\{ \begin{array}{c} -2\Delta\gamma \\ \Delta\gamma \\ -(2p-p_c) \end{array} \right\} \quad (\boldsymbol{\Delta}_I)_i = \left\{ \begin{array}{l} 1 \text{ if } i = I \\ 0 \text{ if } i \neq I \end{array} \right. \tag{A.4}$$

This leads to the simplified expression:

$$\frac{\partial g_1}{\partial \boldsymbol{x}} = \frac{3}{M^2}\frac{\|\mathbf{s}\|^2}{A_4}\left[\frac{1}{k}\boldsymbol{\Gamma} - A_1 A_3 \boldsymbol{\Delta}_3\right] + \boldsymbol{\Pi} \tag{A.5}$$

Calculation of $\frac{\partial g_2}{\partial \boldsymbol{x}}$

Differentiating $(2.23)_2$ with respect to the vector of unknowns gives:

$$\frac{\partial g_2}{\partial \boldsymbol{x}} = \frac{p_0 A_1 A_2}{k}\left[\frac{6\alpha}{M^2}\left(- \Delta\gamma\frac{\partial \mathbf{s} : \mathbf{e}^{e,tr}}{\partial \boldsymbol{x}} + \frac{3}{M^2}\Delta\gamma^2\|\mathbf{s}\|\frac{\partial\|\mathbf{s}\|}{\partial \boldsymbol{x}} + \left(\frac{3\Delta\gamma}{M^2}\|\mathbf{s}\|^2 - \mathbf{s} : \mathbf{e}^{e,tr}\right)\begin{Bmatrix} 0 \\ 0 \\ 1 \end{Bmatrix}\right) + A_6\begin{Bmatrix} -2\Delta\gamma \\ \Delta\gamma \\ -(2p - p_c) \end{Bmatrix}\right] - \begin{Bmatrix} 1 \\ 0 \\ 0 \end{Bmatrix} \tag{A.6}$$

Noting that $\mathbf{s} = 2\alpha p_0 A_2 A_5 \mathbf{e}^{e,tr}$ (from (2.16) and (2.22)) gives us:

$$\mathbf{s} : \mathbf{e}^{e,tr} = \frac{\|\mathbf{s}\|^2}{2\alpha p_0 A_2 A_5} \tag{A.7}$$

$$\frac{\partial \mathbf{s} : \mathbf{e}^{e,tr}}{\partial \boldsymbol{x}} = \frac{\|\mathbf{s}\|}{2\alpha p_0 A_2 A_5}\frac{\partial\|\mathbf{s}\|}{\partial \boldsymbol{x}} \tag{A.8}$$

We can then simplify (A.6) to:

$$\frac{\partial g_2}{\partial \boldsymbol{x}} = -\frac{3\|\mathbf{s}\|^2}{A_4 k M^2}\left(\frac{\Delta\gamma}{k}\boldsymbol{\Gamma} + \boldsymbol{\Delta}_3\right) + \frac{p_0 A_1 A_2 A_6}{k}\boldsymbol{\Gamma} - \boldsymbol{\Delta}_1 \tag{A.9}$$

Calculation of $\frac{\partial g_3}{\partial \boldsymbol{x}}$

Differentiating $(2.23)_3$ with respect to the vector of unknowns gives:

$$\begin{aligned}\frac{\partial g_3}{\partial \boldsymbol{x}} &= -\frac{p_{c0}}{\lambda - k}\exp\left(\frac{\theta_n^p}{\lambda - k}\right)\exp\left(\frac{\Delta\gamma(2p - p_c)}{\lambda - k}\right)\boldsymbol{\Gamma} - \boldsymbol{\Delta}_2 \\ &= -\frac{p_c}{\lambda - k}\boldsymbol{\Gamma} - \boldsymbol{\Delta}_2\end{aligned} \tag{A.10}$$

B. CALCULATION OF CONSISTENT TANGENT FOR CAM-CLAY MODEL

To obtain the inelastic consistent tangent tensor, each of the stress and hardening variables must be differentiated with respect to the trial elastic strain tensor, $\boldsymbol{\varepsilon}^{e,tr}$. Each of these equations can be solved for the derivative as a function of $\partial\Delta\gamma/\partial\boldsymbol{\varepsilon}^{e,tr}$. Finally, enforcing the consistency condition allows $\partial\Delta\gamma/\partial\boldsymbol{\varepsilon}^{e,tr}$ to be determined, and the tangent tensor evaluated.

Differentiate expression for p_c, Eq. (1.14):

$$\begin{aligned}\frac{\partial p_c}{\partial \boldsymbol{\varepsilon}^{e,tr}} &= \frac{p_{c0}}{\lambda-k}\exp\left(\frac{\theta_n^p}{\lambda-k}\right)\exp\left(\frac{\Delta\gamma(2p-p_c)}{\lambda-k}\right)\\ &\quad\left[(2p-p_c)\frac{\partial\Delta\gamma}{\partial\boldsymbol{\varepsilon}^{e,tr}}+2\Delta\gamma\frac{\partial p}{\partial\boldsymbol{\varepsilon}^{e,tr}}\right]\\ &= B_1\left[(2p-p_c)\frac{\partial\Delta\gamma}{\partial\boldsymbol{\varepsilon}^{e,tr}}+2\Delta\gamma\frac{\partial p}{\partial\boldsymbol{\varepsilon}^{e,tr}}\right]\end{aligned} \tag{B.1}$$

where

$$B_1 = \frac{p_c}{\lambda-k}\left[1+\frac{\Delta\gamma}{\lambda-k}p_c\right]^{-1} \tag{B.2}$$

To differentiate volumetric and deviatoric parts of stress, it will be useful to evaluate the derivatives of each of the constants defined in Section 2.4.2:

$$\frac{\partial A_1}{\partial \boldsymbol{\varepsilon}^{e,tr}} = -\frac{1}{k}A_1\left[(2p-p_c)\frac{\partial \Delta\gamma}{\partial \boldsymbol{\varepsilon}^{e,tr}} + \Delta\gamma\left(2\frac{\partial p}{\partial \boldsymbol{\varepsilon}^{e,tr}} - \frac{\partial p_c}{\partial \boldsymbol{\varepsilon}^{e,tr}}\right)\right] \tag{B.3}$$

$$\frac{\partial A_2}{\partial \boldsymbol{\varepsilon}^{e,tr}} = \frac{A_2}{k}\mathbf{1} \tag{B.4}$$

$$\frac{\partial A_3}{\partial \boldsymbol{\varepsilon}^{e,tr}} = \frac{A_3}{k}\mathbf{1} \tag{B.5}$$

$$\begin{aligned}\frac{\partial A_4}{\partial \boldsymbol{\varepsilon}^{e,tr}} &= \frac{A_1A_3\Delta\gamma}{k}\left[\mathbf{1} - (2p-p_c)\frac{\partial \Delta\gamma}{\partial \boldsymbol{\varepsilon}^{e,tr}} - \Delta\gamma\left(2\frac{\partial p}{\partial \boldsymbol{\varepsilon}^{e,tr}} - \frac{\partial p_c}{\partial \boldsymbol{\varepsilon}^{e,tr}}\right)\right] + A_1A_3\frac{\partial \Delta\gamma}{\partial \boldsymbol{\varepsilon}^{e,tr}} \\ &= B_2\mathbf{1} + B_3\frac{\partial \Delta\gamma}{\partial \boldsymbol{\varepsilon}^{e,tr}} - B_2\Delta\gamma\left(2\frac{\partial p}{\partial \boldsymbol{\varepsilon}^{e,tr}} - \frac{\partial p_c}{\partial \boldsymbol{\varepsilon}^{e,tr}}\right)\end{aligned} \tag{B.6}$$

$$\begin{aligned}\frac{\partial A_5}{\partial \boldsymbol{\varepsilon}^{e,tr}} &= -\frac{A_5}{k}\left[(2p-p_c)\frac{\partial \Delta\gamma}{\partial \boldsymbol{\varepsilon}^{e,tr}} - \Delta\gamma\left(2\frac{\partial p}{\partial \boldsymbol{\varepsilon}^{e,tr}} - \frac{\partial p_c}{\partial \boldsymbol{\varepsilon}^{e,tr}}\right)\right] \\ &\quad - \frac{A_5}{A_4^2}\left[B_2\mathbf{1} + B_3\frac{\partial \Delta\gamma}{\partial \boldsymbol{\varepsilon}^{e,tr}} - B_2\Delta\gamma\left(2\frac{\partial p}{\partial \boldsymbol{\varepsilon}^{e,tr}} - \frac{\partial p_c}{\partial \boldsymbol{\varepsilon}^{e,tr}}\right)\right] \\ &= A_5\left[B_4\frac{\partial \Delta\gamma}{\partial \boldsymbol{\varepsilon}^{e,tr}} + B_5\left(2\frac{\partial p}{\partial \boldsymbol{\varepsilon}^{e,tr}} - \frac{\partial p_c}{\partial \boldsymbol{\varepsilon}^{e,tr}}\right) - \frac{B_2}{A_4}\mathbf{1}\right]\end{aligned} \tag{B.7}$$

$$\begin{aligned}\frac{\partial A_6}{\partial \boldsymbol{\varepsilon}^{e,tr}} &= \frac{2\alpha}{k}\left[\mathbf{e}^{e,tr} - \frac{3\Delta\gamma}{M^2}\left(\mathbf{e}^{e,tr} : \frac{\partial \mathbf{s}}{\partial \boldsymbol{\varepsilon}^{e,tr}} + \mathbf{s}\right) - \frac{3}{M^2}\left(\mathbf{s} : \mathbf{e}^{e,tr}\right)\frac{\partial \Delta\gamma}{\partial \boldsymbol{\varepsilon}^{e,tr}}\right. \\ &\quad \left. + \left(\frac{3\Delta\gamma}{M^2}\right)^2 \mathbf{s} : \frac{\partial \mathbf{s}}{\partial \boldsymbol{\varepsilon}^{e,tr}} + \left(\frac{3}{M^2}\right)^2 \Delta\gamma\|\mathbf{s}\|^2 : \frac{\partial \Delta\gamma}{\partial \boldsymbol{\varepsilon}^{e,tr}}\right] \\ &= B_6\left(-\mathbf{s} + \frac{3\Delta\gamma}{M^2}\mathbf{s} : \frac{\partial \mathbf{s}}{\partial \boldsymbol{\varepsilon}^{e,tr}} + \frac{3}{M^2}\|\mathbf{s}\|^2\frac{\partial \Delta\gamma}{\partial \boldsymbol{\varepsilon}^{e,tr}}\right)\end{aligned} \tag{B.8, B.9}$$

where

$$\begin{cases} B_2 = \dfrac{A_1A_3\Delta\gamma}{k} \\ B_3 = -B_2(2p-p_c) + A_1A_3 \\ B_4 = -\left(\dfrac{1}{k}(2p-p_c) + \dfrac{B_3}{A_4}\right) \\ B_5 = -\Delta\gamma\left(\dfrac{1}{k} - \dfrac{B_2}{A_4}\right) \\ B_6 = \dfrac{1}{k}\left(2\alpha\left(\dfrac{3\Delta\gamma}{M^2}\right) - \dfrac{1}{p_0A_2A_5}\right) \end{cases} \tag{B.10}$$

Next, we differentiate $\mathbf{s}^{tr}$ and $\mathbf{s}$ from (2.16) and (2.22) respectively:

$$\frac{\partial \mathbf{s}^{tr}}{\partial \boldsymbol{\varepsilon}^{e,tr}} = 2\alpha p_0 A_2\left[\mathbb{I}_{\text{dev}} + \frac{1}{k}\mathbf{e}^{e,tr}\otimes\mathbf{1}\right] \tag{B.11}$$

$$\begin{aligned}\frac{\partial \mathbf{s}}{\partial \boldsymbol{\varepsilon}^{e,tr}} &= A_5\mathbf{s}^{tr}\otimes\left[B_4\frac{\partial \Delta\gamma}{\partial \boldsymbol{\varepsilon}^{e,tr}} + B_5\left(2\frac{\partial p}{\partial \boldsymbol{\varepsilon}^{e,tr}} - \frac{\partial p_c}{\partial \boldsymbol{\varepsilon}^{e,tr}}\right) - \frac{B_2}{A_4}\mathbf{1}\right] + 2\alpha p_0A_2A_5\mathbb{I}_{\text{dev}} + \frac{1}{k}\mathbf{s}\otimes\mathbf{1} \\ &= \mathbf{s}\otimes\left[B_4\frac{\partial \Delta\gamma}{\partial \boldsymbol{\varepsilon}^{e,tr}} + B_5\left(2\frac{\partial p}{\partial \boldsymbol{\varepsilon}^{e,tr}} - \frac{\partial p_c}{\partial \boldsymbol{\varepsilon}^{e,tr}}\right) + B_7\mathbf{1}\right] + 2\alpha p_0A_2A_5\mathbb{I}_{\text{dev}}\end{aligned} \tag{B.12}$$

where

$$B_7 = \frac{1}{k} - \frac{B_2}{A_4} \tag{B.13}$$

Substituting (B.1) into (B.12) gives:

$$\frac{\partial \mathbf{s}}{\partial \boldsymbol{\varepsilon}^{e,tr}} = \mathbf{s} \otimes \left[B_8 \frac{\partial \Delta\gamma}{\partial \boldsymbol{\varepsilon}^{e,tr}} + B_9 \frac{\partial p}{\partial \boldsymbol{\varepsilon}^{e,tr}} + B_7 \mathbf{1} \right] + 2\alpha p_0 A_2 A_5 \mathbb{I}_{\text{dev}} \tag{B.14}$$

where

$$\begin{cases} B_8 = B_4 - B_1 B_5 (2p - p_c) \\ B_9 = 2B_5 (1 - \Delta\gamma B_1) \end{cases} \tag{B.15}$$

Differentiate expression for p, (2.21) :

$$\begin{aligned} \frac{\partial p}{\partial \boldsymbol{\varepsilon}^{e,tr}} = p_0 A_1 A_2 \Bigg[B_6 \left\{ -\mathbf{s} + \frac{3\Delta\gamma}{M^2} \mathbf{s} : \frac{\partial \mathbf{s}}{\partial \boldsymbol{\varepsilon}^{e,tr}} + \frac{3}{M^2} \|\mathbf{s}\|^2 \frac{\partial \Delta\gamma}{\partial \boldsymbol{\varepsilon}^{e,tr}} \right\} \\ - \frac{A_6}{k} \left\{ (2p - p_c) \frac{\partial \Delta\gamma}{\partial \boldsymbol{\varepsilon}^{e,tr}} + \Delta\gamma \left(2 \frac{\partial p}{\partial \boldsymbol{\varepsilon}^{e,tr}} - \frac{\partial p_c}{\partial \boldsymbol{\varepsilon}^{e,tr}} - \mathbf{1} \right) \right\} \Bigg] \end{aligned} \tag{B.16}$$

Substitute for $\partial p_c / \partial \boldsymbol{\varepsilon}^{e,tr}$ from (B.1), and solve for $\partial p / \partial \boldsymbol{\varepsilon}^{e,tr}$:

$$\frac{\partial p}{\partial \boldsymbol{\varepsilon}^{e,tr}} = -C_2 \mathbf{s} + \left(\frac{3\Delta\gamma}{M^2} \right) C_2 \mathbf{s} : \frac{\partial \mathbf{s}}{\partial \boldsymbol{\varepsilon}^{e,tr}} + C_3 \frac{\partial \Delta\gamma}{\partial \boldsymbol{\varepsilon}^{e,tr}} + C_4 \mathbf{1} \tag{B.17}$$

(B.18)

where

$$\begin{cases} C_1 = \left[1 + 2\Delta\gamma \dfrac{p_0 A_1 A_2 A_6}{k} (1 - B_1 \Delta\gamma) \right]^{-1} \\ C_2 = p_0 A_1 A_2 B_6 C_1 \\ C_3 = C_2 \dfrac{3}{M^2} \|\mathbf{s}\|^2 + \dfrac{p_0 A_1 A_2 A_6 C_1}{k} (2p - p_c)(B_1 \Delta\gamma) \\ C_4 = \dfrac{p_0 A_1 A_2 A_6 C_1}{k} \end{cases} \tag{B.19}$$

Substitute (B.12) into (B.17), and solve for $\partial p / \partial \boldsymbol{\varepsilon}^{e,tr}$:

$$\frac{\partial p}{\partial \boldsymbol{\varepsilon}^{e,tr}} = C_5 \mathbf{s} + C_6 \frac{\partial \Delta\gamma}{\partial \boldsymbol{\varepsilon}^{e,tr}} + C_7 \mathbf{1} \tag{B.20}$$

(B.21)

where

$$\begin{cases} C_5 = -\dfrac{C_2}{A_4} \left[1 - \left(\dfrac{3\Delta\gamma}{M^2} \right) B_9 C_2 \|\mathbf{s}\|^2 \right]^{-1} \\ C_6 = \left(B_8 C_2 \|\mathbf{s}\|^2 \left(\dfrac{3\Delta\gamma}{M^2} \right) + C_3 \right) \left[1 - \left(\dfrac{3\Delta\gamma}{M^2} \right) B_9 C_2 \|\mathbf{s}\|^2 \right]^{-1} \\ C_7 = \left(B_7 C_2 \|\mathbf{s}\|^2 \left(\dfrac{3\Delta\gamma}{M^2} \right) + C_4 \right) \left[1 - \left(\dfrac{3\Delta\gamma}{M^2} \right) B_9 C_2 \|\mathbf{s}\|^2 \right]^{-1} \end{cases} \tag{B.22}$$

Differentiate the discrete form of the consistency condition:

$$f(\boldsymbol{\sigma}, p_c) = 0 \tag{B.23}$$

$$\mathrm{d}f(\boldsymbol{\sigma}, p_c) = \frac{\partial f}{\partial \boldsymbol{\sigma}} : \mathrm{d}\boldsymbol{\sigma} + \frac{\partial f}{\partial p_c} \mathrm{d}p_c = 0 \tag{B.24}$$

Differentiate (2.3) with respect to both $\boldsymbol{\sigma}$ and p_c:

$$\frac{\partial f}{\partial \boldsymbol{\sigma}} = \frac{3}{M^2}\mathbf{s} + \frac{1}{3}(2p - p_c)\mathbf{1} \tag{B.25}$$

$$\frac{\partial f}{\partial p_c} = -p \tag{B.26}$$

By definition, the total derivative of $\boldsymbol{\sigma}$ is given by:

$$\begin{aligned} \mathrm{d}\boldsymbol{\sigma} &= \frac{\partial \boldsymbol{\sigma}}{\partial \boldsymbol{\varepsilon}^{e,tr}} : \mathrm{d}\boldsymbol{\varepsilon}^{e,tr} \\ &= \left[\mathbf{1} \otimes \frac{\partial p}{\partial \boldsymbol{\varepsilon}^{e,tr}} + \frac{\partial \mathbf{s}}{\partial \boldsymbol{\varepsilon}^{e,tr}}\right] : \mathrm{d}\boldsymbol{\varepsilon}^{e,tr} \end{aligned} \tag{B.27}$$

and we can substitute from (B.20) and (B.14) into (B.27) to give:

$$\begin{aligned} \mathrm{d}\boldsymbol{\sigma} = \Bigg[& C_5\mathbf{1} \otimes \mathbf{s} + C_6\mathbf{1} \otimes \frac{\partial \Delta\gamma}{\partial \boldsymbol{\varepsilon}^{e,tr}} + C_7\mathbf{1} \otimes \mathbf{1} + (B_8 + B_9C_6)\mathbf{s} \otimes \frac{\partial \Delta\gamma}{\partial \boldsymbol{\varepsilon}^{e,tr}} \\ & + (B_7 + B_9C_7)\mathbf{s} \otimes \mathbf{1} + B_9C_5\mathbf{s} \otimes \mathbf{s} + 2\alpha p_0 A_2 A_5 \mathbb{I}_{\mathrm{dev}}\Bigg] : \mathrm{d}\boldsymbol{\varepsilon}^{e,tr} \end{aligned} \tag{B.28}$$

Similarly, the total derivative of p_c, substituting from (B.1) and (B.20), is given by:

$$\mathrm{d}p_c = B_1 \left[(2p - p_c + 2\Delta\gamma C_6)\frac{\partial \Delta\gamma}{\partial \boldsymbol{\varepsilon}^{e,tr}} + 2\Delta\gamma C_5\mathbf{s} + 2\Delta\gamma C_7\mathbf{1}\right] : \mathrm{d}\boldsymbol{\varepsilon}^{e,tr} \tag{B.29}$$

Consider both terms on the right hand side of (B.24) separately, substituting from (B.25), (B.26), (B.28) and (B.29):

$$\begin{aligned} \frac{\partial f}{\partial \boldsymbol{\sigma}} : \mathrm{d}\boldsymbol{\sigma} &= \Bigg[\frac{3}{M^2}\|\mathbf{s}\|^2 \left\{(B_8 + B_9C_6)\frac{\partial \Delta\gamma}{\partial \boldsymbol{\varepsilon}^{e,tr}} + (B_7 + B_9C_7)\mathbf{1} + B_9C_5\mathbf{s}\right\} \\ &\quad + A_5A_3\mathbf{s} + (2p - p_c)\left\{C_5\mathbf{s} + C_6\frac{\partial \Delta\gamma}{\partial \boldsymbol{\varepsilon}^{e,tr}} + C_7\mathbf{1}\right\}\Bigg] : \mathrm{d}\boldsymbol{\varepsilon}^{e,tr} \\ &= \left[D_1\frac{\partial \Delta\gamma}{\partial \boldsymbol{\varepsilon}^{e,tr}} + D_2\mathbf{1} + D_3\mathbf{s}\right] : \mathrm{d}\boldsymbol{\varepsilon}^{e,tr} \end{aligned} \tag{B.30}$$

$$\frac{\partial f}{\partial p_c}\mathrm{d}p_c = \left[D_4\frac{\partial \Delta\gamma}{\partial \boldsymbol{\varepsilon}^{e,tr}} + D_5\mathbf{1} + D_6\mathbf{s}\right] : \mathrm{d}\boldsymbol{\varepsilon}^{e,tr} \tag{B.31}$$

$$\tag{B.32}$$

where

$$\begin{cases} D_1 = \dfrac{3}{M^2}\|\mathbf{s}\|^2(B_8 + B_9C_6) + C_6(2p - p_c) \\ D_2 = \dfrac{3}{M^2}\|\mathbf{s}\|^2(B_7 + B_9C_7) + C_7(2p - p_c) \\ D_3 = \dfrac{3}{M^2}\|\mathbf{s}\|^2(B_9C_5) + C_5(2p - p_c) + A_5A_3 \\ D_4 = -pB_1(2p - p_c + 2\Delta\gamma C_6) \\ D_5 = -pB_1(2\Delta\gamma C_7) \\ D_6 = -pB_1(2\Delta\gamma C_5) \end{cases} \tag{B.33}$$

Combining (B.30) and (B.31) in (B.24), and solving for $\partial\Delta\gamma/\partial\boldsymbol{\epsilon}^{e,tr}$ gives:

$$\frac{\partial\Delta\gamma}{\partial\boldsymbol{\epsilon}^{e,tr}} = D_7\mathbf{s} + D_8\mathbf{1} \tag{B.34}$$

(B.35)

where

$$\begin{cases} D_7 = -\dfrac{D_3 + D_6}{D_1 + D_4} \\ D_8 = -\dfrac{D_2 + D_5}{D_1 + D_4} \end{cases} \tag{B.36}$$

Finally, substituting (B.1), (B.14), (B.20) and (B.34) into (2.30) gives:

$$\mathbb{C}^{\mathrm{p}} = E_1\mathbf{1}\otimes\mathbf{s} + E_2\mathbf{1}\otimes\mathbf{1} + E_3\mathbf{s}\otimes\mathbf{1} + E_4\mathbf{s}\otimes\mathbf{s} + E_5\mathbb{I}_{\mathrm{dev}} \tag{B.37}$$

(B.38)

where

$$\begin{cases} E_1 = C_5 + C_6D_7 \\ E_2 = C_7 + C_6D_8 \\ E_3 = (B_7 + B_9C_7) + (B_8 + B_9C_6)D_8 \\ E_4 = B_9C_5 + (B_8 + B_9C_6)D_7 \\ E_5 = 2\alpha p_0 A_2 A_5 \end{cases} \tag{B.39}$$

C. CALCULATION OF RESIDUAL GRADIENT FOR BOUNDING SURFACE MODEL

Define $\mathbf{\Pi}$, $\mathbf{\Gamma}$ and $\mathbf{\Delta}_I$ vectors, analogously with Appendix A:

$$\mathbf{\Pi} = \left\{ \begin{array}{c} 2\tilde{p} - p_l \\ -\tilde{p} \\ 0 \\ 0 \end{array} \right\} \quad \mathbf{\Gamma} = \left\{ \begin{array}{c} -2\Delta\gamma \\ \Delta\gamma \\ -(2\tilde{p} - p_l) \\ 0 \end{array} \right\} \quad (\mathbf{\Delta}_I)_i = \left\{ \begin{array}{l} 1 \text{ if } i = I \\ 0 \text{ if } i \neq I \end{array} \right. \tag{C.1}$$

Calculation of $\frac{\partial g_1}{\partial \boldsymbol{x}}$

Differentiating $(3.48)_1$ with respect to the vector of unknowns gives:

$$\frac{\partial g_1}{\partial \boldsymbol{x}} = \frac{3}{M^2}\tilde{\mathbf{s}} : \frac{\partial \tilde{\mathbf{s}}}{\partial \boldsymbol{x}} + \mathbf{\Pi} \tag{C.2}$$

The constants defined in (3.42) must be differentiated to evaluate $\partial\tilde{\mathbf{s}}/\partial\boldsymbol{x}$.

$$\frac{\partial A_1}{\partial \boldsymbol{x}} = \frac{A_1}{k}\mathbf{\Gamma} \tag{C.3}$$

$$\frac{\partial A_4}{\partial \boldsymbol{x}} = \frac{\Delta\gamma A_1 A_3}{k}\mathbf{\Gamma} + A_1 A_3 \mathbf{\Delta}_3 \tag{C.4}$$

$$\frac{\partial A_5}{\partial \boldsymbol{x}} = \frac{A_5}{A_4 k}\mathbf{\Gamma} - A_5^2 A_3 \mathbf{\Delta}_3 \tag{C.5}$$

$$\frac{\partial A_7}{\partial \boldsymbol{x}} = -\frac{1}{\lambda - k}\mathbf{\Gamma} \tag{C.6}$$

To differentiate $\boldsymbol{\alpha}$, we must make use of the earlier manipulation of $\boldsymbol{\sigma}_h$. Recalling (3.22) the derivative of $\boldsymbol{\sigma}_h$ is evaluated:

$$\begin{aligned} \frac{\partial \boldsymbol{\sigma}_h}{\partial \boldsymbol{x}} &= \frac{p_{cn}}{(1 - A_7)^2}\mathbf{\Sigma} \otimes \left(\frac{\partial A_7}{\partial \boldsymbol{x}} \right) \\ &= -\frac{p_c}{(\lambda - k)(1 - A_7)}\mathbf{\Sigma} \otimes \mathbf{\Gamma} \end{aligned} \tag{C.7}$$

where the last step follows from (C.6) and (3.45).

Now the derivative of $\boldsymbol{\alpha}$ can be evaluated, by differentiating (3.8):

$$\begin{aligned}\frac{\partial \boldsymbol{\alpha}}{\partial \boldsymbol{x}} &= \frac{\partial \boldsymbol{\sigma}_h}{\partial \boldsymbol{x}}\frac{\kappa}{1+\kappa} + \frac{1}{(1+\kappa)^2}\boldsymbol{\sigma}_h \otimes \boldsymbol{\Delta}_4 \\ &= \boldsymbol{\Sigma} \otimes \left[\frac{p_c}{(\lambda-k)(1-A_7)}\boldsymbol{\Gamma} + \frac{p_l}{(1+\kappa)}\boldsymbol{\Delta}_4\right]\end{aligned} \tag{C.8}$$

Note that the derivatives of $\boldsymbol{\alpha}^s$ and α^p can now be found from (C.8) by taking the deviatoric and volumetric parts of $\boldsymbol{\Sigma}$, respectively. These will be referred to as $\boldsymbol{\Sigma}_{\text{dev}}$ and Σ_{vol} in the following. The term in square brackets is unchanged.

The derivative of $\tilde{\mathbf{s}}$ is also required; differentiating equation (3.47) gives:

$$\begin{aligned}\frac{\partial \tilde{\mathbf{s}}}{\partial \boldsymbol{x}} &= \mathbf{s}^{tr} \otimes \frac{\partial A_5}{\partial \boldsymbol{x}} - \frac{1}{A_4^2}\left[A_4\frac{\partial \boldsymbol{\alpha}^s}{\partial \boldsymbol{x}} - \boldsymbol{\alpha}^s \otimes \frac{\partial A_4}{\partial \boldsymbol{x}}\right] \\ &= \left[\frac{\mathbf{s}}{A_5} - A_3\Delta\gamma\boldsymbol{\alpha}^s\right] \otimes \left[\frac{A_5}{kA_4}\boldsymbol{\Gamma} - A_3A_5^2\boldsymbol{\Delta}_3\right] \\ &- \frac{1}{A_4}\boldsymbol{\Sigma}_{\text{dev}} \otimes \left[-\frac{p_c}{(\lambda-k)(1-A_7)}\boldsymbol{\Gamma} + \frac{p_l}{1+\kappa}\boldsymbol{\Delta}_4\right] + \frac{A_1A_3\boldsymbol{\alpha}^s}{A_4^2} \otimes \left[\frac{\Delta\gamma}{k}\boldsymbol{\Gamma} + \boldsymbol{\Delta}_3\right]\end{aligned} \tag{C.9}$$

We substitute from (3.25), to give:

$$\frac{\partial \tilde{\mathbf{s}}}{\partial \boldsymbol{x}} = \left[\frac{1}{kA_4}\mathbf{s} + \frac{p_c}{A_4(\lambda-k)(1-A_7)}\boldsymbol{\Sigma}_{\text{dev}}\right] \otimes \boldsymbol{\Gamma} - A_3A_5\tilde{\mathbf{s}} \otimes \boldsymbol{\Delta}_3 - \frac{p_l}{A_4(1+\kappa)}\boldsymbol{\Sigma}_{\text{dev}} \otimes \boldsymbol{\Delta}_4 \tag{C.10}$$

By substituting (C.10) into (C.2), $\partial g_1/\partial \boldsymbol{x}$ can be determined.

Calculation of $\frac{\partial g_2}{\partial \boldsymbol{x}}$

Differentiating $(3.48)_2$ with respect to the vector of unknowns, $\boldsymbol{x}$, gives:

$$\begin{aligned}\frac{\partial g_2}{\partial \boldsymbol{x}} &= \left[\frac{p_0A_1A_2A_6}{k} + \frac{p_c}{\kappa p_l(\lambda-k)(1-A_7)}\Sigma_{\text{vol}}\right]\boldsymbol{\Gamma} - \frac{3}{kM^2}\mathbf{s} : \left[\Delta\gamma\frac{\partial \tilde{\mathbf{s}}}{\partial \boldsymbol{x}} + \tilde{\mathbf{s}} \otimes \boldsymbol{\Delta}_3\right] \\ &- \boldsymbol{\Delta}_1 - \frac{p_l}{\kappa(1+\kappa)}\Sigma_{\text{vol}}\boldsymbol{\Delta}_4\end{aligned} \tag{C.11}$$

Calculation of $\frac{\partial g_3}{\partial \boldsymbol{x}}$

Differentiating $(3.48)_3$ with respect to $\boldsymbol{x}$:

$$\begin{aligned}\frac{\partial g_3}{\partial \boldsymbol{x}} &= \frac{1}{(1-A_7)^2}\left[(1-A_7)\left(h\kappa^m\frac{\partial A_7}{\partial \boldsymbol{x}} + A_7hm\kappa^{m-1}\boldsymbol{\Delta}_4\right) + (p_{ln} + A_7h\kappa^m)\frac{\partial A_7}{\partial \boldsymbol{x}}\right] - \boldsymbol{\Delta}_2 \\ &= -\frac{1}{(1-A_7)(\lambda-k)}\left(h\kappa^m + p_l\right)\boldsymbol{\Gamma} - \boldsymbol{\Delta}_2 + \frac{A_7hm\kappa^{m-1}}{1-A_7}\boldsymbol{\Delta}_4\end{aligned} \tag{C.12}$$

Calculation of $\frac{\partial g_4}{\partial \boldsymbol{x}}$

Differentiating $(3.48)_4$ with respect to $\boldsymbol{x}$:

$$\frac{\partial g_4}{\partial \boldsymbol{x}} = \left\{ \begin{array}{c} 0 \\ 1+\kappa \\ 0 \\ p_l \end{array} \right\} + \frac{p_c}{(1-A_7)(\lambda - k)} \boldsymbol{\Gamma} \tag{C.13}$$

D. CALCULATION OF CONSISTENT TANGENT FOR BOUNDING SURFACE MODEL

Determination of the consistent tangent follows exactly the same procedure as for the MCC model, with one extra model unknown (additional parameters, κ and p_l, related to p_c through (3.9)).

First, it will be useful to obtain the derivative of A_7. From (3.42):

$$\frac{\partial A_7}{\partial \boldsymbol{\varepsilon}^{e,tr}} = \frac{1}{\lambda - k}\left[\frac{\partial \Delta\gamma}{\partial \boldsymbol{\varepsilon}^{e,tr}}(2\tilde{p} - p_l) + \Delta\gamma\left(2\frac{\partial \tilde{p}}{\partial \boldsymbol{\varepsilon}^{e,tr}} - \frac{\partial p_l}{\partial \boldsymbol{\varepsilon}^{e,tr}}\right)\right] \tag{D.1}$$

Two separate expressions can be obtained for the derivative of p_c. Differentiating (3.45), and using (D.1) gives:

$$\frac{\partial p_c}{\partial \boldsymbol{\varepsilon}^{e,tr}} = \frac{p_{cn}}{(1 - A_7)^2(\lambda - k)}\left[\frac{\partial \Delta\gamma}{\partial \boldsymbol{\varepsilon}^{e,tr}}(2\tilde{p} - p_l) + \Delta\gamma\left(2\frac{\partial \tilde{p}}{\partial \boldsymbol{\varepsilon}^{e,tr}} - \frac{\partial p_l}{\partial \boldsymbol{\varepsilon}^{e,tr}}\right)\right] \tag{D.2}$$

Differentiating (3.9) gives the second expression:

$$\frac{\partial p_c}{\partial \boldsymbol{\varepsilon}^{e,tr}} = (1 + \kappa)\frac{\partial p_l}{\partial \boldsymbol{\varepsilon}^{e,tr}} + p_l\frac{\partial \kappa}{\partial \boldsymbol{\varepsilon}^{e,tr}} \tag{D.3}$$

Equating (D.2) and (D.3), and solving for $\partial p_l / \partial \boldsymbol{\varepsilon}^{e,tr}$ gives:

$$\frac{\partial p_l}{\partial \boldsymbol{\varepsilon}^{e,tr}} = 2\Delta\gamma B_2\frac{\partial \tilde{p}}{\partial \boldsymbol{\varepsilon}^{e,tr}} + (2\tilde{p} - p_l)B_2\frac{\partial \Delta\gamma}{\partial \boldsymbol{\varepsilon}^{e,tr}} - p_l B_1\frac{\partial \kappa}{\partial \boldsymbol{\varepsilon}^{e,tr}} \tag{D.4}$$

where

$$\begin{cases} B_1 = \left[1 + \kappa + \dfrac{p_c\Delta\gamma}{(1 - A_7)(\lambda - k)}\right]^{-1} \\ B_2 = \dfrac{p_c}{(1 - A_7)(\lambda - k)}B_1 \end{cases} \tag{D.5}$$

We can also differentiate (3.46) directly to obtain a second expression for the derivative of p_l:

$$\begin{aligned} \frac{\partial p_l}{\partial \boldsymbol{\varepsilon}^{e,tr}} &= \frac{1}{(1 - A_7)^2}\left[h\,(1 - A_7)\left(A_7 m\kappa^{m-1}\frac{\partial \kappa}{\partial \boldsymbol{\varepsilon}^{e,tr}} + \kappa^m\frac{\partial A_7}{\partial \boldsymbol{\varepsilon}^{e,tr}}\right) + (p_{ln} + A_7 h\kappa^m)\frac{\partial A_7}{\partial \boldsymbol{\varepsilon}^{e,tr}}\right] \\ &= \frac{hm\kappa^{m-1}A_7}{1 - A_7}\frac{\partial \kappa}{\partial \boldsymbol{\varepsilon}^{e,tr}} + \frac{1}{1 - A_7}\left(h\kappa^m + p_l\right)\frac{\partial A_7}{\partial \boldsymbol{\varepsilon}^{e,tr}} \end{aligned} \tag{D.6}$$

Substituting from (D.1) into (D.6), and solving for $\partial p_l / \partial \boldsymbol{\varepsilon}^{e,tr}$ gives:

$$\frac{\partial p_l}{\partial \boldsymbol{\varepsilon}^{e,tr}} = B_4 \frac{\partial \kappa}{\partial \boldsymbol{\varepsilon}^{e,tr}} + B_5 \left[(2\tilde{p} - p_l) \frac{\partial \Delta\gamma}{\partial \boldsymbol{\varepsilon}^{e,tr}} + 2\Delta\gamma \frac{\partial \tilde{p}}{\partial \boldsymbol{\varepsilon}^{e,tr}} \right] \tag{D.7}$$

where

$$\begin{cases} B_3 = \left[1 + \dfrac{h\kappa^m + p_l}{(1 - A_7)(\lambda - k)} \Delta\gamma \right]^{-1} \\ B_4 = \left[\dfrac{hm\kappa^{m-1} A_7}{1 - A_7} \right] B_3 \\ B_5 = \left[\dfrac{h\kappa^m + p_l}{(1 - A_7)(\lambda - k)} \right] B_3 \end{cases} \tag{D.8}$$

Now the two expressions for $\partial p_l / \partial \boldsymbol{\varepsilon}^{e,tr}$, (D) and (D.7), can be equated, and solved for $\partial \kappa / \partial \boldsymbol{\varepsilon}^{e,tr}$:

$$\frac{\partial \kappa}{\partial \boldsymbol{\varepsilon}^{e,tr}} = B_6 \frac{\partial \tilde{p}}{\partial \boldsymbol{\varepsilon}^{e,tr}} + B_7 \frac{\partial \Delta\gamma}{\partial \boldsymbol{\varepsilon}^{e,tr}} \tag{D.9}$$

where

$$\begin{cases} B_6 = 2\Delta\gamma (B_2 - B_5)[B_4 + p_l B_1]^{-1} \\ B_7 = (2\tilde{p} - p_l)(B_2 - B_5)[B_4 + p_l B_1]^{-1} \end{cases} \tag{D.10}$$

We substitute (D.9) back into (D.7):

$$\frac{\partial p_l}{\partial \boldsymbol{\varepsilon}^{e,tr}} = B_8 \frac{\partial \tilde{p}}{\partial \boldsymbol{\varepsilon}^{e,tr}} + B_9 \frac{\partial \Delta\gamma}{\partial \boldsymbol{\varepsilon}^{e,tr}} \tag{D.11}$$

where

$$\begin{cases} B_8 = B_4 B_6 + 2\Delta\gamma B_5 \\ B_9 = B_4 B_7 + (2\tilde{p} - p_l) B_5 \end{cases} \tag{D.12}$$

We can now calculate the derivative of the back stress tensor, $\boldsymbol{\alpha}$, by differentiating (3.25), and substituting from (D.11) and (D.9) where necessary. This gives:

$$\frac{\partial \boldsymbol{\alpha}}{\partial \boldsymbol{\varepsilon}^{e,tr}} = \boldsymbol{\Sigma} \otimes \left[B_{10} \frac{\partial \tilde{p}}{\partial \boldsymbol{\varepsilon}^{e,tr}} + B_{11} \frac{\partial \Delta\gamma}{\partial \boldsymbol{\varepsilon}^{e,tr}} \right] \tag{D.13}$$

where

$$\begin{cases} B_{10} = \kappa B_8 + p_l B_6 \\ B_{11} = \kappa B_9 + p_l B_7 \end{cases} \tag{D.14}$$

To differentiate the deviatoric and volumetric stress components, it will first be necessary to obtain the

derivatives of A_1–A_6. Differentiating (3.42) gives the following expressions:

$$\frac{\partial A_1}{\partial \boldsymbol{\varepsilon}^{e,tr}} = C_1 \frac{\partial \tilde{p}}{\partial \boldsymbol{\varepsilon}^{e,tr}} + C_2 \frac{\partial \Delta\gamma}{\partial \boldsymbol{\varepsilon}^{e,tr}} \tag{D.15}$$

$$\frac{\partial A_2}{\partial \boldsymbol{\varepsilon}^{e,tr}} = \frac{A_2}{k}\mathbf{1} \tag{D.16}$$

$$\frac{\partial A_3}{\partial \boldsymbol{\varepsilon}^{e,tr}} = \frac{A_3}{k}\mathbf{1} \tag{D.17}$$

$$\frac{\partial A_4}{\partial \boldsymbol{\varepsilon}^{e,tr}} = C_3\mathbf{1} + C_4 \frac{\partial \tilde{p}}{\partial \boldsymbol{\varepsilon}^{e,tr}} + C_5 \frac{\partial \Delta\gamma}{\partial \boldsymbol{\varepsilon}^{e,tr}} \tag{D.18}$$

$$\frac{\partial A_5}{\partial \boldsymbol{\varepsilon}^{e,tr}} = C_6 \frac{\partial \tilde{p}}{\partial \boldsymbol{\varepsilon}^{e,tr}} + C_7 \frac{\partial \Delta\gamma}{\partial \boldsymbol{\varepsilon}^{e,tr}} + C_8\mathbf{1} \tag{D.19}$$

$$\begin{aligned}\frac{\partial A_6}{\partial \boldsymbol{\varepsilon}^{e,tr}} &= \frac{2\alpha}{k}\left(\mathbf{e}^{e,tr} - \frac{3\Delta\gamma}{M^2}\tilde{\mathbf{s}}\right) : \left[\mathbb{I}_{\text{dev}} - \frac{3}{M^2}\tilde{\mathbf{s}} \otimes \frac{\partial \Delta\gamma}{\partial \boldsymbol{\varepsilon}^{e,tr}} - \frac{3\Delta\gamma}{M^2}\frac{\partial \tilde{\mathbf{s}}}{\partial \boldsymbol{\varepsilon}^{e,tr}}\right] \\ &= \frac{1}{p_0 k A_1 A_2}\left[\mathbf{s} - \frac{3}{M^2}(\mathbf{s} : \tilde{\mathbf{s}})\frac{\partial \Delta\gamma}{\partial \boldsymbol{\varepsilon}^{e,tr}} - \frac{3\Delta\gamma}{M^2}\mathbf{s} : \frac{\partial \tilde{\mathbf{s}}}{\partial \boldsymbol{\varepsilon}^{e,tr}}\right]\end{aligned} \tag{D.20}$$

where

$$\begin{cases} C_1 = -\dfrac{A_1 \Delta\gamma}{k}(2 - B_8) \\ C_2 = -\dfrac{A_1}{k}\left[(2\tilde{p} - p_l) - \Delta\gamma B_9\right] \\ C_3 = \dfrac{A_1 A_3 \Delta\gamma}{k} \\ C_4 = C_1 A_3 \Delta\gamma \\ C_5 = A_1 A_3 + C_2 A_3 \Delta\gamma \\ C_6 = \dfrac{C_1}{A_4^2} \\ C_7 = \dfrac{1}{A_4^2}(C_2 - A_1^2 A_3) \\ C_8 = -\dfrac{A_1 C_3}{A_4^2} \end{cases} \tag{D.21}$$

Next, we differentiate $\mathbf{s}^{tr}$ and $\tilde{\mathbf{s}}$ from $(3.32)_4$ and (3.47) respectively:

$$\frac{\partial \mathbf{s}^{tr}}{\partial \boldsymbol{\varepsilon}^{e,tr}} = 2\alpha p_0 A_2 \mathbb{I}_{\text{dev}} + \frac{1}{k}\mathbf{s}^{tr} \otimes \mathbf{1} \tag{D.22}$$

$$\begin{aligned}\frac{\partial \tilde{\mathbf{s}}}{\partial \boldsymbol{\varepsilon}^{e,tr}} &= 2\alpha p_0 A_2 A_5 \mathbb{I}_{\text{dev}} + \frac{A_5}{k}\mathbf{s}^{tr} \otimes \mathbf{1} + \mathbf{s}^{tr} \otimes \left(C_6 \frac{\partial \tilde{p}}{\partial \boldsymbol{\varepsilon}^{e,tr}} + C_7 \frac{\partial \Delta\gamma}{\partial \boldsymbol{\varepsilon}^{e,tr}} + C_8\mathbf{1}\right) \\ &\quad - \frac{1}{A_4}\boldsymbol{\Sigma}_{\text{dev}} \otimes \left(B_{10}\frac{\partial \tilde{p}}{\partial \boldsymbol{\varepsilon}^{e,tr}} + B_{11}\frac{\partial \Delta\gamma}{\partial \boldsymbol{\varepsilon}^{e,tr}}\right) + \frac{\boldsymbol{\alpha}^s}{A_4^2} \otimes \left(C_3\mathbf{1} + C_4\frac{\partial \tilde{p}}{\partial \boldsymbol{\varepsilon}^{e,tr}} + C_5\frac{\partial \Delta\gamma}{\partial \boldsymbol{\varepsilon}^{e,tr}}\right)\end{aligned} \tag{D.23}$$

Substituting from (3.25) for $\boldsymbol{\alpha}^s$:

$$\frac{\partial \tilde{\mathbf{s}}}{\partial \boldsymbol{\varepsilon}^{e,tr}} = \frac{1}{kA_4}\mathbf{s} \otimes \mathbf{1} + (C_9\mathbf{s} + C_{10}\boldsymbol{\Sigma}_{\text{dev}}) \otimes \frac{\partial \tilde{p}}{\partial \boldsymbol{\varepsilon}^{e,tr}} + (C_{11}\mathbf{s} + C_{12}\boldsymbol{\Sigma}_{\text{dev}}) \otimes \frac{\partial \Delta\gamma}{\partial \boldsymbol{\varepsilon}^{e,tr}} + C_{13}\mathbb{I}_{\text{dev}} \tag{D.24}$$

where

$$\begin{cases} C_9 = \dfrac{C_1}{A_1 A_4} \\ C_{10} = -\dfrac{B_{10}}{A_4} \\ C_{11} = \dfrac{C_7}{A_5} \\ C_{12} = \dfrac{\kappa p_l A_1 A_3 - B_{11}}{A_4} \\ C_{13} = 2\alpha p_0 A_2 A_5 \end{cases} \tag{D.25}$$

We differentiate the volumetric part of (3.7) to obtain:

$$\begin{aligned} \frac{\partial \tilde{p}}{\partial \boldsymbol{\varepsilon}^{e,tr}} = p_0 A_2 A_6 \left(C_1 \frac{\partial \tilde{p}}{\partial \boldsymbol{\varepsilon}^{e,tr}} + C_2 \frac{\partial \Delta\gamma}{\partial \boldsymbol{\varepsilon}^{e,tr}} \right) + \frac{p_0 A_1 A_2 A_6}{k} \mathbf{1} + \frac{1}{k} \mathbf{s} \\ - \frac{3}{kM^2} (\mathbf{s} : \tilde{\mathbf{s}}) \frac{\partial \Delta\gamma}{\partial \boldsymbol{\varepsilon}^{e,tr}} - \frac{3\Delta\gamma}{kM^2} \mathbf{s} : \frac{\partial \tilde{\mathbf{s}}}{\partial \boldsymbol{\varepsilon}^{e,tr}} - \Sigma_{\text{vol}} \left(B_1 0 \frac{\partial \tilde{p}}{\partial \boldsymbol{\varepsilon}^{e,tr}} + B_1 1 \frac{\partial \Delta\gamma}{\partial \boldsymbol{\varepsilon}^{e,tr}} \right) \end{aligned} \tag{D.26}$$

Solving for $\partial \tilde{p} / \partial \boldsymbol{\varepsilon}^{e,tr}$ gives:

$$\frac{\partial \tilde{p}}{\partial \boldsymbol{\varepsilon}^{e,tr}} = \frac{D_1}{k} \mathbf{s} + D_2 \mathbf{1} - \frac{3\Delta\gamma}{D_1} kM^2 \mathbf{s} : \frac{\partial \tilde{\mathbf{s}}}{\partial \boldsymbol{\varepsilon}^{e,tr}} + D_3 \frac{\partial \Delta\gamma}{\partial \boldsymbol{\varepsilon}^{e,tr}} \tag{D.27}$$

where

$$\begin{cases} D_1 = [1 - p_0 A_2 A_6 C_1 + \Sigma_{\text{vol}} B_{10}]^{-1} \\ D_2 = \dfrac{p_0 A_1 A_2 A_6 D_1}{k} \\ D_3 = D_1 \left(p_0 A_2 A_6 C_2 - B_{11} \Sigma_{\text{vol}} - \dfrac{3}{kM^2} (\mathbf{s} : \tilde{\mathbf{s}}) \right) \end{cases} \tag{D.28}$$

We can substitute from (D.24) into (D.27), and solve for $\partial \tilde{p} / \partial \boldsymbol{\varepsilon}^{e,tr}$. This gives:

$$\frac{\partial \tilde{p}}{\partial \boldsymbol{\varepsilon}^{e,tr}} = D_5 \mathbf{1} + D_6 \mathbf{s} + D_7 \frac{\partial \Delta\gamma}{\partial \boldsymbol{\varepsilon}^{e,tr}} \tag{D.29}$$

where

$$\begin{cases} D_4 = \left[1 + D_1 \left(\dfrac{3\Delta\gamma}{kM^2} \right) \mathbf{s} : (C_9 \mathbf{s} + C_{10} \mathbf{s}_h) \right]^{-1} \\ D_5 = D_4 \left(D_2 - D_1 \left(\dfrac{3\Delta\gamma}{kM^2} \right) \dfrac{\|\mathbf{s}\|^2}{kA_4} \right) \\ D_6 = D_4 \left(\dfrac{D_1}{k} - D_1 \left(\dfrac{3\Delta\gamma}{kM^2} \right) C_{13} \right) = \dfrac{D_1 D_4}{A_4 k} \\ D_7 = D_4 \left(D_3 - D_1 \left(\dfrac{3\Delta\gamma}{kM^2} \right) \mathbf{s} : (C_{11} \mathbf{s} + C_{12} \mathbf{s}_h) \right) \end{cases} \tag{D.30}$$

As before, we obtain the discrete consistency condition by differentiating the yield function:

$$f(\tilde{\boldsymbol{\sigma}}, p_l) = 0 \tag{D.31}$$

$$\mathrm{d}f(\tilde{\boldsymbol{\sigma}}, p_l) = \frac{\partial f}{\partial \tilde{\boldsymbol{\sigma}}} : \mathrm{d}\tilde{\boldsymbol{\sigma}} + \frac{\partial f}{\partial p_l} \mathrm{d}p_l = 0 \tag{D.32}$$

Differentiate (3.6) with respect to both $\tilde{\boldsymbol{\sigma}}$ and p_l:

$$\frac{\partial f}{\partial \tilde{\boldsymbol{\sigma}}} = \frac{3}{M^2}\tilde{\mathbf{s}} + \frac{1}{3}(2\tilde{p} - p_l)\mathbf{1} \tag{D.33}$$

$$\frac{\partial f}{\partial p_l} = -\tilde{p} \tag{D.34}$$

As with the CC model, the total derivative of $\tilde{\boldsymbol{\sigma}}$ is given by:

$$\mathrm{d}\tilde{\boldsymbol{\sigma}} = \left[\mathbf{1} \otimes \frac{\partial \tilde{p}}{\partial \boldsymbol{\varepsilon}^{e,tr}} + \frac{\partial \tilde{\mathbf{s}}}{\partial \boldsymbol{\varepsilon}^{e,tr}}\right] : \mathrm{d}\boldsymbol{\varepsilon}^{e,tr} \tag{D.35}$$

and substituting from (D.29) and (D.24) into (D.35) gives:

$$\begin{aligned}\mathrm{d}\tilde{\boldsymbol{\sigma}} = \Bigg[& C_{13} + (D_5\mathbf{1} + E_1\mathbf{s} + E_2\boldsymbol{\Sigma}_{\text{dev}}) \otimes \mathbf{1} + (D_6\mathbf{1} + E_3\mathbf{s} + E_4\boldsymbol{\Sigma}_{\text{dev}}) \otimes \mathbf{s} \\ & + (D_7\mathbf{1} + E_5\mathbf{s} + E_6\boldsymbol{\Sigma}_{\text{dev}}) \otimes \frac{\partial \Delta\gamma}{\partial \boldsymbol{\varepsilon}^{e,tr}}\Bigg] : \mathrm{d}\boldsymbol{\varepsilon}^{e,tr}\end{aligned} \tag{D.36}$$

Similarly, the total derivative of p_l is given by:

$$\mathrm{d}p_l = \frac{\partial p_l}{\partial \boldsymbol{\varepsilon}^{e,tr}} : \mathrm{d}\boldsymbol{\varepsilon}^{e,tr}$$

and substituting from (D.7) and (D.29), we obtain:

$$\mathrm{d}p_l = \left[D_5B_8\mathbf{1} + D_6B_8\mathbf{s} + E_7\frac{\partial \Delta\gamma}{\partial \boldsymbol{\varepsilon}^{e,tr}}\right] : \mathrm{d}\boldsymbol{\varepsilon}^{e,tr} \tag{D.38}$$

where

$$E_7 = B_9 + B_8D_7 \tag{D.39}$$

Considering both terms on the right hand side of (D.32) separately, we substitute from (D.33), (D.34), (D.36) and (D.38), giving:

$$\begin{aligned}\frac{\partial f}{\partial \tilde{\boldsymbol{\sigma}}} : \mathrm{d}\tilde{\boldsymbol{\sigma}} = \Bigg[& A_3A_5\tilde{\mathbf{s}} + \left(\frac{3}{M^2}\right)\tilde{\mathbf{s}} : \left(E_1\mathbf{s} \otimes \mathbf{1} + E_3\mathbf{s} \otimes \mathbf{s} + E_5\mathbf{s} \otimes \frac{\partial \Delta\gamma}{\partial \boldsymbol{\varepsilon}^{e,tr}}\right) \\ & + \left(\frac{3}{M^2}\right)\tilde{\mathbf{s}} : \left(E_2\boldsymbol{\Sigma}_{\text{dev}} \otimes \mathbf{1} + E_4\boldsymbol{\Sigma}_{\text{dev}} \otimes \mathbf{s} + E_6\boldsymbol{\Sigma}_{\text{dev}} \otimes \frac{\partial \Delta\gamma}{\partial \boldsymbol{\varepsilon}^{e,tr}}\right) \\ & + (2\tilde{p} - p_l)\left(D_5\mathbf{1} + D_6\mathbf{s} + D_7\frac{\partial \Delta\gamma}{\partial \boldsymbol{\varepsilon}^{e,tr}}\right)\Bigg] : \mathrm{d}\boldsymbol{\varepsilon}^{e,tr} \\ = & \left[A_3A_5\tilde{\mathbf{s}} + F_1\mathbf{1} + F_2\mathbf{s} + F_3\frac{\partial \Delta\gamma}{\partial \boldsymbol{\varepsilon}^{e,tr}}\right] : \mathrm{d}\boldsymbol{\varepsilon}^{e,tr}\end{aligned} \tag{D.40}$$

for the first term, and

$$\frac{\partial f}{\partial p_l}\,\mathrm{d}p_l = -\tilde{p}\left[D_5B_8\mathbf{1} + D_6B_8\mathbf{s} + E_7\frac{\partial \Delta\gamma}{\partial \boldsymbol{\varepsilon}^{e,tr}}\right] : \mathrm{d}\boldsymbol{\varepsilon}^{e,tr} \tag{D.41}$$

for the second term, where:

$$\begin{cases} F_1 = (2\tilde{p} - p_l)D_5 + \left(\dfrac{3}{M^2}\right)\tilde{\mathbf{s}} : (E_1\mathbf{s} + E_2\boldsymbol{\Sigma}_{\text{dev}}) \\ F_2 = (2\tilde{p} - p_l)D_6 + \left(\dfrac{3}{M^2}\right)\tilde{\mathbf{s}} : (E_3\mathbf{s} + E_4\boldsymbol{\Sigma}_{\text{dev}}) \\ F_3 = (2\tilde{p} - p_l)D_7 + \left(\dfrac{3}{M^2}\right)\tilde{\mathbf{s}} : (E_5\mathbf{s} + E_6\boldsymbol{\Sigma}_{\text{dev}}) \\ F_4 = [E_7\tilde{p} - F_3]^{-1} \end{cases} \tag{D.42}$$

Combining (D.40) and (D.41) in (D.32), and solving for $\partial\Delta\gamma/\partial\boldsymbol{\varepsilon}^{e,tr}$ gives:

$$\frac{\partial\Delta\gamma}{\partial\boldsymbol{\varepsilon}^{e,tr}} = F_5\mathbf{1} + F_6\mathbf{s} + F_7\boldsymbol{\Sigma}_{\text{dev}} \tag{D.43}$$

where

$$\begin{cases} F_5 = F_4(F_1 - D_5B_8\tilde{p} \\ F_6 = F_4(F_2 - D_6B_8\tilde{p} + A_3A_5 \\ F_7 = -A_3A_5F_4\kappa p_l \end{cases} \tag{D.44}$$

This expression is substituted into (D.29) and (D.24), giving:

$$\frac{\partial\tilde{p}}{\partial\boldsymbol{\varepsilon}^{e,tr}} = G_1\mathbf{1} + G_2\mathbf{s} + D_7F_7\boldsymbol{\Sigma}_{\text{dev}} \tag{D.45}$$

and

$$\frac{\partial\tilde{\mathbf{s}}}{\partial\boldsymbol{\varepsilon}^{e,tr}} = C_{13}\mathbb{I}_{\text{dev}} + (G_3\mathbf{s} + G_4\boldsymbol{\Sigma}_{\text{dev}}) \otimes \mathbf{1} + (G_5\mathbf{s} + G_6\boldsymbol{\Sigma}_{\text{dev}}) \otimes \mathbf{s} + (G_7\mathbf{s} + G_8\boldsymbol{\Sigma}_{\text{dev}}] \otimes \boldsymbol{\Sigma}_{\text{dev}} \tag{D.46}$$

where

$$\begin{cases} G_1 = D_5 + D_7F_5 \\ G_2 = D_6 + D_7F_6 \\ G_3 = E_1 + E_5F_5 \\ G_4 = E_2 + E_6F_5 \\ G_5 = E_3 + E_5F_6 \\ G_6 = E_4 + E_6F_6 \\ G_7 = E_5F_7 \\ G_8 = E_6F_7 \end{cases} \tag{D.47}$$

We now have the derivatives of $\tilde{p}$ and $\tilde{\mathbf{s}}$, in (D.45) and (D.46) respectively, but we must convert to derivatives of $\mathbf{s}$ and p before the consistent tangent can be calculated. Differentiating the volumetric and deviatoric parts of (3.7) gives the following expressions:

$$\begin{aligned} \frac{\partial p}{\partial\boldsymbol{\varepsilon}^{e,tr}} &= \frac{\partial\tilde{p}}{\partial\boldsymbol{\varepsilon}^{e,tr}} + \frac{\partial\alpha^p}{\partial\boldsymbol{\varepsilon}^{e,tr}} \\ &= H_1\mathbf{1} + H_2\mathbf{s} + H_3\boldsymbol{\Sigma}_{\text{dev}} \end{aligned} \tag{D.48}$$

$$\tag{D.49}$$

and

$$\begin{aligned}\frac{\partial \mathbf{s}}{\partial \boldsymbol{\varepsilon}^{e,tr}} &= \frac{\partial \tilde{\mathbf{s}}}{\partial \boldsymbol{\varepsilon}^{e,tr}} + \frac{\partial \boldsymbol{\alpha}^{s}}{\partial \boldsymbol{\varepsilon}^{e,tr}} \\ &= C_{13}\mathbb{I}_{\text{dev}} + (G_3\mathbf{s} + H_4\boldsymbol{\Sigma}_{\text{dev}}) \otimes \mathbf{1} + (G_5\mathbf{s} + H_5\boldsymbol{\Sigma}_{\text{dev}}) \otimes \mathbf{s} + (G_7\mathbf{s} + H_6\boldsymbol{\Sigma}_{\text{dev}}) \otimes \boldsymbol{\Sigma}_{\text{dev}}\end{aligned} \tag{D.50}$$

where

$$\begin{cases} H_1 = (1 + B_{10}\Sigma_{\text{vol}})G_1 + B_{11}F_5\Sigma_{\text{vol}} \\ H_2 = (1 + B_{10}\Sigma_{\text{vol}})G_2 + B_{11}F_6\Sigma_{\text{vol}} \\ H_3 = (1 + B_{10}\Sigma_{\text{vol}})D_7F_7 + B_{11}F_7\Sigma_{\text{vol}} \\ H_4 = G_4 + B_{10}G_1 + B_{11}F_5 \\ H_5 = G_6 + B_{10}G_2 + B_{11}F_6 \\ H_6 = G_8 + B_{10}D_7F_7 + B_{11}F_7 \end{cases} \tag{D.51}$$

Finally, we recall the expression for the consistent tangent from Chapter 2, (2.30). Substituting for $\partial p/\partial \boldsymbol{\varepsilon}^{e,tr}$ and $\partial \mathbf{s}/\partial \boldsymbol{\varepsilon}^{e,tr}$ from (D.48) and (D.50) respectively, we obtain the final expression:

$$\begin{aligned}\mathbb{C}^{\text{p}} = &(H_1\mathbf{1} + G_3\mathbf{s} + H_4\boldsymbol{\Sigma}_{\text{dev}}) \otimes \mathbf{1} + (H_2\mathbf{1} + G_5\mathbf{s} + H_5\boldsymbol{\Sigma}_{\text{dev}}) \otimes \mathbf{s} \\ &+ (H_3\mathbf{1} + G_7\mathbf{s} + H_6\boldsymbol{\Sigma}_{\text{dev}}) \otimes \boldsymbol{\Sigma}_{\text{dev}} + C_{13}\mathbb{I}_{\text{dev}}\end{aligned} \tag{D.52}$$

E. CALCULATION OF RESIDUAL GRADIENT FOR GENERALISED PLASTICITY MODEL

As noted in the text, g_2 and g_3 for the GP model are identical to their MCC counterparts. Refer to Appendix A for the calculation of $\partial g_2/\partial \boldsymbol{x}$ and $\partial g_3/\partial \boldsymbol{x}$.

Calculation of $\frac{\partial g_1}{\partial \boldsymbol{x}}$

The yield function, f, used here is also identical to that used in the MCC model, so from (A.5), we have:

$$\frac{\partial f}{\partial \boldsymbol{x}} = \frac{3}{M^2}\frac{\|\mathbf{s}\|^2}{A_4}\left[\frac{1}{k}\boldsymbol{\Gamma} - A_1 A_3 \boldsymbol{\Delta}_3\right] + \boldsymbol{\Pi} \tag{E.1}$$

The derivative of $\hat{f}$ with respect to $\boldsymbol{x}$ can be obtained directly from (E.1), by removing the dependence of f on p_c, and replacing p_c with p_{cn}. Therefore, setting the second component of $\partial \hat{f}/\partial \boldsymbol{x}$ to zero, we obtain:

$$\frac{\partial \hat{f}}{\partial \boldsymbol{x}} = \frac{3}{M^2}\frac{\|\mathbf{s}\|^2}{A_4}\left[\frac{1}{k}\hat{\boldsymbol{\Gamma}} - A_1 A_3 \boldsymbol{\Delta}_3\right] + (2p - p_{cn})\boldsymbol{\Delta}_1 \tag{E.2}$$

where

$$\hat{\boldsymbol{\Gamma}} = \left\{ \begin{array}{c} -2\Delta\gamma \\ 0 \\ -(2p - p_{cn}) \end{array} \right\} \tag{E.3}$$

and the $\boldsymbol{\Delta}_1$ term has been obtained by setting the second component of $\boldsymbol{\Pi}$ to zero.

Differentiating (4.6) gives:

$$\frac{\partial h}{\partial \boldsymbol{x}} = \frac{1}{(\delta(\beta - f) + H\beta)^2}\left[(\delta(\beta - f) + H\beta)\frac{\partial f}{\partial \boldsymbol{x}} - f\left(-\delta\frac{\partial f}{\partial \boldsymbol{x}} + (\delta + H)\frac{\partial \beta}{\partial \boldsymbol{x}} + \beta\frac{\partial H}{\partial \boldsymbol{x}}\right)\right] \tag{E.4}$$

which can be simplified by recalling the definition of h in (4.6), giving the following expression:

$$\frac{\partial h}{\partial \boldsymbol{x}} = \frac{1}{\delta(\beta - f) + H\beta}\left\{\frac{\partial f}{\partial \boldsymbol{x}}(1 + h\delta) - h\left((\delta + H)\frac{\partial \beta}{\partial \boldsymbol{x}} + \beta\frac{\partial H}{\partial \boldsymbol{x}}\right)\right\} \tag{E.5}$$

The derivatives in (E.5) are obtained by differentiating (4.8) and (4.7):

$$\frac{\partial H}{\partial \boldsymbol{x}} = \frac{1}{\lambda - k} \left\{ \begin{array}{c} p_c(4p - p_c) \\ 2p(p - p_c) \\ 0 \end{array} \right\}; \qquad \frac{\partial \beta}{\partial \boldsymbol{x}} = \beta_1 \boldsymbol{\Delta}_1 \tag{E.6}$$

Finally, we can differentiate g_1 directly, from $(4.30)_1$, giving:

$$\frac{\partial g_1}{\partial \boldsymbol{x}} = \frac{\partial h}{\partial \boldsymbol{x}}(\hat{f} - \hat{f}_n) + h \left(\frac{\partial \hat{f}}{\partial \boldsymbol{x}} \right) - \boldsymbol{\Delta}_3 \tag{E.7}$$

By substituting from (E.1), (E.2) and (E.5), $\partial g_1 / \partial \boldsymbol{x}$ can be found.

F. CALCULATION OF CONSISTENT TANGENT FOR GENERALISED PLASTICITY MODEL

Derivatives of p_c, $\mathbf{s}$ and p are the same as those evaluated in Appendix B, and can be obtained from equations (B.1), (B.14) and (B.20), respectively. In this case, however, the consistency condition is enforced on the limit equation:

$$F_{disc}(\boldsymbol{\sigma}, p_c, \Delta\gamma) = 0 \tag{F.1}$$

Differentiating this gives:

$$\mathrm{d}F_{disc}(\boldsymbol{\sigma}, p_c, \Delta\gamma) = \frac{\partial F}{\partial \boldsymbol{\sigma}} : \mathrm{d}\boldsymbol{\sigma} + \frac{\partial F}{\partial p_c}\mathrm{d}p_c + \frac{\partial F}{\partial \Delta\gamma}\mathrm{d}\Delta\gamma \tag{F.2}$$

Given that $\partial f/\partial\boldsymbol{\sigma}$ and $\partial f/\partial p_c$ are the same as before, and $\partial f/\partial\Delta\gamma = 0$, we can differentiate (4.30) with respect to each of the variables. In contrast to the MCC and BS models, (F.2) also involves derivatives with respect to $\Delta\gamma$, and derivatives of $\boldsymbol{\sigma}$ and p_c are now evaluated keeping $\Delta\gamma$ constant. These derivatives are identical to those used in calculation of the residual gradient in Appendix E, except that only the volumetric part of the stress, p, was included in the vector of unknowns, $\boldsymbol{x}$. However, considering that:

$$\frac{\partial H}{\partial \mathbf{s}} = \mathbf{0}\,, \qquad \frac{\partial \beta}{\partial \mathbf{s}} = 0 \tag{F.3}$$

and

$$\frac{\partial p}{\partial \boldsymbol{\sigma}} = \frac{1}{3}\mathbf{1}, \tag{F.4}$$

Equation (E.5) can be used for the partial derivative of h with respect to $\boldsymbol{\sigma}$. This gives:

$$\begin{aligned}\frac{\partial h}{\partial \boldsymbol{\sigma}} &= \frac{1}{\delta(\beta - f) + H\beta}\left\{(1+h\delta)\frac{\partial f}{\partial \boldsymbol{\sigma}} - \frac{1}{3}h\beta_1\left[(H+\delta) + p\frac{\partial H}{\partial p}\right]\mathbf{1}\right\} \\ &= H_1\frac{\partial f}{\partial \boldsymbol{\sigma}} + \frac{1}{3}H_2\mathbf{1}\end{aligned} \tag{F.5}$$

where

$$\begin{cases} H_1 = \dfrac{1+h\delta}{\delta(\beta - f) + H\beta} \\ H_2 = \dfrac{-h\beta_1}{\delta(\beta - f) + H\beta}\left[(H+\delta] + p\dfrac{\partial H}{\partial p}\right] \end{cases} \tag{F.6}$$

Similarly, the partial derivative with respect to p_c can also be obtained from (E.5):

$$\begin{aligned}\frac{\partial h}{\partial p_c} &= \frac{1}{\delta(\beta - f) + H\beta}\left\{(1 + h\delta)\frac{\partial f}{\partial p_c} - h\beta\frac{\partial H}{\partial p_c}\right\} \\ &= H_1\frac{\partial f}{\partial p_c} + H_3\end{aligned} \tag{F.7}$$

where

$$H_3 = \frac{-h\beta}{\delta(\beta - f) + H\beta}\frac{\partial H}{\partial p_c} \tag{F.8}$$

Finally, the partial derivative of h with respect to $\Delta\gamma$ is evaluated:

$$\frac{\partial h}{\partial \Delta\gamma} = 0 \tag{F.9}$$

Note that the third component of (E.5), also representing the derivative of h with respect to $\Delta\gamma$, was non-zero. This apparent inconsistency arises due to the different variables held fixed in the evaluation of each partial derivative. In the $\Delta\gamma$–component of (E.5), p and p_c are held constant, while $\mathbf{s}$ is allowed to vary. The derivative in (F.9), however, has been evaluated keeping both volumetric and deviatoric parts of the stress tensor fixed.

Equations (F.5)–(F.7) allow the calculation of the partial derivatives of F. Differentiating with respect to $\boldsymbol{\sigma}$ gives:

$$\frac{\partial F}{\partial \boldsymbol{\sigma}} = \frac{\partial h}{\partial \boldsymbol{\sigma}}(\hat{f} - \hat{f}_n) + h\frac{\partial \hat{f}}{\partial \boldsymbol{\sigma}} \tag{F.10}$$

Recalling the expression for $\hat{f}$, $(4.22)_2$, we can obtain the derivative with respect to $\boldsymbol{\sigma}$.

$$\frac{\partial \hat{f}}{\partial \boldsymbol{\sigma}} = \frac{3}{M^2}\mathbf{s} + \frac{1}{3}(2p - p_{cn})\mathbf{1} = \frac{\partial f}{\partial \boldsymbol{\sigma}} + \frac{1}{3}(p_c - p_{cn})\mathbf{1} \tag{F.11}$$

Substituting from (F.5) and (F.11) into (F.10) gives:

$$\frac{\partial F}{\partial \boldsymbol{\sigma}} = H_4\frac{\partial f}{\partial \boldsymbol{\sigma}} + \frac{1}{3}H_5\mathbf{1} \tag{F.12}$$

where

$$\begin{cases} H_4 = (\hat{f} - \hat{f}_n)H_1 + h \\ H_5 = (\hat{f} - \hat{f}_n)H_2 + h(p_c - p_{cn}) \end{cases} \tag{F.13}$$

Similarly, $\partial F/\partial p_c$ can be expressed as:

$$\frac{\partial F}{\partial p_c} = H_6\frac{\partial f}{\partial p_c} + H_7 \tag{F.14}$$

where

$$\begin{cases} H_6 = (\hat{f} - \hat{f}_n)H_1 \\ H_7 = (\hat{f} - \hat{f}_n)H_3 \end{cases} \tag{F.15}$$

Finally, the partial derivative of F with respect to $\Delta\gamma$ follows simply from (4.5):

$$\frac{\partial F}{\partial \Delta\gamma} = -1 \tag{F.16}$$

To substitute into (F.2), the total derivatives must also be evaluated. Only $\mathrm{d}\Delta\gamma$ has changed from Appendix B, and is given by:

$$\mathrm{d}\Delta\gamma = \frac{\partial \Delta\gamma}{\partial \boldsymbol{\varepsilon}^{e,tr}} : \mathrm{d}\boldsymbol{\varepsilon}^{e,tr} \tag{F.17}$$

Substituting the above expressions into (F.2) gives:

$$\frac{\partial \Delta\gamma}{\partial \boldsymbol{\varepsilon}^{e,tr}} = \hat{D}_7 \mathbf{s} + \hat{D}_8 \mathbf{1} \tag{F.18}$$

with

$$\begin{cases} \hat{D}_7 = \hat{D}_9 \left[D_3 H_4 + C_5 H_5 + D_6 H_6 + 2\Delta\gamma B_1 C_5 H_7 \right] \\ \hat{D}_8 = \hat{D}_9 \left[D_2 H_4 + C_7 H_5 + D_5 H_6 + 2\Delta\gamma B_1 C_7 H_7 \right] \\ \hat{D}_9 = \left[1 - D_1 H_4 - C_6 H_5 - D_4 H_6 - B_1 H_7 (2p - p_c + 2\Delta\gamma C_6) \right]^{-1} \end{cases} \tag{F.19}$$

where the constants terms B_1, C_5–C_7 and D_1–D_6 are defined in exactly the same manner as Appendix B.

Finally, $\mathbb{C}^{\mathrm{p}}$ can be obtained:

$$\mathbb{C}^{\mathrm{p}} = \hat{E}_1 \mathbf{1} \otimes \mathbf{s} + \hat{E}_2 \mathbf{1} \otimes \mathbf{1} + \hat{E}_3 \mathbf{s} \otimes \mathbf{1} + \hat{E}_4 \mathbf{s} \otimes \mathbf{s} + \hat{E}_5 \mathbb{I}_{\mathrm{dev}} \tag{F.20}$$

where the only differences from Appendix B are due to the use of $\hat{D}_7$ and $\hat{D}_8$ in place of D_7 and D_8, respectively. That is: with

$$\begin{cases} \hat{E}_1 = C_5 + C_6 \hat{D}_7 \\ \hat{E}_2 = C_7 + C_6 \hat{D}_8 \\ \hat{E}_3 = (B_7 + B_9 C_7) + (B_8 + B_9 C_6) \hat{D}_8 \\ \hat{E}_4 = B_9 C_5 + (B_8 + B_9 C_6) \hat{D}_7 \\ \hat{E}_5 = 2\alpha p_0 A_2 A_5 \end{cases} \tag{F.21}$$

REFERENCES

Auricchio, F., Taylor, R. and Lubliner, J. [1992] "Application of a return map algorithm to plasticity models," in *COMPLAS Computational Plasticity: Fundamentals and Applications*, eds. D. Owen and E. Onate, Barcelona, pp. 2229–2248.

Borja, R. I. and Lee, S. R. [1990] "Cam-Clay plasticity, Part I: Implicit integration of elasto-plastic constituive relations," *Comput. Methods Appl. Mech. Engrg.* **78**, 49–72.

Borja, R. I., Lin, C.-H. and Montáns, F. J. [2001] "Cam-Clay plasticity, Part IV: Implicit integration of anisotropic bounding surface model with nonlinear hyperelasticity and ellipsoidal loading function," *Comput. Methods Appl. Mech. Engrg.* **190**, 3293–3323.

Borja, R. I., Tamagnini, C. and Amorosi, A. [1997] "Coupling plasticity and energy-conserving elasticity models for clays." *J. Geotech. and Geoenvironmental Engrg. ASCE* **123**(10), 948–957.

Callari, C., Auricchio, F. and Sacco, E. [1998] "A finite-strain Cam-Clay model in the framework of multiplicative elasto-plasticity," *International Journal of Plasticity* **14**(12), 1155–1187.

Coulomb, C. A. [1776] "Essai sur une application des rgles des maximis et minimis quelques problemes de statique relatifs l'architecture," *Mem. Acad. Roy. Pres.divers Sav.* **5**, 343.

Dafalias, Y. F. and Herrmann, L. R. [1982] "Bounding surface formulation of soil plasticity," in *Soil Mechanics — Transient and Cyclic Loads*, eds. G. N. Pande and O. C. Ziekiewicz, chapter 10 (Wiley, New York), pp. 253–282.

Drucker, D. C. and Prager, W. [1952] "Soil mechanics and plastic analysis of limit design," *Quart. Appl. Maths.* **10**, 157–165.

Hashiguchi, K. [1995] "On the linear relations of v–$\ln p$ and $\ln v$–$\ln p$ for isotropic consolidation of soils," *Int J. Numer. Analyt. Methods Geomechanics* **19**, 367–376.

Hashiguchi, K. and Ueno, M. [1977] "Elastoplastic constitutive laws of granular materials," in *Proc. 11th Int. Conf. SMFE, Specialty Session 9*, Tokyo, pp. 73–82.

Houlsby, G. T. [1985] "The use of a variable shear modulus in elasto-plastic models for clays," *Comput. Geotech.* **1**, 3–13.

Hughes, T. J. R. [2000] *The Finite Element Method: Linear Static and Dynamic Finite Element Analysis* (Dover).

Lubliner, J. [1990] *Plasticity theory* (Macmillan).

Lubliner, J., Taylor, R. L. and Auricchio, F. [1993] "A new model of generalized plasticity," *Int. J. Solid Struct.* **30**, 3171.

Roscoe, K. H. and Burland, J. B. [1968] "On the generalized stress–strain behaviour of 'wet' clay," *Engineering Plasticity* , 535–609.

Roscoe, K. H. and Schofield, A. N. [1963] "Mechanical behaviour of an idealized 'wet' clay," in *Proc. 2nd Eur. Conf. SMFE*, volume 1, Wiesbaden, pp. 47–54.

Roscoe, K. H., Schofield, A. N. and Wroth, C. P. [1958] "On the yielding of soils," *Geotechnique* **8**, 22–53.

Taylor, R. [2000] "A finite-element analysis program," *Technical report*, University of California at Berkeley, http://www.ce.berkeley.edu/rlt.

von Mises, R. [1913] "Mechabik der festen Koerper im plastisch deformablen Zustant," *Goettinger Nachrichten, math.-phys, Klasse* , 582.

Wroth, C. P. and Houlsby, G. T. [1980] "A critical state model for predicting the behaviour of clays." in *Workshop on Limit Equilibrium, Plasticity and Generalized Stress–Strain in Geotechnical Engineering*, pp. 592–627.

Wroth, C. P. and Houlsby, G. T. [1985] "Soil mechanics—property characterization and analysis procedures," in *Proc. 11th Int. Conf. SMFE*, volume 1, San Francisco, pp. 1–55.

Zienkiewicz, O., Leung, K. and Pastor, M. [1985] "Simple model for transient soil loading in earthquake analysis. I. Basic model and its application," *Int J. Numer. Analyt. Methods Geomechanics* **9**, 453–476.

Zytinsky, M., Randolph, M. K., Nova, R. and Wroth, C. P. [1978] "On modelling the unloading-reloading behaviour of soils," *Int. J. Numer. Analyt. Methods Geomechanics* **2**, 87–93.